NAVAL POSTGRADUATE SCHOOL

MONTEREY, CALIFORNIA

THESIS

SUBSTRATE AND FEEDSTOCK FACTORS AFFECTING COLD SPRAY COATING ADHESION AND RELATED IMPACTS ON CORROSION

by

Jeffrey C. Mitchell

March 2021

Thesis Advisor:	Andy Nieto
Second Reader:	Troy Ansell

THIS PAGE INTENTIONALLY LEFT BLANK

REPORT DOCUMENTATION PAGE			*Form Approved OMB No. 0704-0188*

1. AGENCY USE ONLY *(Leave blank)*	**2. REPORT DATE** March 2021	**3. REPORT TYPE AND DATES COVERED** Master's thesis

4. TITLE AND SUBTITLE SUBSTRATE AND FEEDSTOCK FACTORS AFFECTING COLD SPRAY COATING ADHESION AND RELATED IMPACTS ON CORROSION	**5. FUNDING NUMBERS** B73B6
6. AUTHOR(S) Jeffrey C. Mitchell	
7. PERFORMING ORGANIZATION NAME(S) AND ADDRESS(ES) Naval Postgraduate School Monterey, CA 93943-5000	**8. PERFORMING ORGANIZATION REPORT NUMBER**
9. SPONSORING / MONITORING AGENCY NAME(S) AND ADDRESS(ES) NPS RIP	**10. SPONSORING / MONITORING AGENCY REPORT NUMBER**

11. SUPPLEMENTARY NOTES The views expressed in this thesis are those of the author and do not reflect the official policy or position of the Department of Defense or the U.S. Government.

12a. DISTRIBUTION / AVAILABILITY STATEMENT Approved for public release. Distribution is unlimited.	**12b. DISTRIBUTION CODE** A

13. ABSTRACT (maximum 200 words)

Cold spray technology has the potential to greatly reduce the effects of corrosion on susceptible materials. Lack of adhesion strength is one of the limitations currently preventing cold spray from becoming a dominant resource. Adhesion strength is the strength of the bond between the cold-sprayed coating and the substrate. Without good adhesion, the coating provides minimal protection against corrosion and could potentially make corrosion worse. In order to determine how to increase cold spray adhesion, the feedstock powder and substrate were manipulated to analyze their effects on adhesion. The main areas of focus for this project were the effects of the following characteristics on adhesion strength: i) the surface condition of the substrate, ii) the hardness of the substrate, and iii) the size of the cold spray particles. Samples within each area of focus were sprayed using cold spray and then a pull-off adhesion test was performed. The surface condition of the substrate was further studied to determine its effect on Mg AZ31 alloy's corrosion rate by placing a smooth, roughened, and polished sample within a salt fog chamber for 672 hrs. The results from the adhesion tests showed that softer substrates and smoother surface condition produce higher adhesive strength. The corrosion experiments found that the samples with the higher roughness value saw the highest corrosion rates and formed the thickest oxide layer.

14. SUBJECT TERMS cold spray, adhesion strength, surface treatment, particle distribution, packing, aluminum, magnesium	**15. NUMBER OF PAGES** 103
	16. PRICE CODE

17. SECURITY CLASSIFICATION OF REPORT	**18. SECURITY CLASSIFICATION OF THIS PAGE**	**19. SECURITY CLASSIFICATION OF ABSTRACT**	**20. LIMITATION OF ABSTRACT**
Unclassified	Unclassified	Unclassified	UU

NSN 7540-01-280-5500

Standard Form 298 (Rev. 2-89)
Prescribed by ANSI Std. 239-18

THIS PAGE INTENTIONALLY LEFT BLANK

Approved for public release. Distribution is unlimited.

SUBSTRATE AND FEEDSTOCK FACTORS AFFECTING COLD SPRAY COATING ADHESION AND RELATED IMPACTS ON CORROSION

Jeffrey C. Mitchell
Lieutenant, United States Navy
BS, Virginia Military Institute, 2014

Submitted in partial fulfillment of the
requirements for the degree of

MASTER OF SCIENCE IN MECHANICAL ENGINEERING

from the

NAVAL POSTGRADUATE SCHOOL
March 2021

Approved by: Andy Nieto
Advisor

Troy Ansell
Second Reader

Garth V. Hobson
Chair, Department of Mechanical and Aerospace Engineering

THIS PAGE INTENTIONALLY LEFT BLANK

ABSTRACT

Cold spray technology has the potential to greatly reduce the effects of corrosion on susceptible materials. Lack of adhesion strength is one of the limitations currently preventing cold spray from becoming a dominant resource. Adhesion strength is the strength of the bond between the cold-sprayed coating and the substrate. Without good adhesion, the coating provides minimal protection against corrosion and could potentially make corrosion worse. In order to determine how to increase cold spray adhesion, the feedstock powder and substrate were manipulated to analyze their effects on adhesion. The main areas of focus for this project were the effects of the following characteristics on adhesion strength: i) the surface condition of the substrate, ii) the hardness of the substrate, and iii) the size of the cold spray particles. Samples within each area of focus were sprayed using cold spray and then a pull-off adhesion test was performed. The surface condition of the substrate was further studied to determine its effect on Mg AZ31 alloy's corrosion rate by placing a smooth, roughened, and polished sample within a salt fog chamber for 672 hrs. The results from the adhesion tests showed that softer substrates and smoother surface condition produce higher adhesive strength. The corrosion experiments found that the samples with the higher roughness value saw the highest corrosion rates and formed the thickest oxide layer.

THIS PAGE INTENTIONALLY LEFT BLANK

TABLE OF CONTENTS

LIST OF FIGURES

THIS PAGE INTENTIONALLY LEFT BLANK

LIST OF TABLES

THIS PAGE INTENTIONALLY LEFT BLANK

LIST OF ACRONYMS AND ABBREVIATIONS

EDS	energy dispersive spectroscopy
OP	optical microscope
SEM	scanning electron microscope
STD	standard deviation
USD	United States dollar
XRD	x-ray diffraction

THIS PAGE INTENTIONALLY LEFT BLANK

ACKNOWLEDGMENTS

I would like to thank my thesis advisor, Andy Nieto, for providing all of the knowledge and direction that I needed to successfully complete this thesis. This was a large project and there were many roadblocks along the way, and without your guidance this thesis would not have been at the level it is today. I enjoyed all of our time together and hope the rest of your time here at NPS continues to be successful.

I would also like to thank Dr. Troy Ansell not only for training me on multiple complex pieces of equipment and being my second reader, but also for always being there to answer any of my questions and to provide additional insight.

Likewise, I would like to thank Stefan Kohlgrueber, Dr. Chanman Park, and John Mobley for their assistance in learning proper operation and maintenance of the equipment that played a major role in my research.

THIS PAGE INTENTIONALLY LEFT BLANK

I. INTRODUCTION

A. OBJECTIVES OF THESIS WORK

Cold spray is a developing technology that began receiving commercial attention in the early 2000s [1]. One of the major hurdles left before cold spray can become a dominant method for coating applications is increasing the adhesion strength of the cold spray coating to the substrate surface. Having strong adhesion strength means the metallic particles deposited by the cold spray machine properly stick to the substrate surface and provide the protection or properties the coating was intended for.

The goal of this thesis is to investigate factors affecting adhesion strength of a cold spray coating that have not been previously explored systematically. This thesis will focus on how the surface roughness and hardness of the substrate and the size distribution of the cold spray particles affects the adhesion strength. Two secondary objectives of this thesis are to see if the hardness of the cold spray powder will have a noticeable effect on the adhesion strength and how substrate surface roughness can affect the corrosion rate of highly corrosion-susceptible materials such as magnesium alloys. This is relevant for when poor adhesion strength results in the underlying substrate being exposed.

B. MOTIVATION AND TECHNOLOGY BENEFITS

One potential use for cold spray technology is corrosion prevention. Operating in a marine environment yields a significant probability for corrosion to occur. Corrosion is one of the top costs for the Navy and leads to significant maintenance overhauls that decrease the operational readiness of the fleet. Corrosion can decrease the structural integrity and mechanical properties for vital portions of the ship and will result in extended shipyard times. Shipyard time not only leads to increased costs but also a decrease in the crews' proficiency. The Navy reported in its 2019 budget $24,688,000 in costs that went toward corrosion prevention alone [2]. The Department of Defense (DOD) spent a total of $20.6 billion as a result of corrosion in fiscal year 2016 [3]. Cold spray would provide the ability to apply a metallic coating to susceptible portions of ships or other DOD equipment to increase their resistance to corrosion. Even if the base metal is highly corrosion-

susceptible, the coating can consist of another metal or alloy that is much more resistant to corrosion, thereby greatly reducing overall material costs.

Cold spray also has the ability to restore the structural integrity of damaged materials. Damage to the ship caused by human error, cavitation, corrosion, etc., will commonly lead to extended dry dock periods where major portions of the ship would need to be removed including sections of the hull, screws, and major pieces of machinery. Cold spray would have the ability to restore the structural integrity lost without the need to disassemble the ship. A cold spray coating would be applied using a portable system to the damaged area. This would restore that material's structural integrity, making the ship suitable for sea.

The commercial sector will also benefit from the development of the cold spray process. Once cold spray can be implemented into the production process, metallic coatings can be applied for corrosion prevention and an increase in the material's structural integrity. This will increase the life of the product and save money for the company. Once adhesion strength is better understood, both the military and commercial sector will see major benefits. From there the applications for cold spray can evolve to becoming routine maintenance for preventing corrosion and other major ship repairs.

II. REVIEW OF THE STATE-OF-THE-ART

A. BACKGROUND AND HISTORY

Cold spray is a type of thermal spray. Thermal spray is a common technique for creating a coating on a substrate to serve as a thermal barrier, corrosion protection, wear protection, and multiple others. Another coating method, plasma spray, accomplishes this by heating the metallic particles past their melting point, applying them to the surface of the substrate and then quenching them to create a coating. The problem with this method is the high temperatures. Figure 1 compares these two techniques used in terms of gas temperature and particle speed. The high temperatures can lead to changes in phase, loss of mechanical properties, and increased corrosion rates. The use of cold spray technology has the potential to have the same benefits as plasma spray but with none of the side effects [1].

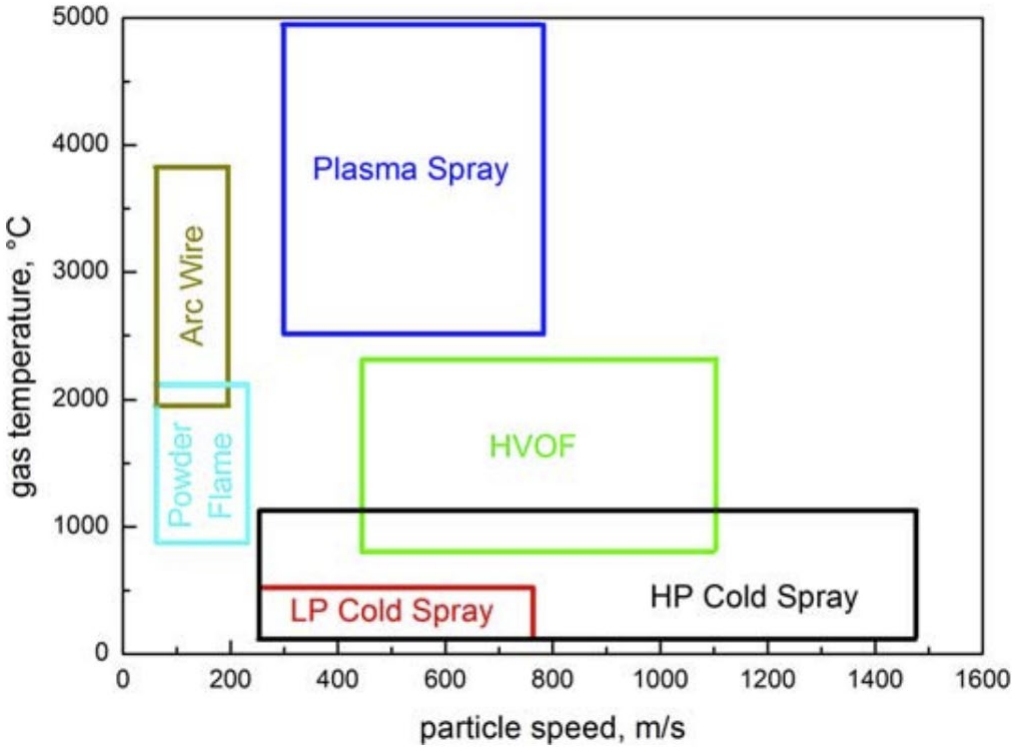

Figure 1. Varieties of additive manufacturing. Source: [4].

The concept of using high-velocity gas to impact metallic particles below their melting temperature onto a substrate has been known since the 1900s [1]. Samuel Thurston submitted the patent, "Method of Impacting One Metal Upon Another" in 1902 [5]. A sketch of Thurston's design can be seen in Figure 2. Unfortunately, the technology was not available at the time to make this process practical. In the 1980s, the Russian Academy of Sciences rediscovered this technique accidently during an experiment in a wind tunnel [6]. The Russians were studying the effects of two-phased gas flow, gas and solid particles mixed together, on different models. They discovered that particles of a certain size, that impacted at a certain angle and velocity, would bond to the surface of the model. The velocity needed to be above a predicted critical value in order for the bonding to occur [1]. In the early 2000s, cold spray machines began to be commercially available [1].

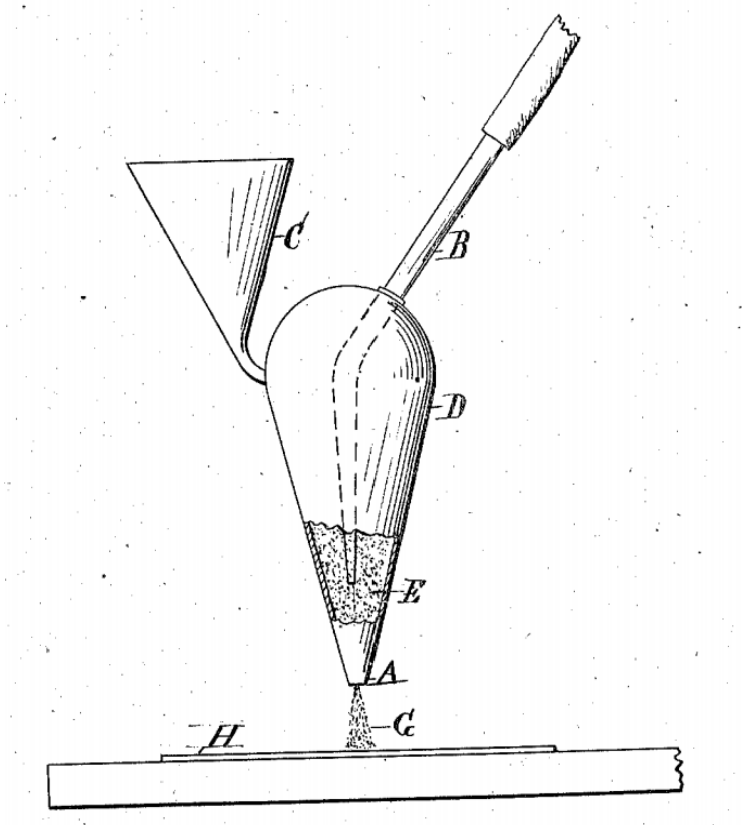

Figure 2. Original plans from the patent of the first cold spray machine. Source: [5].

B. HOW COLD SPRAY WORKS

Two different steps, adhesion of particles to the substrate and the build-up of the particle deposit, are required for cold spray to work. Adhesion is described as the bonding of particles to the substrate [7]. Deposit is the buildup or cohesion of particles to themselves [7]. Poor adhesion will result in less contact area between the coating and substrate. This causes an increase in localized stresses and results in premature failure. Poor cohesion will lead to cracks within the coating and layers of coating flaking off from the bulk coating. Examples of poor adhesion and poor cohesion can be seen in Figure 3.

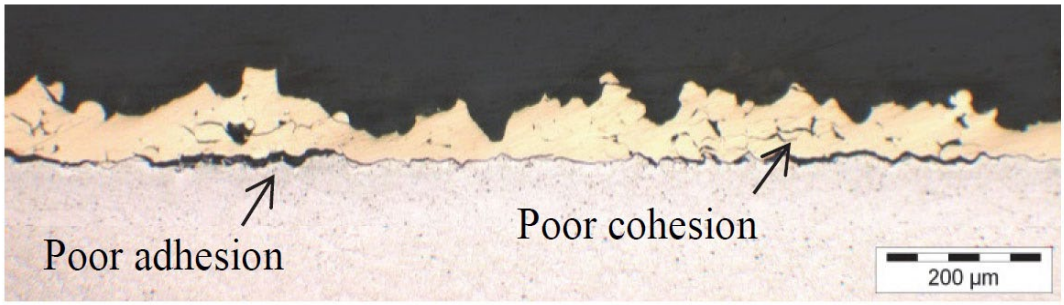

Figure 3. Examples of poor adhesion and poor cohesion. Source: [8].

Cold spray uses differential pressure to propel metallic particles towards the substrate surface. Particles are injected from a source into a De Laval Nozzle. This nozzle converges and diverges to allow the gas to accelerate from subsonic to supersonic speeds. The gas carries the metallic particles through the converging section of the nozzle at subsonic speeds. When the gas reaches the section of the nozzle with the smallest area it reaches Mach 1, which is its choked velocity. The gas velocity then increases to supersonic speeds as the area expands within the diverging section. This drives the metallic particles at high enough speeds that when combined with an increase in temperature to soften the metal, causes the particles to spread on impact and adhere with the substrate surface; a process known as jetting [1], [6], [27]. The particles are heated within the cold spray unit and their temperature never exceeds their melting temperature [7], [11]. Figure 4 shows a schematic of a *modern* cold spray machine.

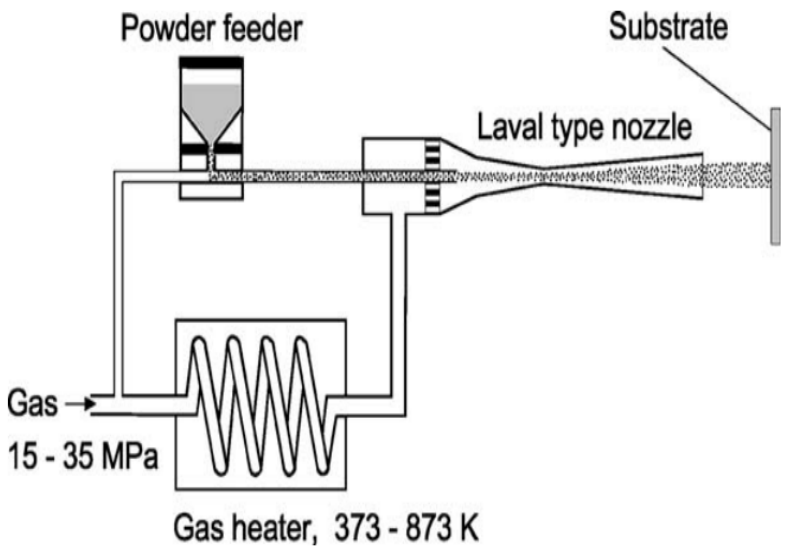

Figure 4. Schematic of cold spray machine. Source: [9].

C. MAGNESIUM: AN IDEAL MATERIAL FOR COLD SPRAY REPAIR

One of the most abundant elements found on earth is Magnesium. It is also significantly less dense than other widely used metals such as aluminum, titanium, and iron [12]. Table 1 shows the density of these metals for comparison. This low density gives magnesium a very high strength to weight ratio, making it highly desirable for engineering applications that desire low weight: automotive, biomedical, aircraft, etc. A 1 kg reduction in weight of an aircraft will result in 1,150 USD fuel savings [13], [14]. This both benefits the environment since it leaves a smaller carbon footprint, and it reduces operational costs. Magnesium is also nontoxic and is 100% recyclable. This further benefits the environment and makes it extremely appropriate for biomedical applications that place metallic components within the human body [15]. Magnesium is also very machinable. Rolling, milling, casting, and turning are significantly easier with magnesium, which in turn reduces manufacturing costs.

Table 1. Comparison of metal densities

Metal	**Magnesium**	**Aluminum**	**Titanium**	**Iron**
Density (g/cm^3)	1.7	2.7	4.5	7.9

One of the main reasons magnesium is not already widely used is its low corrosion resistance [16–18]. Magnesium is a relatively soft metal. This means that scratches and pits are easily formed on its surface. This makes magnesium particularly susceptible to pitting corrosion. Pitting corrosion occurs in two phases, initiation and propagation. Initiation occurs where localized mechanical damage occurs on the substrate's surface or within a pre-existing imperfection. Propagation occurs when positively charged ions build-up within the pit as a result of uniform corrosion. These positive ions then attract additional negatively charged ions causing localized changes in solution pH. This causes accelerated localized corrosion and rapid deterioration of the metal. The pit can propagate in any direction within the metal, will result in only minimal weight changes, and may not be easily identified. This makes the chances of catastrophic failure high. To combat this issue, it is a common approach for magnesium to be coated with a more corrosion-resistant metal [19–22]. To increase the strength of these coatings, the substrate surface will be roughened; unfortunately, this also creates pits [7], [23]. One goal of this thesis is to see how the rate of corrosion will change when a sample of magnesium is intentionally roughened to increase the adhesion of a metallic coating.

D. CURRENT UNDERSTANDING OF FACTORS THAT AFFECT COLD SPRAY ADHESION

There are three primary factors that are known to affect the adhesion of a coating to a substrate: particle temperature, particle velocity, and the surface characteristics of the substrate. Particle temperature can either be controlled through direct heat input or indirect heat input [7], [24]. Direct heat input involves pre-heating the powder prior to cold spray. Indirect heat input involves heating the gas, which then heats the particles [7], [24]. The easiest, and most ideal method of influencing particle temperature is indirect heat input [7], [24]. The gas travels through heaters within the cold spray machine prior to being injected with the metallic powder. The higher temperature gas then transfers heat to the metallic particles through convection. Figure 5 shows a simulation of how the temperature of the gas elevates the temperature of the particles. T_p15/V_p15 represents the temperature and speed of a 15 μm Cu particle as it travels through the de Laval nozzle [24]. T_g/V_g represent the change in temperature and velocity of nitrogen gas through the de Laval nozzle [24].

The temperature of the gas and metallic particles decrease as they travel through the nozzle to the substrate surface. The temperature of the gas decreases faster than the particles due to the higher heat capacity of the metal. Temperatures used for cold spray range from 20 C–1000 C [4].

Direct heating will result in a longer period of time that the particles remain at elevated temperatures. This decreases the particle's hardness from an annealing affect, resulting in a lower critical velocity and higher probability of adhesion [7]. However, if the particles are not preheated under vacuum, the higher temperatures will result with an increased oxidation rate [7]. The presence of an oxide layer will inhibit proper adhesion. Thus, for adhesion to occur the oxidation layer would have to be broken, which results in a higher required critical velocity [7].

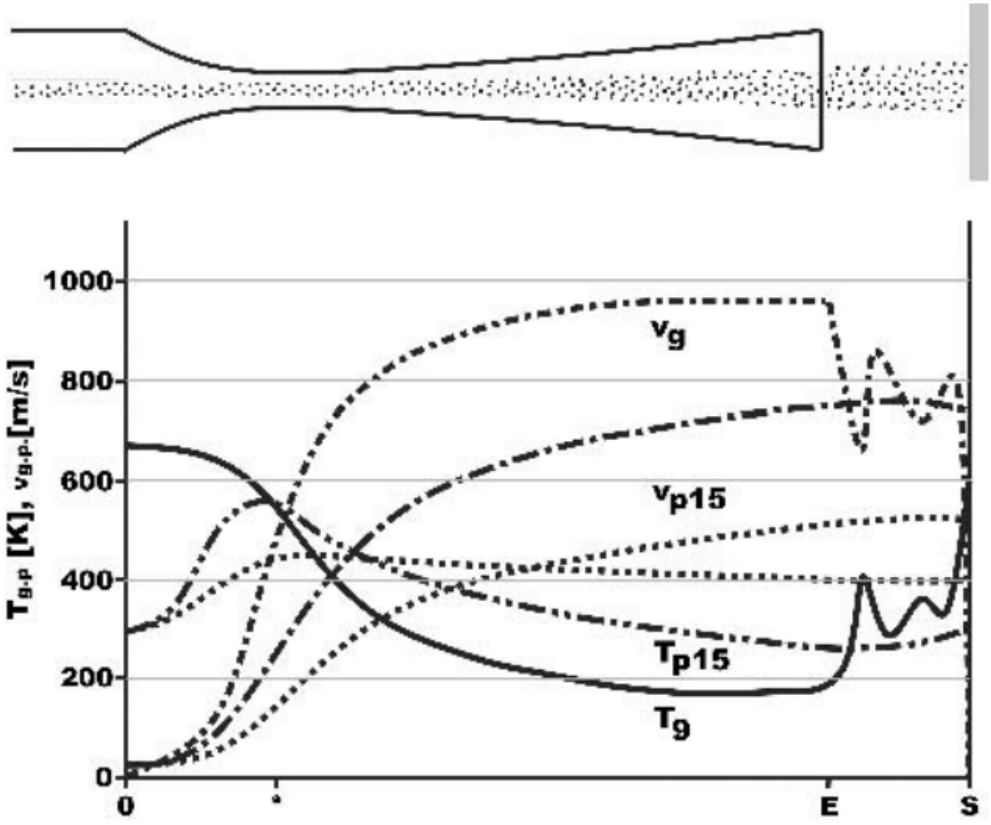

Figure 5. Change in particulate temperature and velocity through cold spray nozzle. Source: [24].

The higher temperatures are required to increase the ductility of the particles. This increase in ductility affects two different parameters of the particles: the flattening ratio and the critical velocity. The flattening ratio is a numerical representation of the amount of particle deformation that occurs upon impact with the substrate surface [25]. Particles with a higher flattening ratio will become more deformed once contacted with the substrate surface. Higher flattening ratios correspond to a higher surface area for bonding, decreased porosity, and increased adhesive/cohesive strength [25]. The equation for flattening ratio is [25]

$$Flattening\ Ratio = 1 - \frac{h_p}{d_p}, \tag{1.1}$$

where h_p is the height of the flattened particle and d_p the initial particle diameter, shown in Figure 6. This ratio was simplified by Assadi et al. to the ratio of particle impact velocity and particle critical velocity ($\frac{v_{pi}}{v_{cr}}$) [25]. The critical velocity of a particle is the minimum velocity required for particle deformation and for adhesion to occur between the particle and the substrate surface [7]. A particles velocity must be higher than its critical velocity for adhesion to occur.

The simplest way to determine the required critical velocity of a particle is using Equation 1.2 [9], [26].

$$V_{cr} = 667 - 14_{\rho} + 0.08\mathrm{T}_m + 0.1\sigma_u - 0.4T_i \tag{1.2}$$

In this equation, ρ is the density of the powder, T_m is the powders melting temperature in kelvin, σ_u is its ultimate strength, and T_i is the initial temperature of the particle in kelvin [9], [26]. This equation shows the critical velocity required for adhesion changes based on the mechanical properties of the powder that is used and the temperature the particle is heated to inside the cold spray unit [6]. The flattening of the particle aids two different bonding mechanisms: metallurgical bonding and mechanical interlocking. Mechanical interlocking is the physical weaving of particle and substrate that holds the coating onto

the substrate surface. This bonding mechanism is not as strong as metallurgical bonding but can be easier to create [27]. Metallurgical bonding is the atomic diffusion of the substrate surface and the coating. The increased heat that occurs once the particle impacts the substrate surface can cause an intermetallic phase to form or localized alloying in compatible metals, causing an increase in bond strength. For this to occur the particle needs to flatten onto the substrate surface and the bonding area needs to be oxide free [27].

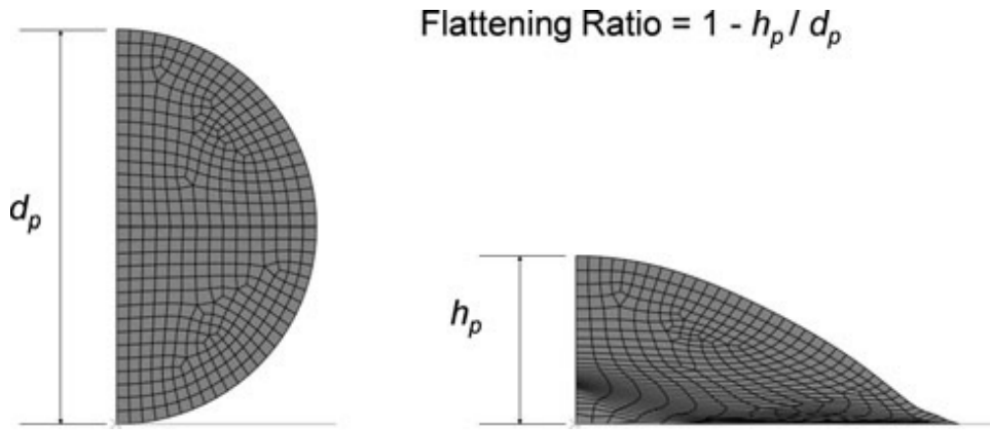

Figure 6. Flattening of metallic particle. Source: [25].

The flattening of the particle is the result of an adiabatic shear instability. When the particle hits the surface, it causes a localized peak in temperature. This increase in temperature causes strain softening in the shear direction and a decrease in strength, which allows the particle to act fluid like; also known as jetting [6], [10], [26]. The factors affecting the prominence of jetting can be best represented by Equation 1.3 [10].

$$\sigma = [\mathrm{A} + \mathrm{B}_{\varepsilon_\rho}^{\eta}][1 + Cl\eta\frac{\varepsilon_\rho}{\varepsilon_o}][1 - (\frac{T - T_{ref}}{T_{melt} - T_{ref}})] \tag{1.3}$$

The equation shows the calculation of flow stress. Flow stress is the stress required to cause a material to plastically deform at a constant strain [10]. The lower the flow stress, the more likely the metallic particle will act fluid-like, causing jetting to occur. The first bracket shows the effects of strain hardening on flow stress with A, B, and η being material

constants of the particle [10]. The second bracket shows the effects of strain rate hardening with C being a material constant, and $\frac{\varepsilon_\rho}{\varepsilon_o}$ being the ratio of the particles strain rate to a reference strain rate [10]. The third bracket shows the effects of temperature the T being the particle temperature, T_{melt} being the melting temperature of the particle and T_{ref} as a reference temperature [10].

The equation for flow stress demonstrates that jetting is more likely to occur with less material hardening and an increase in particle softness resulting from a higher temperature. Figure 7 shows time-lapsed images of a model for jetting. The jetting causes a difference in velocity between the heated substrate material and the flowing particle material. This difference in velocity causes an instability to occur, mixing the two materials together. The weaving of metals adheres the coating to the substrate through mechanical interlock and depending on the metals being used, promotes a metallurgical bond to form between the two metals.

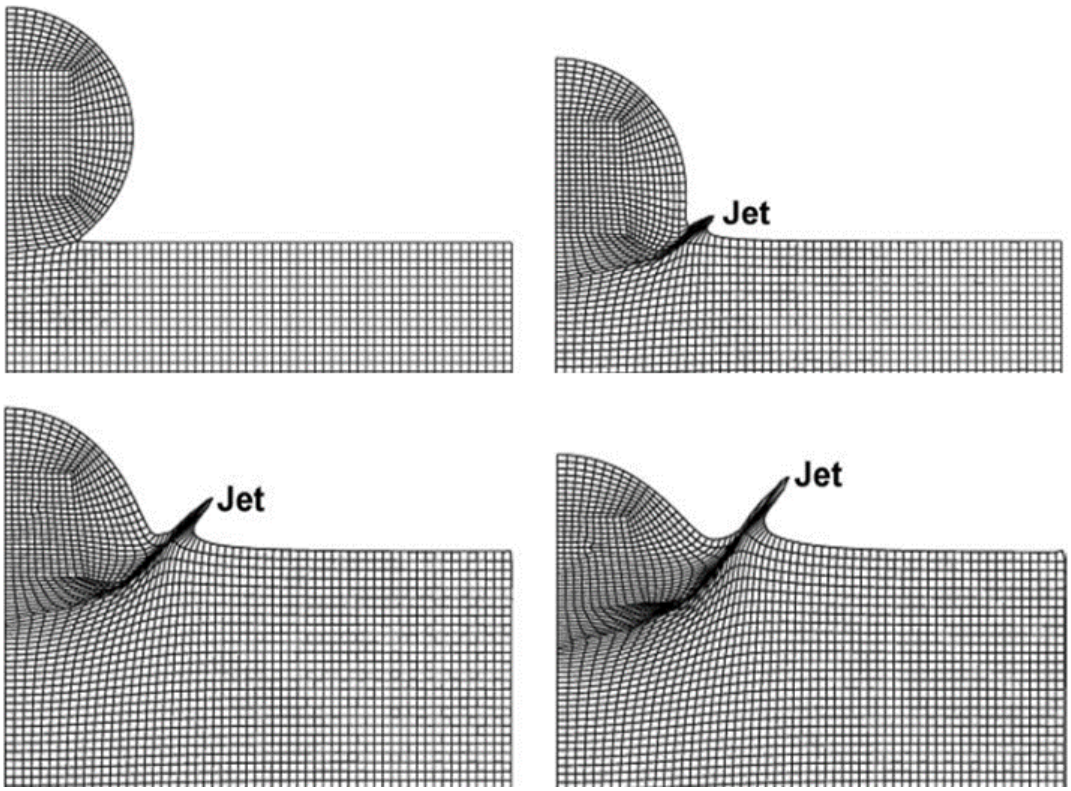

Figure 7. Jetting principle. Source: [6].

Particle velocity is controlled by multiple variables including gas velocity, particle size and shape, and the stand-off distance. The impact velocity of a particle can range from 200–1200 m/s based on these factors [26]. The gas is the driving fluid that carries the metallic powders through the nozzle and onto the substrate surface. The speed of the gas can be controlled three different ways: gas pressure, gas temperature, and gas type. As the gas pressure increases, so will the velocity of the gas as it exits the nozzle. The higher the gas velocity, the higher the corresponding particle velocity will be. Table 2 and Figure 8 show the nonlinear relationship between gas pressure and particle velocity at a constant temperature.

Table 2. Effects of gas pressure on particle velocity. Source: [28].

	Propellant gas pressure (MPa)	**Propellant Gas Temperature (°C)**	**Particle average velocity (m/s)**	**Particle velocity standard deviation (m/s)**
A	0.2	150	271	35
B	0.5	150	359	41
C	1.0	150	430	46

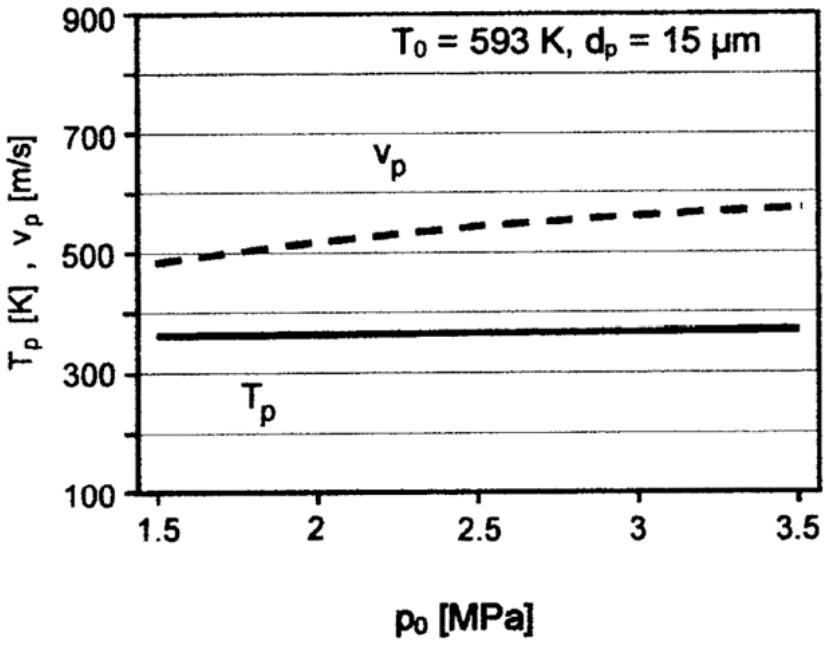

Figure 8. Effect of gas pressure on particle velocity and temperature. Source: [24].

The temperature of the gas also affects the speed. As the temperature of the gas increases, the energy of the gas molecules also increases. This increase in molecular energy results in an increase in molecular velocity, causing the gas velocity to increase. This affect can be seen in Figure 9. The results in Figure 9 were determined using copper particles with a uniform particle diameter of 15 μm, nitrogen gas, and a constant gas inlet pressure, p_0 [24]. As the gas inlet temperature, T_0, increases, the particle temperature and velocity, T_p and V_p, both increase [24]. The increase in gas temperature will also increase the gas pressure. Assuming the cold spray machine is a fixed volume within the nozzle, as temperature of the gas increases, so will its inlet pressure. This relationship between gas temperature and pressure at the entrance of the nozzle is represented in the ideal gas law, equation 1.4.

$$PV = nRT \tag{1.4}$$

For this equation P is the gas pressure, V is the volume, n is the amount of the gas, R is the ideal gas constant, and T is the temperature. This relationship can be applied to compressed air, nitrogen, and helium by using the appropriate gas constant, R [29]. However, this relationship is only applicable at the entrance of the nozzle while the gas is still subsonic.

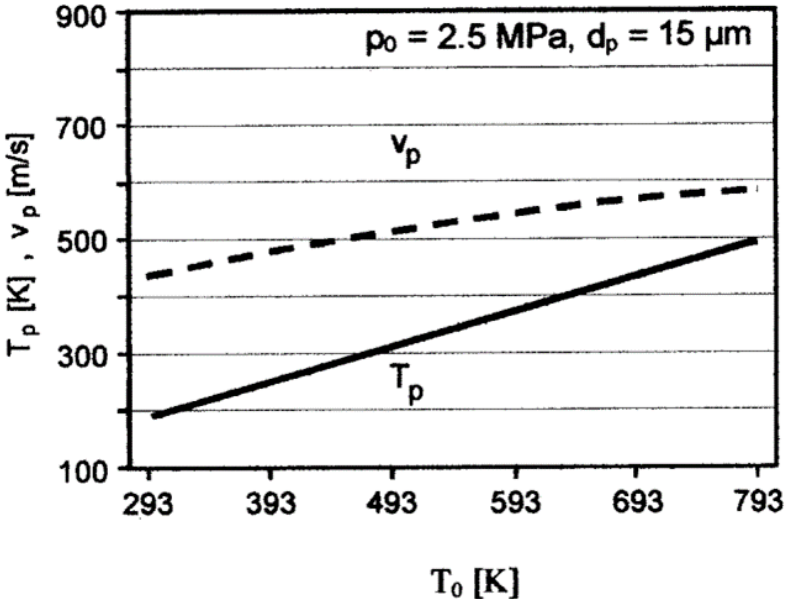

Figure 9. Effect of gas temperature on particle velocity and temperature. Source: [24].

There are three commonly used gases for cold spray: air, nitrogen, and helium. The most efficient gas is helium. Table 3 compares the specific heat ratios and the specific gas constants of all three gases. The specific heat ratios, the ratio between the specific heat at constant pressure and constant volume, of these three gases does not vary significantly and does not cause significant variations of gas velocity [7].

The specific gas constant is the gas constant, $8.3145 J*mol^{-1}*K^{-1}$, divided by the molecular mass of the element. This gas characteristic is significant because it shows how much energy a gas will have at a given temperature. Table 3 shows that at a given temperature and number of particles, the energy of the air and nitrogen are approximately the same. However, under the same conditions helium's specific gas constant is approximately ten times higher than both air and nitrogen [7]. This means that helium particles will have significantly more energy than air or nitrogen at a given temperature. This, as previously discussed, means that helium gas will have a higher velocity under the same working conditions, making it more efficient.

Table 3. Specific heat ratio and specific gas constant for air, nitrogen, and helium. Source: [7].

	Air	**Nitrogen**	**Helium**
Υ	1.4	1.4	1.66
R_s ($J*kg^{-1}*K^{-1}$)	287	297	2077

The specific heat capacity of these three gases is also an important factor to consider. Specific heat capacity is the amount of energy that is required to raise or lower a certain amount of an element by one degree of temperature. This number can be based on two different assumptions; either the element is under constant pressure or it is maintained at a constant volume. The specific heat capacity is a great representation of an element's ability to retain heat. A high specific heat capacity indicates that more energy needs to be added or removed to change the temperature of the element. This means that an element

with a high specific heat would be able to retain a higher temperature for a longer period of time.

Table 4 shows the specific heat capacity for all three gases under constant pressure and constant volume. Under both constant pressure and constant volume, nitrogen and air both have very similar values. Helium is magnitudes higher under both assumptions. This is significant because it means that helium will retain the set temperature for a longer period of time during the cold spray process. This means helium gas will decrease velocity at a slower rate and will also be more efficient at transferring heat to the metallic particles. Helium is the most expensive option followed by nitrogen. Compressed air is the cheapest option and can be provided through the use of a local compressor. Common pressures used in cold spray range from 0.2 MPa to 4.0 MPa [7].

Table 4. Specific heat capacity for air, nitrogen, and helium under constant pressure and constant volume assumptions Adapted from [30].

	Air	**Nitrogen**	**Helium**
C_p ($kJ*kg^{-1}*K^{-1}$)	1.005	1.039	5.193
C_v ($kJ*kg^{-1}*K^{-1}$)	0.718	0.743	3.116

The size and shape of the metallic particles also contributes to the speed the particle travels. Figure 10 shows examples of various sizes and shapes of particles. Larger particles will travel slower than smaller particles. The shape of the particle will also affect the aerodynamics of the particle. Spherical particles will travel slower than particles with irregular surface morphology at the same gas pressure. Irregular morphologies will have a higher drag coefficient, and this increased resistance to flow will allow the gas to better carry the particles to the substrate surface. However, irregular shaped particle's drag coefficients are not consistent or predictable, so this trend is not reliable. Spherical powders will be much more precise [31].

The third major factor that affects the particle velocity is the stand-off distance. The stand-off distance of the cold spray machine is the distance from the tip of the nozzle to the substrate surface. The longer this distance, the slower the particles' velocity will be when it hits the substrate as a result of increased atmospheric resistance.

The characteristics of the substrate surface can have a major role in coating adhesion. The surface of the substrate can be polished, as milled or machined, or rough. A rougher surface will potentially promote better mechanical interlocking between the particles and the substrate surface. Smoother surfaces will promote particle rebounding, but have less vulnerability to the formation of an oxide layer. The research that relates the substrates surface condition and how it affects coating adhesion strength is inconclusive. Some research has shown that surface roughness increased adhesion strength depending on the grit blasting technique [32]. Other research has shown that a roughened surface performed worse that polished and untouched surfaces [27]. The hardness of the substrate material can also have an effect on the coating's adhesion. The harder the material the more likely the particles will rebound off the substrate. This could lead to increased porosity and a decrease in adhesion strength.

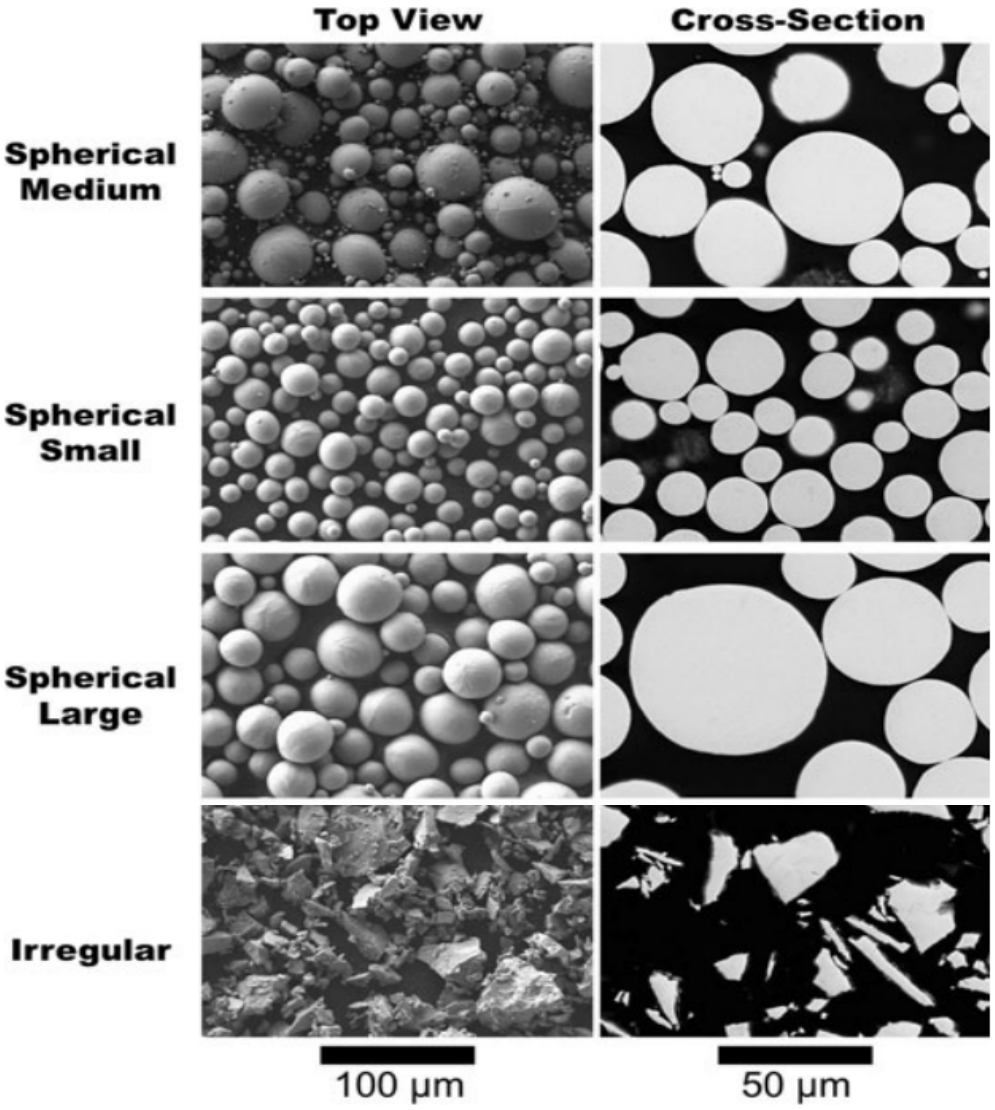

Figure 10. Different particle morphologies. Source: [31].

THIS PAGE INTENTIONALLY LEFT BLANK

III. EXPERIMENTAL PLAN

A. ADHESION STRENGTH DETERMINATION

1. Materials and Parameters

The primary substrate for this thesis was AZ31 magnesium alloy. All substrates were cut into rectangular bars approximately 160 x 25 x 6 mm and were cold sprayed using a CenterLine Supersonic Spray Technologies division (SST) Series P Spray Machine, with a X-Feeder, and a Series P Automatic Spray Gun (LaSalle, ON, Canada). All powders used were purchased from CenterLine SST. Table 5 shows the full list of all substrates and powders used. Each sample's coating was sprayed in one pass of the automatic spray gun. The gun was set up with a standoff distance of 12.7 mm, a line spacing of 2 mm, and a speed of 20 mm/sec. The parameters used for the cold spray process varied for each powder type. Table 6 lists the specific parameters used for each powder. All parameters listed in Table 6 correspond with using nitrogen gas with the exception of stainless steel. Stainless steel powder was sprayed using helium gas.

Table 5. List of materials used

	Substrate Composition	Powder Composition	Powder Vendor Identification
Magnesium (Mg)	AZ31(96% Mg, ~3% Al, and ~1% Zn)	Not Applicable	Not Applicable
Aluminum (Al)	AA5083 (95% Al, 4% Mg, and 1% Mn)	Pure Al	SST-A0017
Stainless Steel (SS)	316L (70% Fe, 16% Cr, 10%Ni, 2% Mo, and 2% Mn)	316L (84% Fe, 16% Cr, and 10%N)	SST-S5002
Copper (Cu)	110 (100% Cu)	Pure Cu	SST-C5003

Table 6. Cold spray parameters

Powders	Gas	Feed (%)	Feed (g/min)	Feed (cc/min)	Temperature (°C)	Pressure (MPa)
Cu	Nitrogen	5	21.4	11.3	350	1.37
Al	Nitrogen	25	21.4	20.7	250	1.59
SS	Helium	14	210.7	45.8	400	0.83

2. Surface Roughening

To measure the effect of surface roughness on adhesion strength there were two different surface conditions that were sprayed. The first is the smoother, as-received surface condition and the second is roughened surface condition created with the use of a grit blaster using a Al_2O_3 media on all sides. The roughness of each sample was measured using an optical profilometer (Zygo NewView 7100, Berwyn, PA, USA). Each sample was labeled based on the powder material, the powder size distribution, and the substrate material used. The use of the stock powder would be designated by "S", the fine particle distribution would be designated by "F", and the mixed particle distribution would be designated by "M". A grit blasted sample is designated by "G" following the substrate material. An example is Al-S-MgG. This sample using aluminum powder, with stock powder size distribution, and was sprayed onto a grit blasted magnesium substrate. Figure 11 shows the structure of this experiment. Each blue square indicates a different sample.

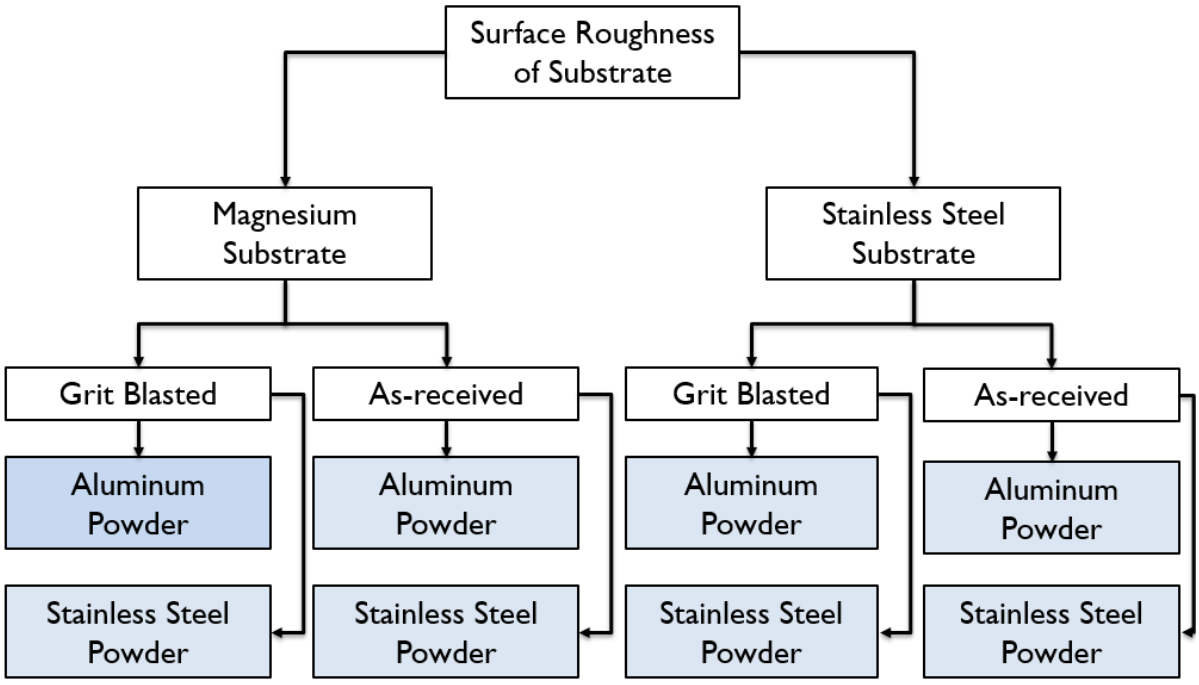

Figure 11. Experimental plan: Surface roughness of substrate

3. Substrate Hardness Characterization

To measure the effect of substrate hardness on adhesion strength, four different substrate materials with varying hardness were used. Magnesium, aluminum, copper, and stainless steel substrates were used and were sprayed with aluminum and stainless steel powders. Table 7 lists each substrate with its corresponding Vickers hardness value. For each substrate, a minimum of 10 hardness measurements were taken on a Struers Durascan (Struers Inc., Cleveland, OH, USA). Each measurement had a minimum of 500 µm spacing from other measurements. This spacing was based on being a multiple of 5 of the measurement diagonal, which ranged from 50–70 µm. The two different powders determined if the hardness of the cold spray powders will have a noticeable effect on the adhesion of the cold spray coating. The Vickers hardness value will be determined for each coating using the same process preformed on the different substrates. The only change will be the minimum spacing between measurements to accommodate limited coating size.

Figure 12 shows the structure of this experiment with each blue square indicating a separate sample.

Table 7. Substrate hardness

Substrate	Vickers (mean)	STD
Mg	56.210	4.237
Al	88.840	2.150
Cu	90.070	3.449
SS	159.100	8.306

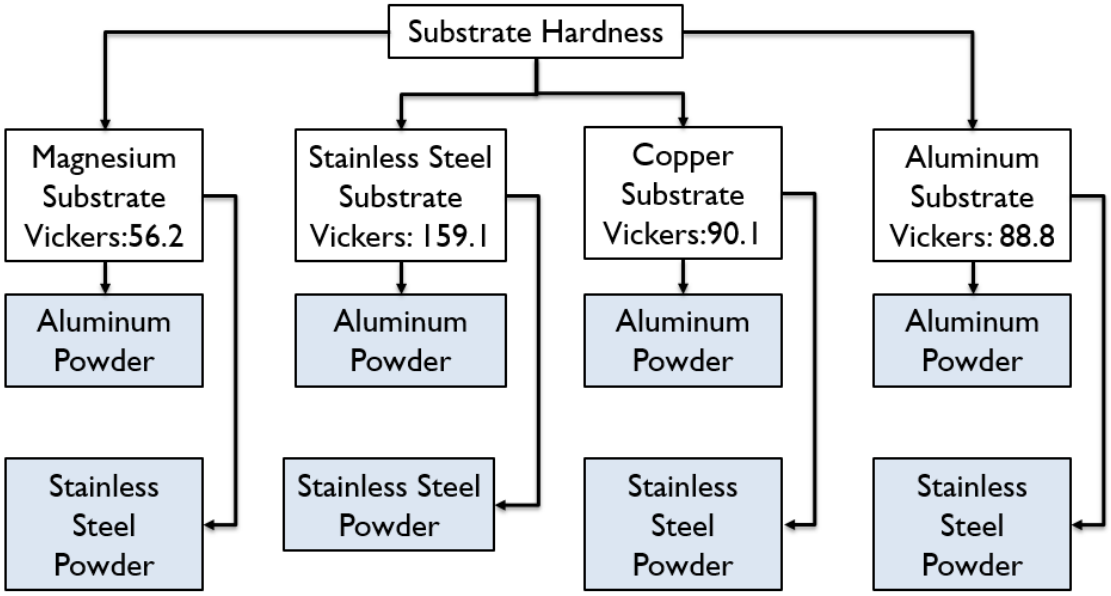

Figure 12. Experimental plan: Substrate hardness

4. Particle Size Distribution

To determine if the distribution of cold spray powder size effects the adhesion strength, aluminum, copper, and stainless steel particles were sieved using a vibratory sieve shaker (Retsch AS 200, Newtown, PA, USA) at an amplitude of 1.25A for 1 hour to separate the stock powders by size. Magnesium bars were sprayed with stock powder, a

mixture of the finest and coarsest particle size distributions, and with the finest particle size distribution only. The stock powder sample were treated as the control. This experiment determined if different particle sizes will result in a less porous, more uniform surface area for the coating, increasing its adhesion.

The expected distribution for each powder type is shown in Figures 13–15. The yellow particle represents the largest size distribution. The red article represents the finest size distribution. The green particle represents the particle sizes in between the yellow and red particles. Figure 13 represents the expected particle distribution of the stock powder. The mixture of small, medium, and large is predicted to have a larger amount of porosity. The increased porosity would be the result of the different particle sizes not being able to fill all voids during the jetting process. The increase in porosity would result in a decrease in adhesion strength.

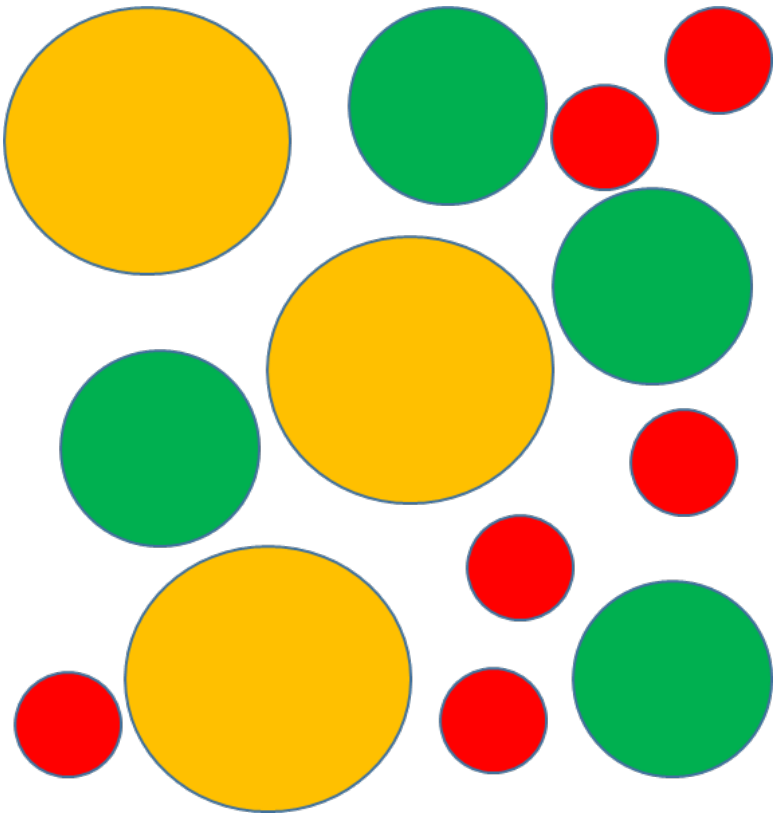

Figure 13. Particle distribution within the stock powder

Figure 14 represents the expected morphology of the fine powder distribution. This distribution is expected to have a reduced porosity when compared to the stock powder. Having only fine particles would reduce the size of the voids between particles during the spray process and would increase the efficiency the voids are able to be filled by the jetting particles. The decrease in porosity would result in a higher adhesion strength. However, the adhesion strength is not expected to be as high as the mixed powder morphology.

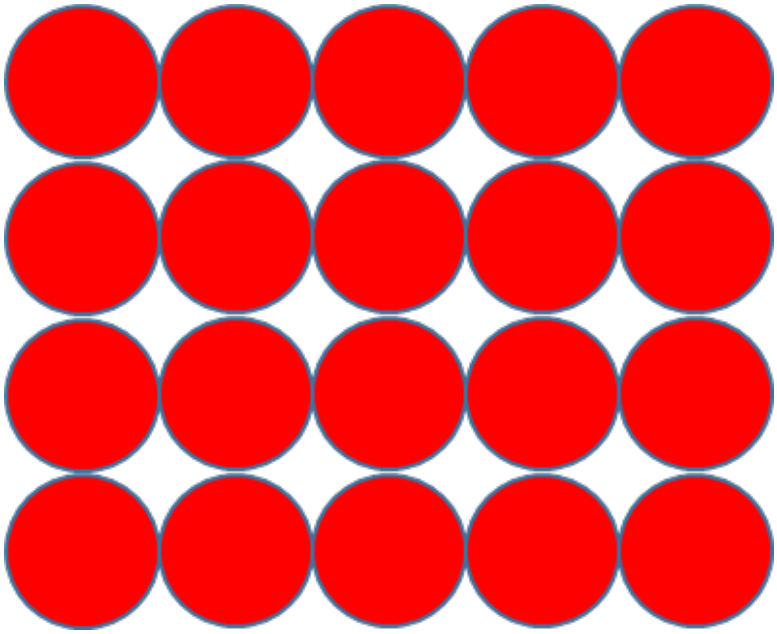

Figure 14. Particle distribution within the fine powder

Figure 15 represents the expected morphology of the mixed powder distribution. Using a mixture of the coarse and fine particles, the expected porosity should be the lowest of the three-particle distribution. The fine particles will fill in the voids left between the large particles. An example of this can be seen in Figure 16. Figure 16 shows two layers of mixed distribution of particles after being sprayed on the surface of a substrate. Figure 16A shows the coating with only large particles. Figure 16B shows the coating with mixed powder distribution. The smaller particles have filled in the voids between the larger particles and after the jetting process, the porosity is essentially reduced to zero. The larger particles have increased the uniformity of the coating surface area. These two factors are

expected to result with the mixed particle morphology having the highest adhesion strength.

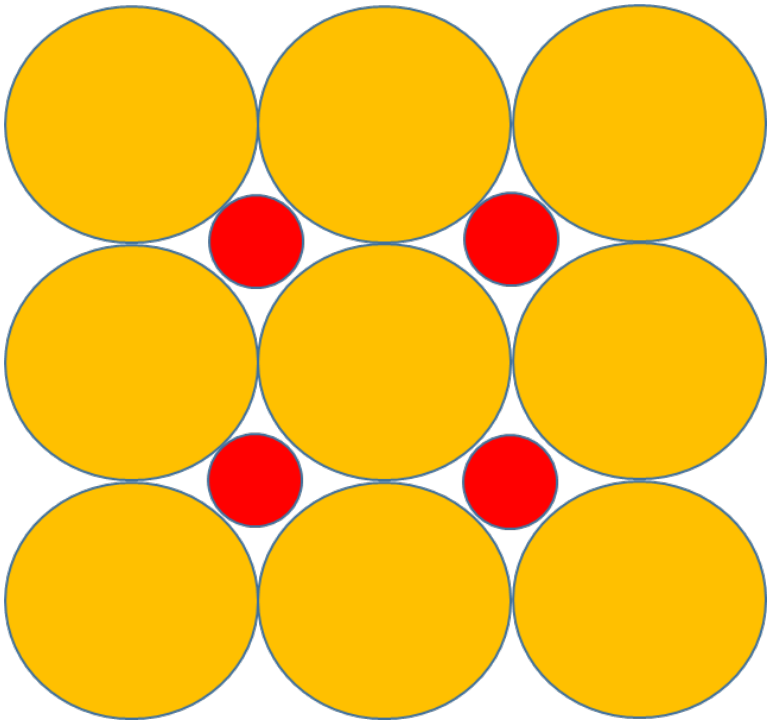

Figure 15. Particle distribution within the mixed powder

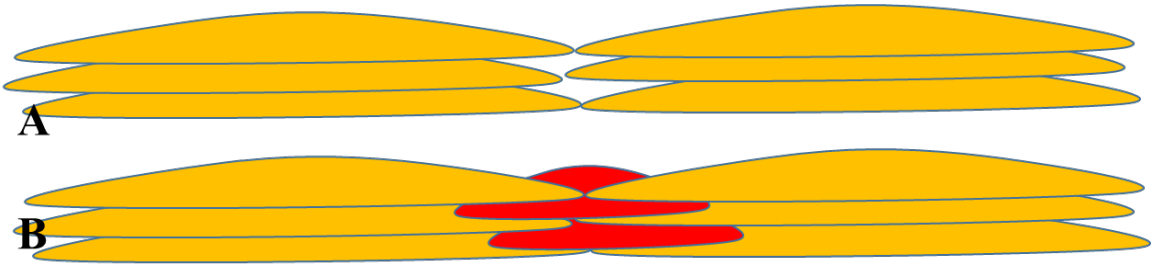

Figure 16. Coating morphology

Figure 17 shows the structure of this experiment with each blue box indication a separate sample. Within the blue boxes, the values in parenthesis indicated the specific particle size range.

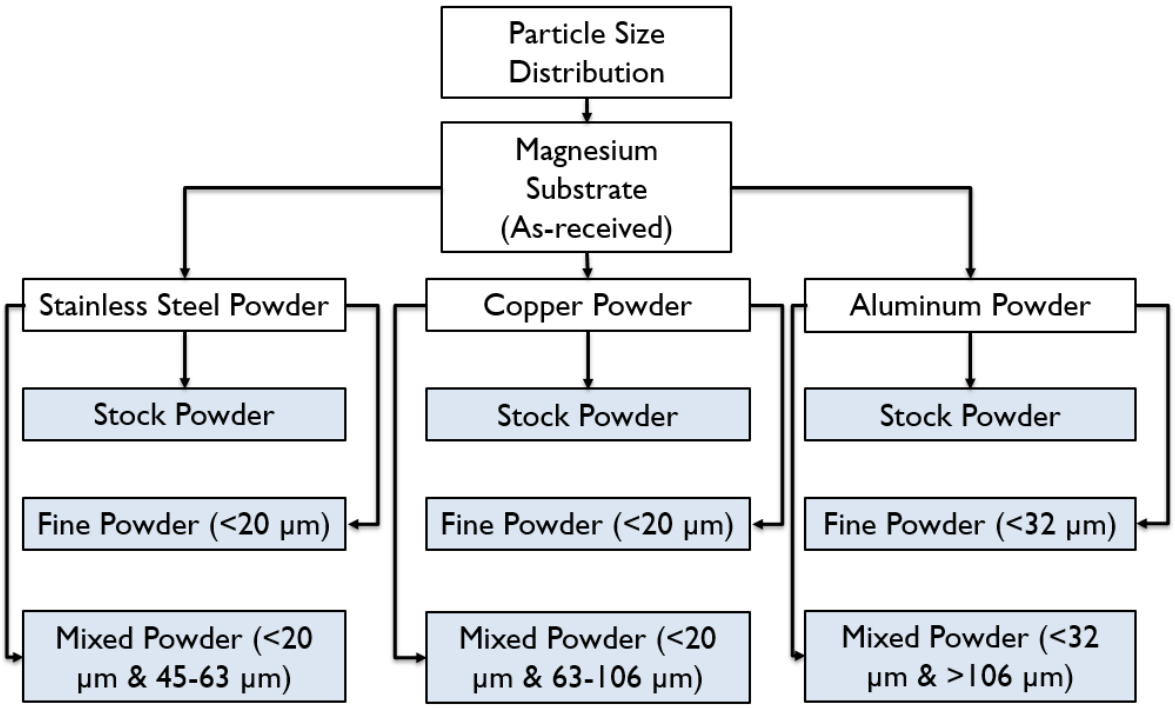

Figure 17. Experimental plan: Particle size distribution

5. Material Characterization

Each sample was evaluated for its adhesion strength using a Elcometer 510 Model T pull-off testing unit (Elcometer Inc., Warren, MI, USA), which is able to be used in accordance with ASTM D4541. With this unit, 20 mm diameter dollies were used with J-B Weld Cold-Weld Steel Reinforced Epoxy (rated maximum bond strength of 34.61 MPa.) A successful test was considered to be greater-than or equal to 30% non-glue failure. A minimum of 4 successful tests were required for each experimental condition. After the adhesion results are determined, one sample from each experimental condition was cross-sectioned using an abrasive saw. Each cross section contained both untouched coating as well as a portion from the adhesion pull off test. This allowed for both analysis of the coating bond to the substrate and the failure mechanism that resulted from the adhesion test. The cross sections were placed in a cold epoxy resin and then polished in accordance with Table 8. A Buehler Ecomet 4 Variable Speed Grinder-Polisher with a Automet 2 Power Head (Buehler, Lake Bluff, IL, USA) was used for both automatic polishing as well

as manual polishing. Each cross section was then examined under a Nikon Epiphot 200 optical microscope (OM) (Nikon Instruments Inc., Melville, NY, USA) and scanning electron microscopy (SEM) using a Zeiss Neon 40 Field Emission SEM (Carl Zeiss Microscopy, LLC, White Plains, NY, USA).

Table 8. Polishing procedure

Grit	Auto/Manual	Pressure (lbs)	Machine Speed (rpm)	Time (min)	Note
320	Auto	3	300	5	Polish until puck is level with full sample exposed
600	Auto	1	200	15	
800	Auto	2	200	45	
1200	Auto	2	200	30	
0.06 µm Silica Solution	Manual	Light hand pressure	≥ 350	N/A	Goal is to minimize scratches

B. MAGNESIUM CORROSION

This section was previously published in the journal *Metals* [33].

1. Materials

A rectangular bar of as-received AZ31 Mg alloy (96% Mg, ~3% Al, and ~1% Zn) was cut utilizing a high-speed abrasive saw to split it into three, equal-sized rectangular bars (48 mm × 22 mm × 9 mm). One bar was utilized in the as-received surface condition and served as a control or baseline sample. The second sample was mechanically polished to a near-mirror finish utilizing 320, 600, 800, and 1200 grit SiC paper, in order to substantially remove any pre-existing scratches or other defects on the surface. The polishing machine utilized was a Buehler Ecomet 3 variable speed grinder-polisher. The sample was polished on all six sides equally. Due to the softness of the material, the polishing machine was only used with the 320 and 600 grit paper. For the 800 and 1200 grit polishing steps, the samples were polished manually. The third sample was grit-blasted

using Al_2O_3 media, on all sides to produce a roughened surface with pre-existing surface defects such as craters, scratches, and micro-crevices that would serve as initial pitting sites. The ensuing surface roughness of each sample was quantified using an optical profilometer.

2. Salt Fog Chamber Exposure

The control, roughened, and polished samples then underwent a 672-h salt fog chamber test in accordance with ASTM B117-11 using a 3.5 wt.% NaCl solution at approximately 30 °C [34]. The three samples were placed in a custom 3D-printed tray where they stood at a 20° incline relative to the vertical. Drainage holes were drilled throughout the bottom of the tray to ensure water did not gather in the bottom of the tray and expose the lower half of the bars to a more severe corrosion environment. Due to the bottom portion of the tray not being fully open to the humid air environment, these portions of the bars were not used for the dimension measurements or surface characterization.

The sample was placed so as to permit an unencumbered exposure of the fog, and the samples were not in contact with any other material that has wicking characteristics. The magnesium samples were removed from the salt fog chamber after 96 h and 168 h in order to track the changes in the dimensions and mass. This same timing was utilized for the duration of the 672 h experiment on a week-by-week basis. Prior to the measurements, loose and hydrated corrosion layers were carefully removed utilizing a razor blade, being careful not to scratch the surface, and preserved in a plastic bag to dry for further characterization. Harsh solutions such as acids were not used to avoid restarting the initial corrosion processes, in order to more accurately observe the trends over time. The weight loss measurements are acknowledged to be conservative, as a greater weight loss could have been recorded if the thin MgO oxide layer had been chemically removed.

3. Material Characterization

At the completion of the salt fog chamber test, the polished, roughened, and control sample top surfaces and cross-sections were examined using the SEM and the equipped EDAX Octane Elect energy dispersive spectroscopy (EDS) detector. EDS elemental mapping and point analysis were conducted. The point analysis consisted of 5 points on

each region of interest. The SEM was operated using a 2 kV accelerated voltage and a 5 mm working distance. Cross-sections were made by mounting samples in an epoxy resin and cut using an abrasive saw. The mounted samples were polished utilizing 320, 600, 800, and 1200 grit paper. To alleviate charging, a 2 nm layer of platinum–palladium was sputtered onto the samples prior to the SEM analysis.

THIS PAGE INTENTIONALLY LEFT BLANK

IV. RESULTS

A. FACTORS AFFECTING ADHESION

1. Surface Roughening

An optical profilometer was used to measure the roughness of magnesium and stainless steel substrate surfaces for both the smooth and grit blasted conditions. The roughness of each sample is quantified by the average roughness value (Ra), which is the measure of the depth of the craters and trenches on the substrate surface. Figure 18 shows images for both the smooth and roughened samples of magnesium. The key thing shown in Figure 18 is that the roughened sample is over five times rougher than the untouched sample. Figure 19 shows the profilometer images for the smooth and roughened stainless steel samples. The grit blasting process causes a minimal effect on the stainless steel samples. This is most likely due to the higher hardness value of stainless steel.

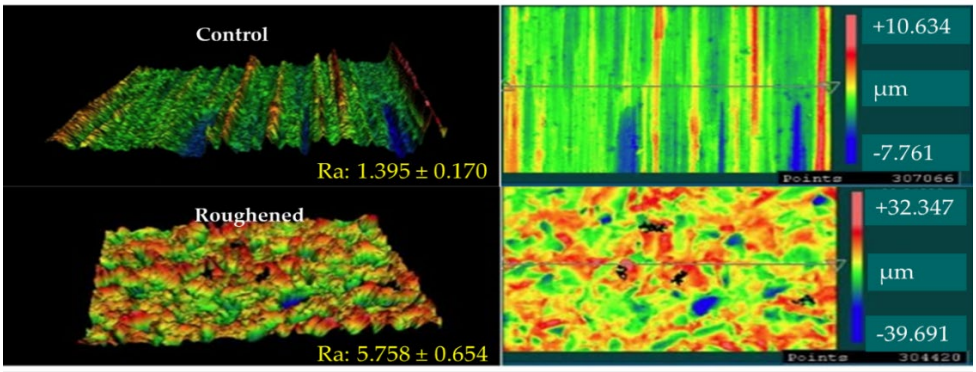

Figure 18. Optical profilometer images of magnesium substrate

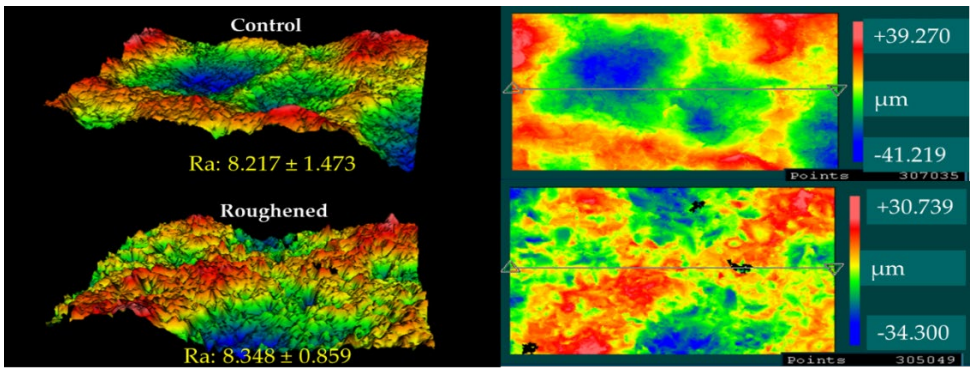

Figure 19. Optical profilometer images of stainless steel

2. Adhesion Strength

a. Effect of Surface Roughening

Table 10 and Figure 20 show the results of the adhesion tests for the surface roughness experiment set. Tests were conducted for all samples listed in Table 9. The results clearly show that samples that used a smooth surface substrate on average had higher adhesion strength values. This was true for both magnesium and stainless steel substrates. What is also important is the magnesium substrates had higher adhesion strength values that the stainless steel substrates. The error bars included with each data set in Figure 20 represent the standard deviation of the data. Originally stainless steel coatings were also going to be applied to these substrates using nitrogen. However, the deposition efficiency was extremely low and produced coatings that were not able to be adequately tested. Helium gas was used to increase the amount of energy transferred to the powder. This greatly increased the deposition efficiency on the test substrates, but due to limited supplies of helium gas and stainless steel powder, stainless steel coated samples were removed from the experiment.

Table 9. Substrate roughness experiment samples

Sample ID	Powder	Substrate	Substrate Condition
Al-S-MgG	Al-Stock	AZ31 Mg Alloy	Grit Blasted
Al-S-Mg	Al-Stock	AZ31 Mg Alloy	Smooth
Al-S-SSG	Al-Stock	316L SS	Grit Blasted
Al-S-SS	Al-Stock	316L SS	Smooth

Table 10. Results from substrate roughness experiment

	Mean % Adhesive Failure	Mean Adhesion Strength (MPa)		STD (MPa)
Al-S-MgG	65	13.16	±	2.19
Al-S-Mg	60	14.85	±	1.98
Al-S-SSG	100	9.25	±	1.27
Al-S-SS	88	11.48	±	1.09

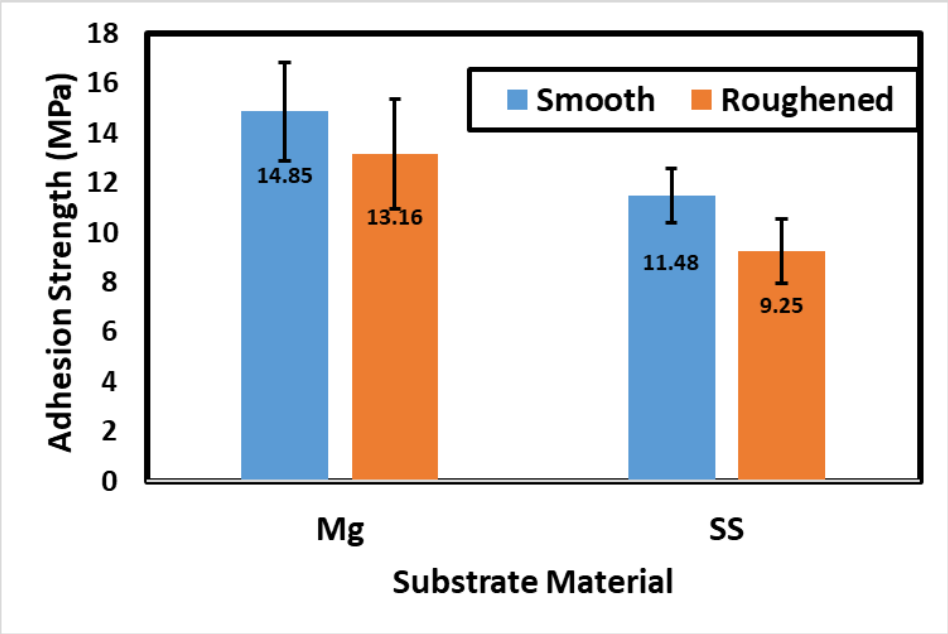

Figure 20. Graph of surface roughness results with aluminum coating

b. Effect of Substrate Hardness

Table 11 lists all samples that were used in the substrate hardness experiment. The results of this experiment are shown in Table 12 and Figure 21. No clear correlation between substrate hardness and cold sprayed coating adhesion strength exists. However, magnesium, the softest material, had the highest adhesion strength. This matches the trend seen in Figure 20. The standard deviation for the aluminum sample was high, but generally appeared to be statistically equal to steel. The error bars included with each data set in Figure 21 represent the standard deviation of the data. The coating on the copper substrate did not properly adhere to the substrate surface and produced very low results. The data for the copper substrate was not included in the analysis.

Table 11. Substrate hardness experiment

Sample	Powder	Substrate	Substrate Condition
Al-S-Mg	Al-Stock	AZ31 Mg Alloy	Smooth
SS-S-Mg	SS-Stock	AZ31 Mg Alloy	Smooth
Al-S-SS	Al-Stock	316L SS	Smooth
SS-S-SS	SS-Stock	316L SS	Smooth
Al-S-Cu	Al-Stock	110 Cu	Smooth
SS-S-Cu	SS-Stock	110 Cu	Smooth
Al-S-Al	Al-Stock	AA5083 Al	Smooth
SS-S-Al	SS-Stock	AA5083 Al	Smooth

Table 12. Results from substrate hardness experiment

	Mean % Adhesvie Failure	Mean Adhesion Strength (MPa)		STD (MPa)
Al-S-Mg	60	14.85	±	1.98
SS-S-Mg		Glue Failure		
Al-S-SS	88	11.48	±	1.09
SS-S-SS	87	17.44	±	2.60
Al-S-Cu	100	2.54	±	0.40
SS-S-Cu		No attempt		
Al-S-Al	88.75	10.47	±	2.84
SS-S-Al		Glue Failure		

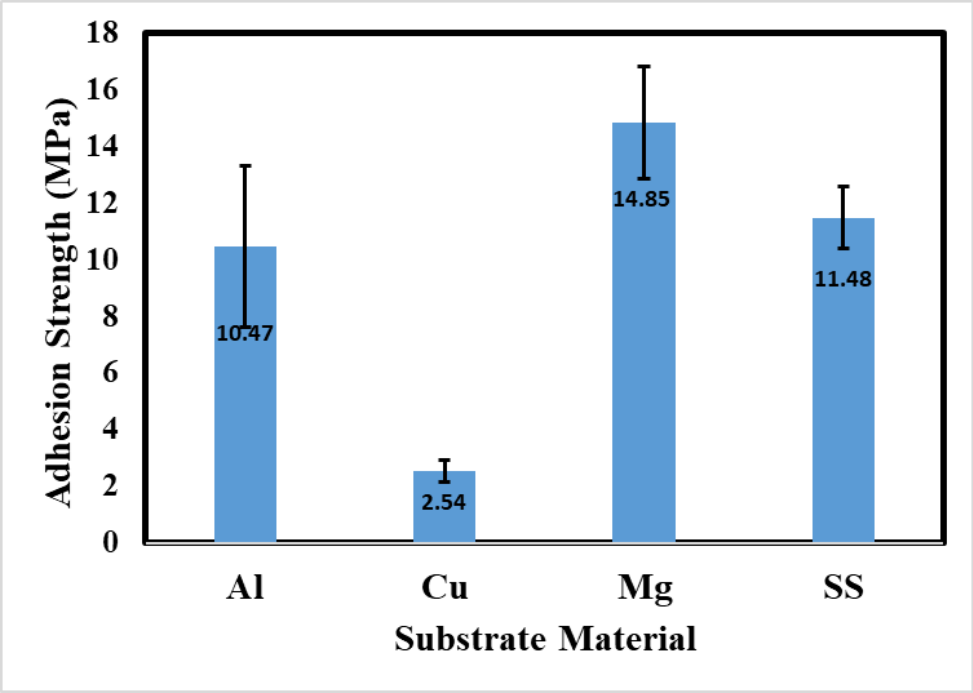

Figure 21. Graph of substrate hardness results with aluminum coating

The original experimental plan called for aluminum and stainless steel coatings within the substrate hardness experiment to determine if the hardness of the powder affected the coatings adhesion strength. Using nitrogen gas, the stainless steel powder produced thin, non-uniform coatings that were not able to be analyzed. Helium was attempted on three different substrates in order to utilize its higher specific heat. This should have transferred more heat to the stainless steel powder, making it more ductile, improving coating uniformity and adhesion. However, due to limited supplies and the cold spray modules heater capacity, the gas pressure and temperature were not able to get high enough to make an adequate coating thickness. As a result, stainless steel coating samples were removed from this experiment. There was, however, a noticeable increase in uniformity after switching from nitrogen to helium. The hardness of the aluminum samples are shown in Table 13. There was not significant change in coating hardness between different substrate. The standard deviation between the found samples was 3.573.

Table 13. Aluminum coating hardness

Substrate	Vickers (mean)	STD
Mg	47.1	5.1
Al	54.9	6.7
Cu	53.4	9.6
SS	54.0	8.5

c. Effect of Particle Size Distribution

Figures 22–24 show SEM images of the three different size distributions used for each powder type. All three match the expected particle distribution shown in Figures 13–15. The stainless steel powder was the most spherical of the three and had the smallest difference between its fine and coarse particles. The aluminum powder was the most elongated with the largest different between its fine and coarse particle ranges. The copper powder was the most irregular shaped. The irregular shapes are most likely due to bonding of small particles of copper into larger sizes during the manufacturing process.

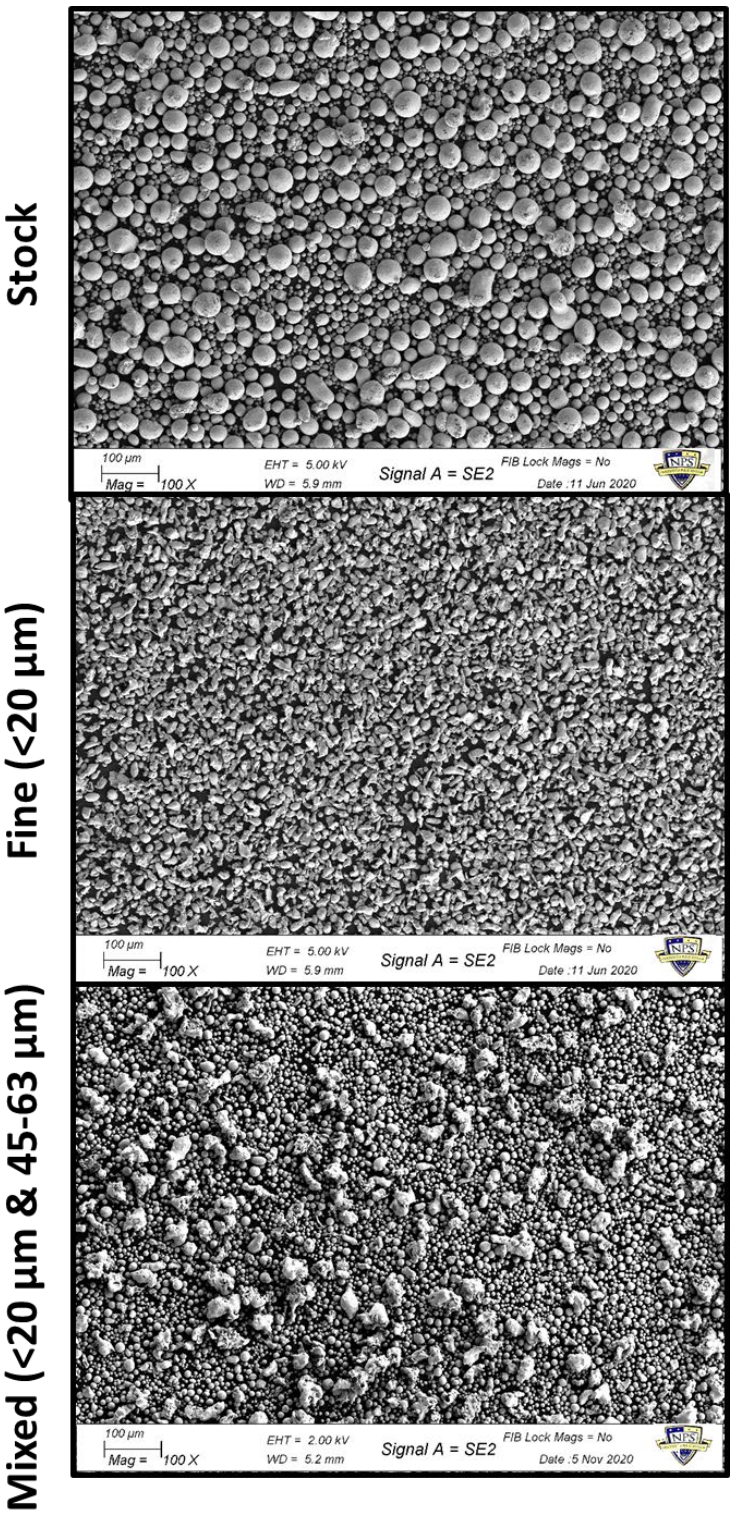

Figure 22. Stainless steel powder size distributions

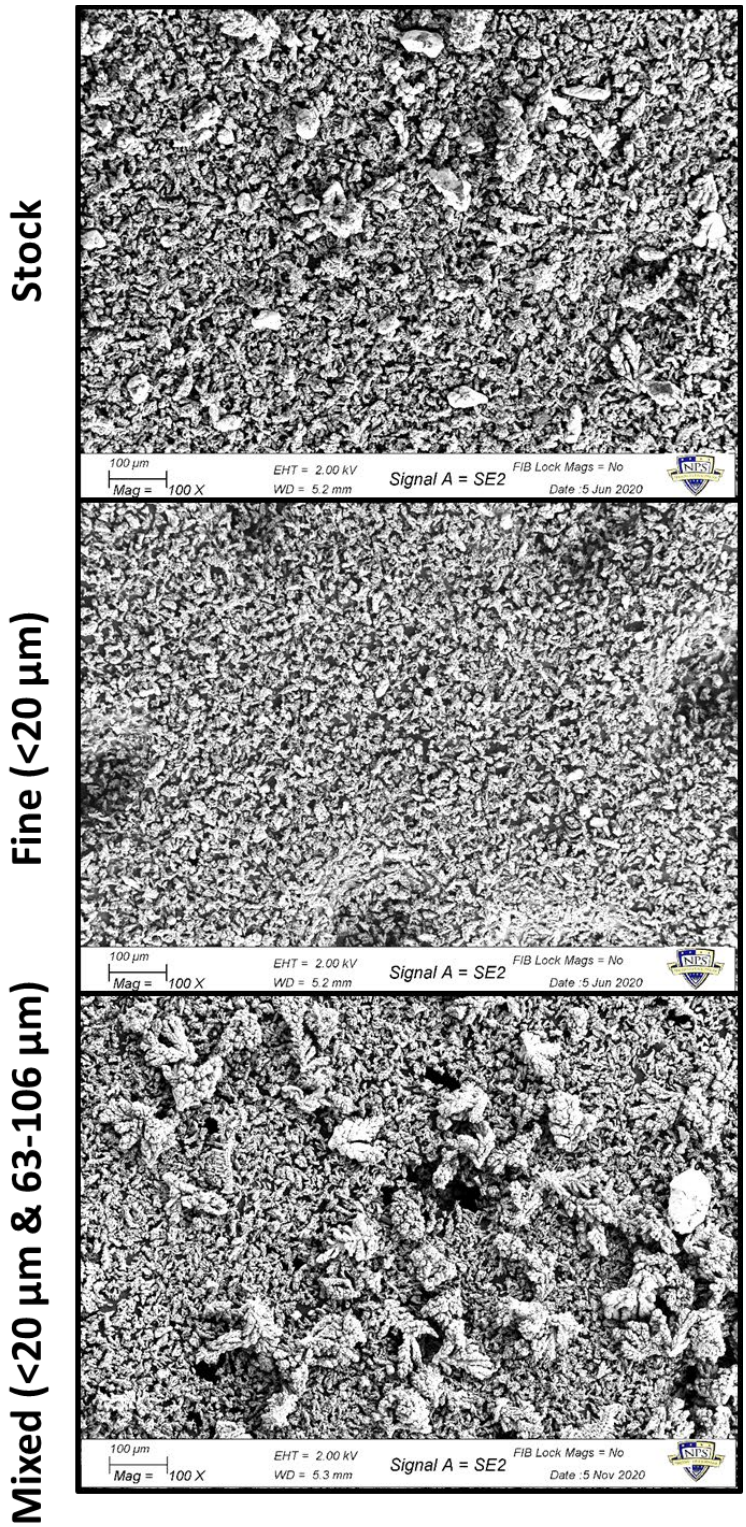

Figure 23. Copper powder size distributions

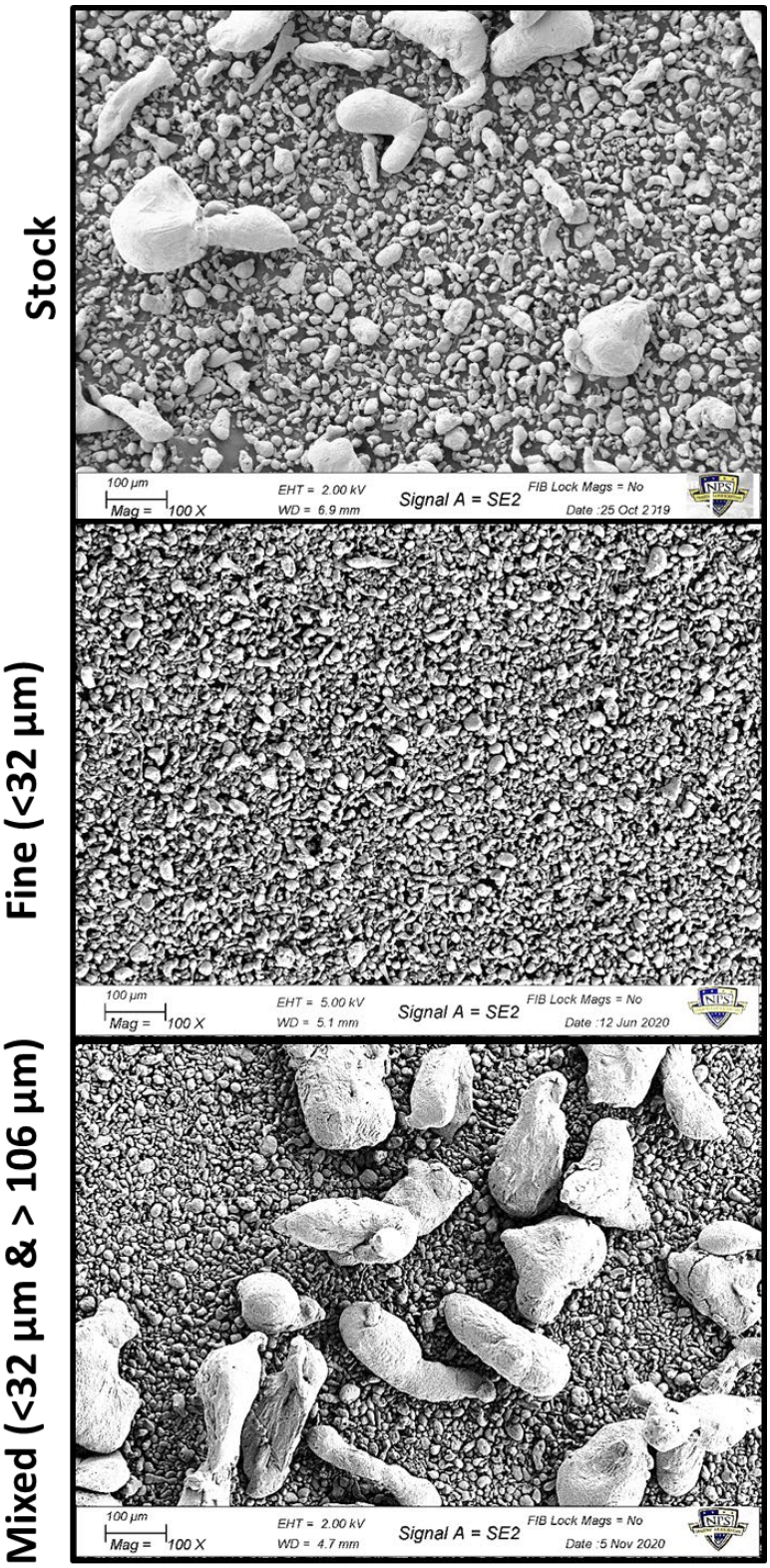

Figure 24. Aluminum powder size distributions

Table 14 lists each sample that was a part of the particle size distribution experiment. The results of this experiment are shown in Table 15 and Figure 25. The samples that used copper powder had the smallest standard deviation. The copper powder showed an increase in adhesion strength using fine and mixed powder morphology. However, the aluminum powder samples showed the highest adhesive strength using the stock powder, followed by the mixed powder morphology. Each aluminum sample had a much larger standard deviation when compared to the copper samples. The error bars included with each data set in Figure 25 represent the standard deviation of the data.

Originally stainless steel coatings were also going to be applied to these substrates using nitrogen. However, the deposition efficiency was extremely low and produced coatings that were not able to be adequately tested. Helium gas was used to increase the amount of energy transferred to the powder. This greatly increased the deposition efficiency on the test substrates, but due to limited supplies of helium gas and stainless steel powder, stainless steel coated samples were removed from the experiment.

Table 14. Particle size distribution experiment results

Sample	Powder	Substrate	Substrate Condition
Cu-S-Mg	Cu-Stock	AZ31 Mg Alloy	Smooth
Cu-F-Mg	Cu-Fine	AZ31 Mg Alloy	Smooth
Cu-M-Mg	Cu-Mix	AZ31 Mg Alloy	Smooth
Al-S-Mg	Al-Stock	AZ31 Mg Alloy	Smooth
Al-F-Mg	Al-Fine	AZ31 Mg Alloy	Smooth
Al-M-Mg	Al-Mix	AZ31 Mg Alloy	Smooth

Table 15. Results of particle size distribution experiment

	Mean % Adhesvie Failure	Mean Adhesion Strength (MPA)		STD (MPa)
Cu-S-Mg	96.67	4.14	±	0.25
Cu-F-Mg	82.00	7.38	±	0.35
Cu-M-Mg	88.33	6.50	±	0.78
Al-S-Mg	60	14.85	±	1.98
Al-F-Mg	97.5	10.18	±	1.53
Al-M-Mg	41.67	12.16	±	3.53

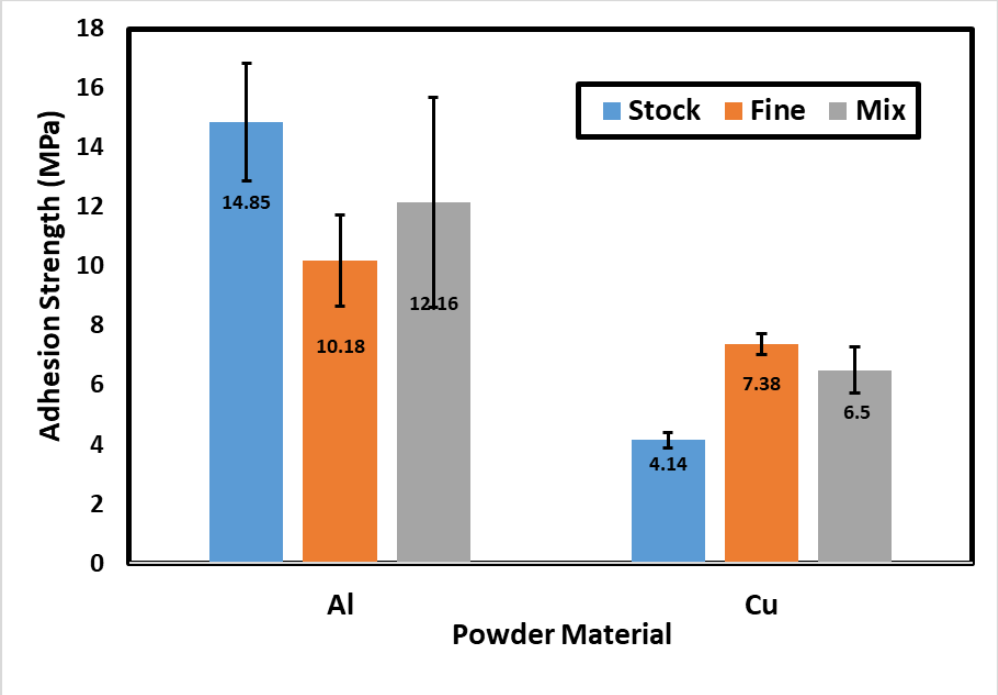

Figure 25. Graph of particle size distribution results on magnesium substrate

B. MAGNESIUM CORROSION

This section was previously published in the journal *Metals* [33].

1. Surface Roughening

Figure 26 shows the 3D morphological profiles of the three Mg samples attained via optical profilometry including the average roughness values taken from three regions across each sample. The red color indicates peaks on the surface, while the blue color represents the valleys. It can be seen that the roughened sample had a surface roughness over four-times greater than the control as-received sample. The mechanical polishing of the sample led to a decrease in the surface roughness of over one order of magnitude relative to the control as-received sample (~1/17th of the control sample).

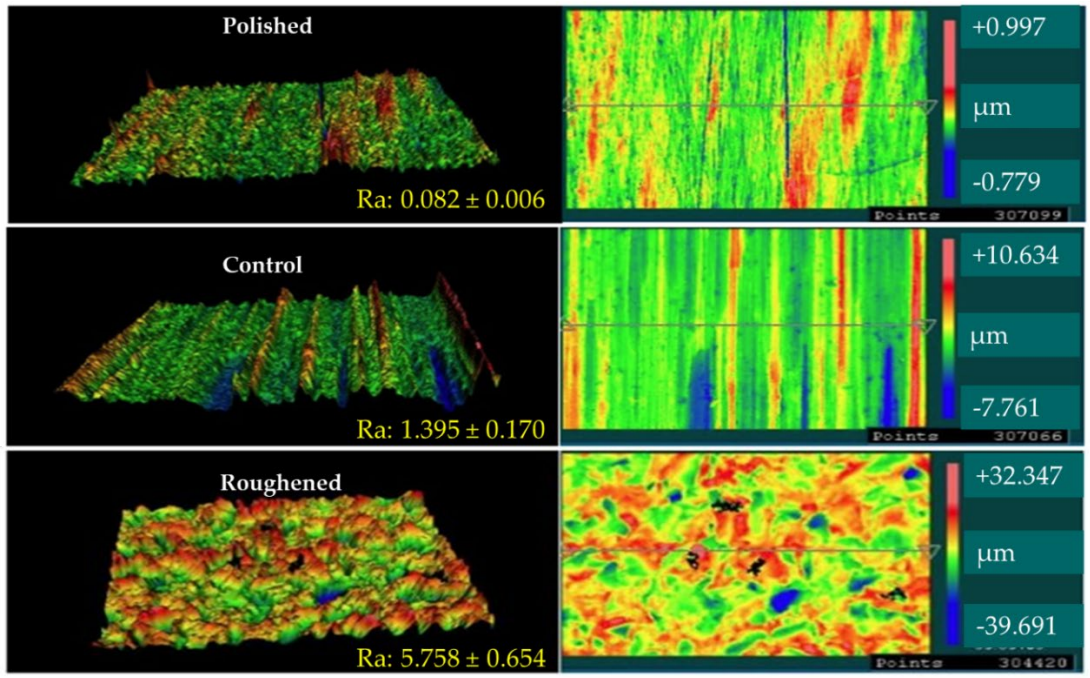

Figure 26. 3D surface profiles and height maps of Mg samples

2. Mass and Dimensional Changes during Salt Fog Exposure

Tables 16–18 present the measurements for each sample exposed to a different surface roughness treatment. Three independent measurement points were taken for each sample. The initial two rows show the data taken during the incubation period, which were not used in any analysis. Only one data point was recorded during each of those measurement periods, as such no standard deviation was calculated.

Figure 27 shows the change in mass and corrosion rate of each sample overtime during the salt fog exposure. The corrosion rate for each sample was calculated using the weight loss method using the mass at 168 h as the initial. The incubation period data were not plotted on the figure. It can be seen that the roughened sample had the highest amount of mass loss. Both the roughened and control samples experience most of their weight loss before approximately 350 h, after which the weights plateau. The polished sample, however, maintained a steady weight throughout the entire salt fog exposure. The corrosion rate for each sample followed a similar trend of intensity.

Table 16. Polished sample dimension and mass change measurements

Polish									
Time (h)	**Length (mm)**			**Width (mm)**			**Thickness (mm)**			**Mass (g)**
0	46.00			22.20			8.69			17.10
96	46.99			21.01			8.99			17.10
168	47.42	±	0.00	21.98	±	0.00	9.28	±	0.00	17.10
264	46.99	±	0.01	21.97	±	0.01	9.14	±	0.00	17.13
336	46.99	±	0.01	22.10	±	0.00	9.14	±	0.00	17.11
432	46.99	±	0.01	21.67	±	0.01	8.97	±	0.01	17.11
504	46.99	±	0.00	21.84	±	0.01	8.97	±	0.01	17.12
600	46.82	±	0.01	21.67	±	0.01	8.89	±	0.00	17.11
672	46.99	±	0.00	21.67	±	0.01	8.89	±	0.00	17.13

Table 17. Control sample dimension and mass change measurements

Control									
Time (h)	**Length (mm)**			**Width (mm)**			**Thickness (mm)**			**Mass (g)**
0	47.60			22.20			9.50			18.11
96	47.98			22.50			9.50			18.19
168	47.99	±	0.00	22.75	±	0.00	9.73	±	0.01	18.07
264	47.75	±	0.00	22.48	±	0.01	9.40	±	0.00	17.90
336	47.58	±	0.01	22.52	±	0.01	9.23	±	0.01	17.89
432	47.58	±	0.01	22.52	±	0.01	9.23	±	0.01	17.86
504	47.75	±	0.00	22.35	±	0.00	9.06	±	0.01	17.89
600	47.41	±	0.01	22.10	±	0.00	8.89	±	0.00	17.88
672	47.58	±	0.01	22.35	±	0.00	9.06	±	0.01	17.87

Table 18. Roughened sample dimension and mass change measurements

Roughened									
Time (h)	**Length (mm)**			**Width (mm)**			**Thickness (mm)**			**Mass (g)**
0	47.60			22.20			9.50			18.03
96	48.49			22.00			8.99			18.19
168	48.25	±	0.00	22.87	±	0.00	9.92	±	0.00	18.23
264	48.01	±	0.00	22.61	±	0.00	9.14	±	0.00	17.72
336	48.09	±	0.01	22.61	±	0.00	9.40	±	0.00	17.85
432	47.92	±	0.01	22.52	±	0.01	9.31	±	0.01	17.75
504	47.67	±	0.01	22.35	±	0.00	9.31	±	0.01	17.75
600	47.33	±	0.01	22.10	±	0.00	9.06	±	0.01	17.76
672	47.50	±	0.00	22.35	±	0.00	9.23	±	0.01	17.77

Throughout the time the samples were inside the salt fog chamber, a porous hydrated oxide layer formed on their surface, as seen in Figure 28. The roughened sample had the largest amount of this oxide present followed by the control sample. The amount that formed on the samples decreased over time. There is significantly more oxide present at 168 h for the roughened and control sample when compared with 504 h. At 672 h, the roughened sample had a minimal hydrated oxide layer present and the control sample had none. The polished sample did not display a hydrated oxide throughout the experiment. When compared to the profilometry data, this further confirms the correlation between surface roughness and the rate of corrosion.

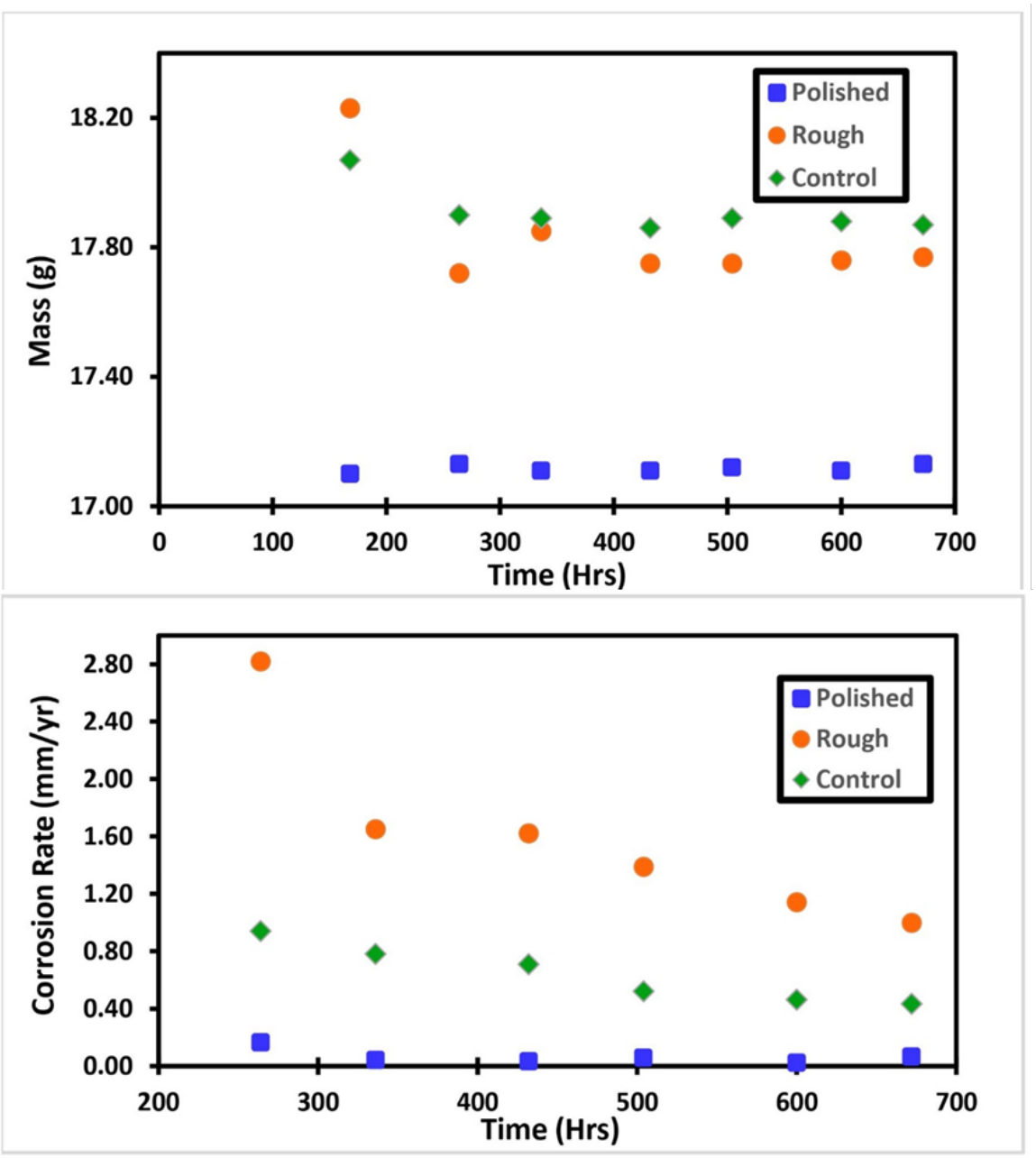

Figure 27. Mass loss of samples

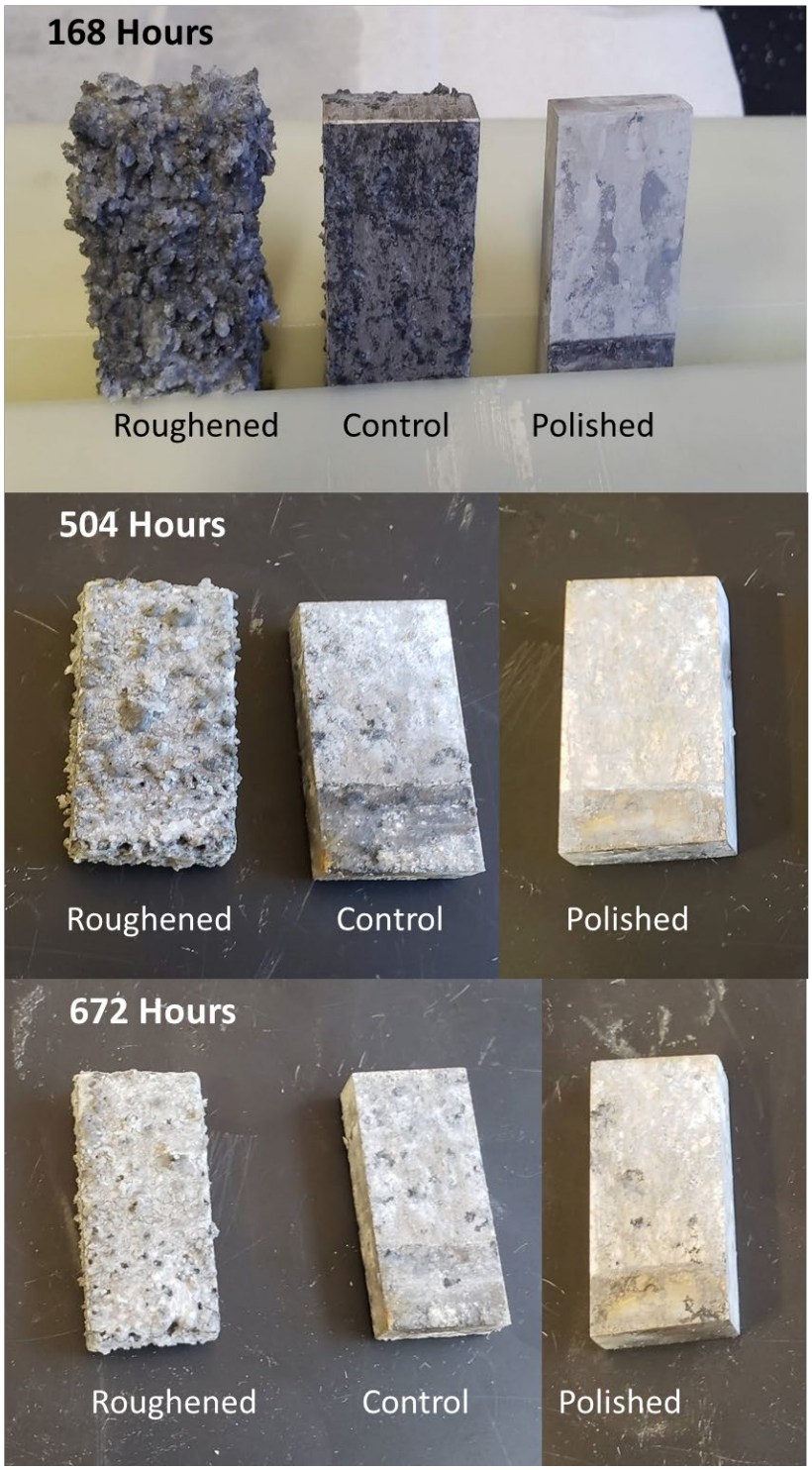

Figure 28. Samples during salt fog chamber experiment

V. DISCUSSION

A. ADHESION EXPERIMENTS

1. Effect of Substrate Roughness

It was predicted the substrates with the roughened surface would exhibit higher adhesion strengths due to increased surface area and mechanical interlocking. This increased surface area would potentially increase the metallurgical bond between the coating and the substrate. However, for both sets of substrates, the smooth, unaltered substrate surface produced the higher adhesion values. This matches the results found by Yin et al. who found that polished and ground samples have a higher adhesion strength than grit blasted samples [27]. The thickness for each sample's coating within this experiment are listed in Table 19.

Table 19. Coating thickness of samples used for evaluating surface roughness

	Coating Thickness (μm)		
Al-S-Mg	107.212	±	20.131
Al-S-MgG	133.654	±	11.907
Al-S-SS	239.423	±	23.369
Al-S-SSG	184.135	±	15.887

Figures 29 and 30 show the cross section of the fracture site for the aluminum powder samples. The two coatings have no differences in porosity. Both samples show evidence of mixed mode failure. Figure 29 has a more vertical fracture, which would normally indicate a brittle failure. However, within the vertical failure are voids that extend inward showing evidence of ductile failure.

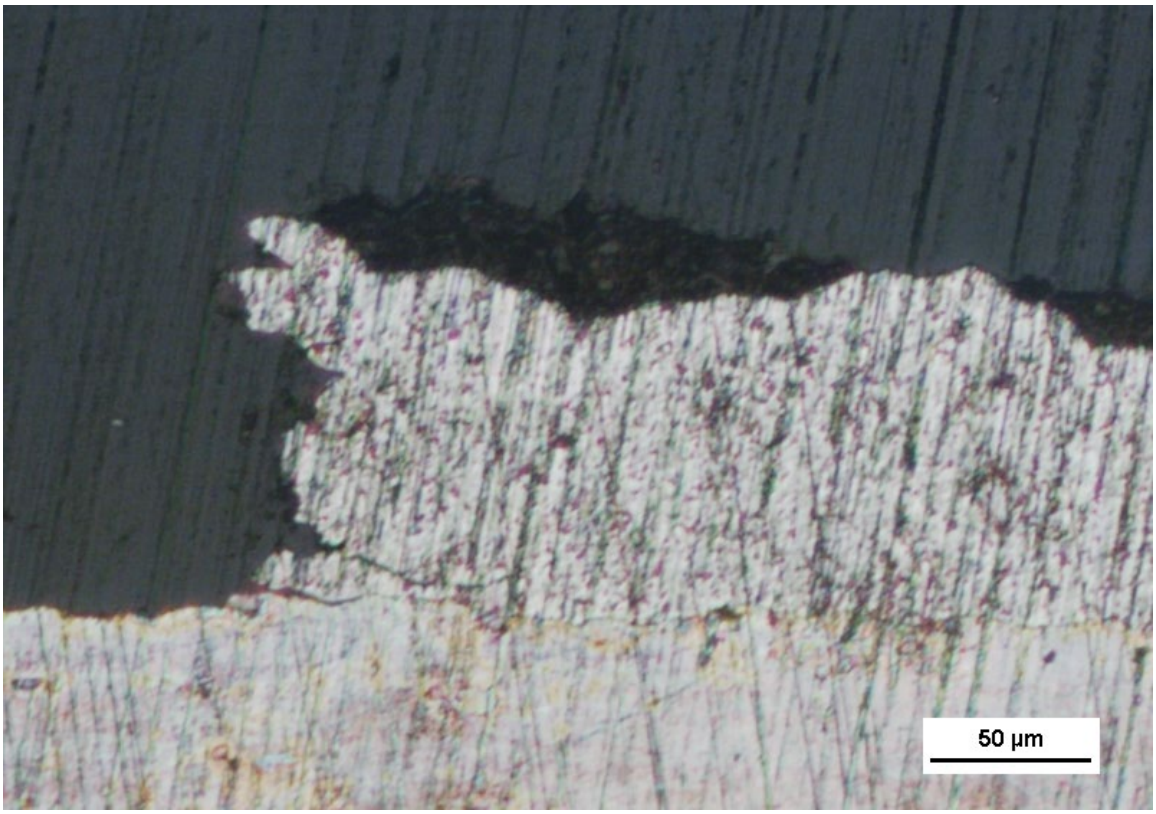

Figure 29. Al-S-Mg fracture site

Figure 30 also provides evidence of mixed mode failure. Where this sample differs is the fracture site first appears as ductile. The fracture site is at approximately 45 degrees at the location of maximum shear. This would imply the coating experience an increased amount of deformation prior to failure. This would match the adhesion results since ductile materials generally have a lower strength. This is still a mixed mode failure since within the fracture site there are areas where the failure is near vertical, a sign of brittle failure.

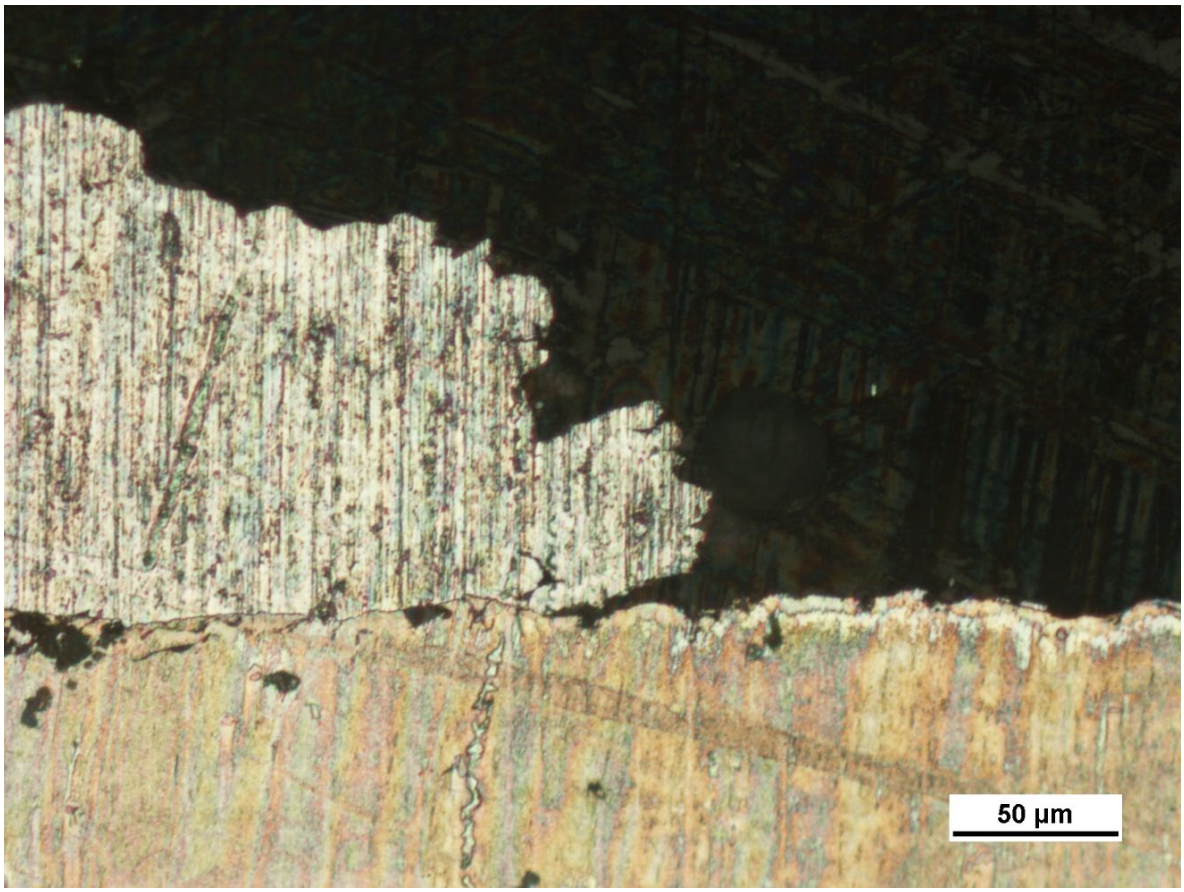

Figure 30. Al-S-MgG fracture site

Figures 31 and 32 show the fracture site for the stainless steel substrate samples. Both samples have an increased porosity density when compared to the magnesium substrate samples shown in Figures 29 and 30. Figure 32 shows that the roughened stainless steel sample has the most sever porosity. The porosity in Figure 32 is not only denser, but also larger in size. The porosity location is also of concern with the stainless steel samples. Unlike the magnesium samples, there is increased presence of porosity along the interface between the coating and the substrate. Increase porosity within the coating would increase the likely hood of cohesive failure. The porosity along the interface would explain the decrease in adhesive strength. These observations when combined with the data shown in Figure 20, shows the trend that as porosity increases, the strength of the coating decreases.

Both of the coatings on stainless steel substrates show evidence of mixed mode failure. Both coatings at first appear to be primarily brittle failure since the fracture site is approximately vertical. Figure 31 shows some angle along the fracture site, but that is most likely a result of cohesive failure since half the fracture site is vertical. Each coating had similar evidence of mixed mode failure within the fracture site, as seen in Figures 29 and 30.

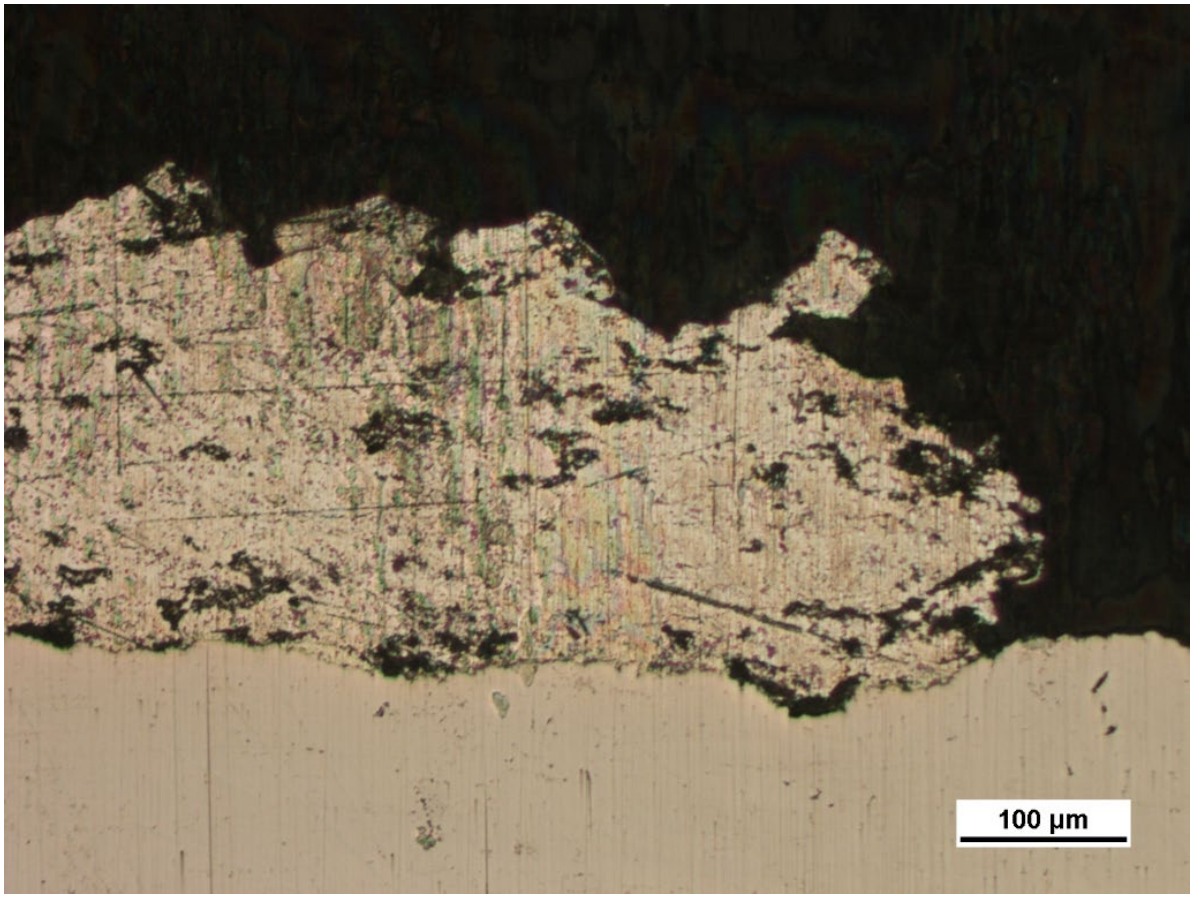

Figure 31. Al-S-SS fracture site

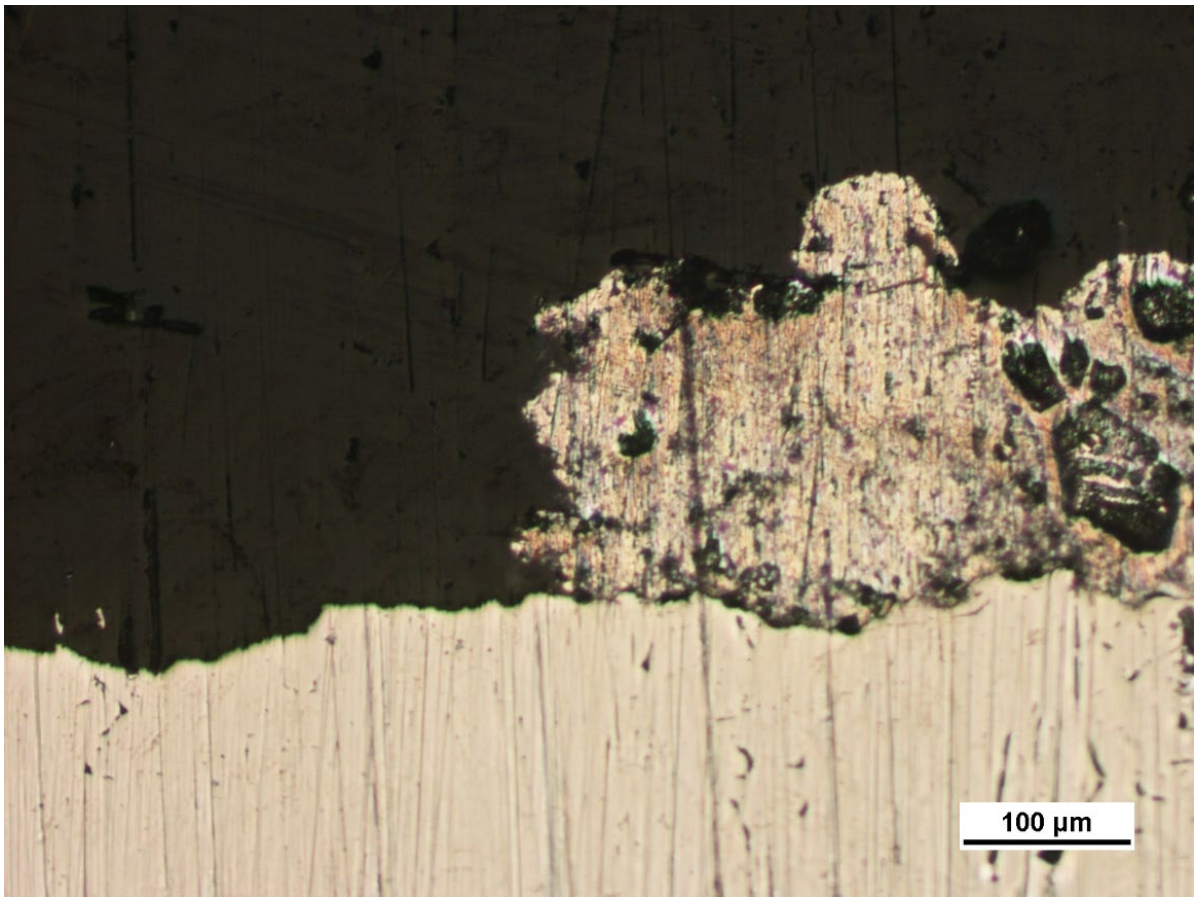

Figure 32. Al-S-SSG fracture site

Figures 33–36 show dark field images of the interface between the coating and the substrate for each sample. Figures 33 and 34 show little variation between the two. They both show a small line of increased contrast between the coating and substrate. This could indicate a separation between the two materials. However, Figures 29 and 30 clearly show that there is a good bond at the interface. The increased contrast is most likely a small amount of micro-galvanic corrosion caused from the contact between aluminum and magnesium while being exposed to water during the polishing process and the atmosphere while in storage.

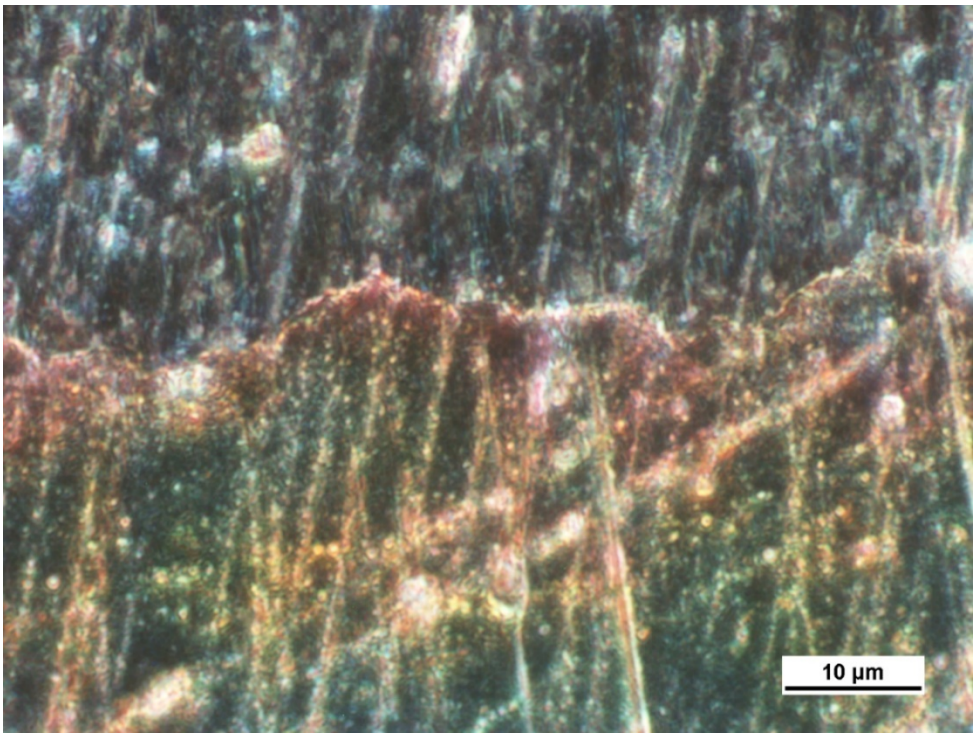

Figure 33. Dark field image of Al-S-Mg coating-substrate interface

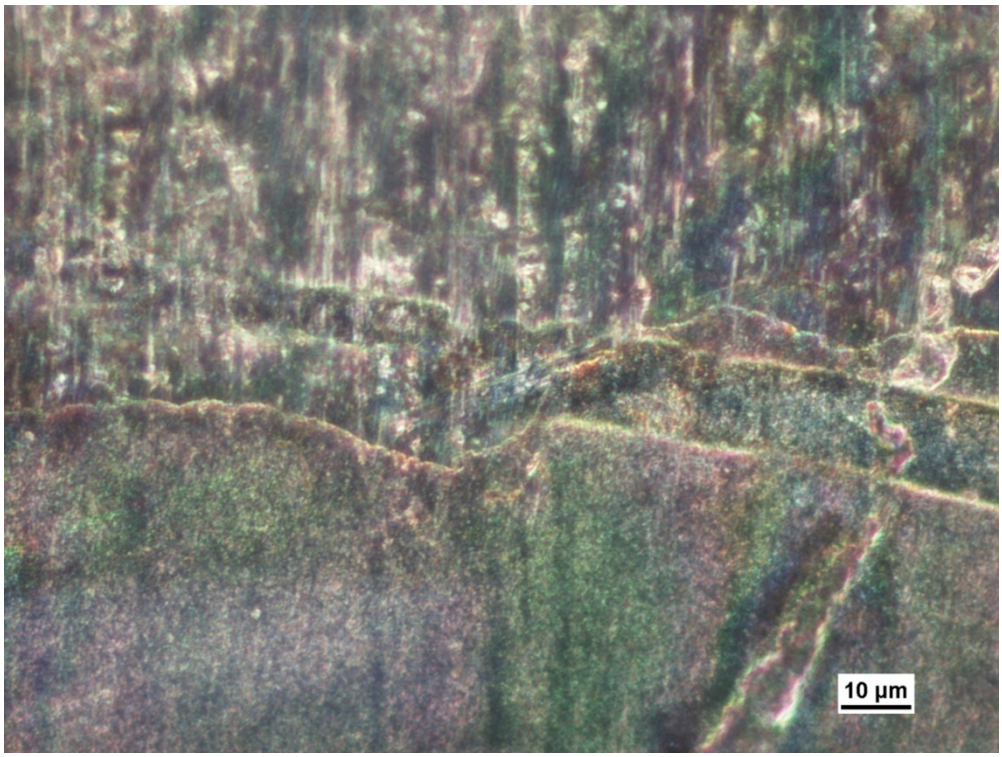

Figure 34. Dark field image of Al-S-MgG coating-substrate interface

Figure 35 and 36 show little to no change in contrast along the coating-substrate interface. The stainless steel substrate samples had lower adhesion strength values, so the lack of contrast does not indicate a better bond. The difference in corrosion potential between aluminum and stainless steel is approximately half of the different between magnesium and stainless steel. This provides additional evidence that the contrast seen in Figures 33 and 34 is in fact corrosion that occurred during the sample preparation process.

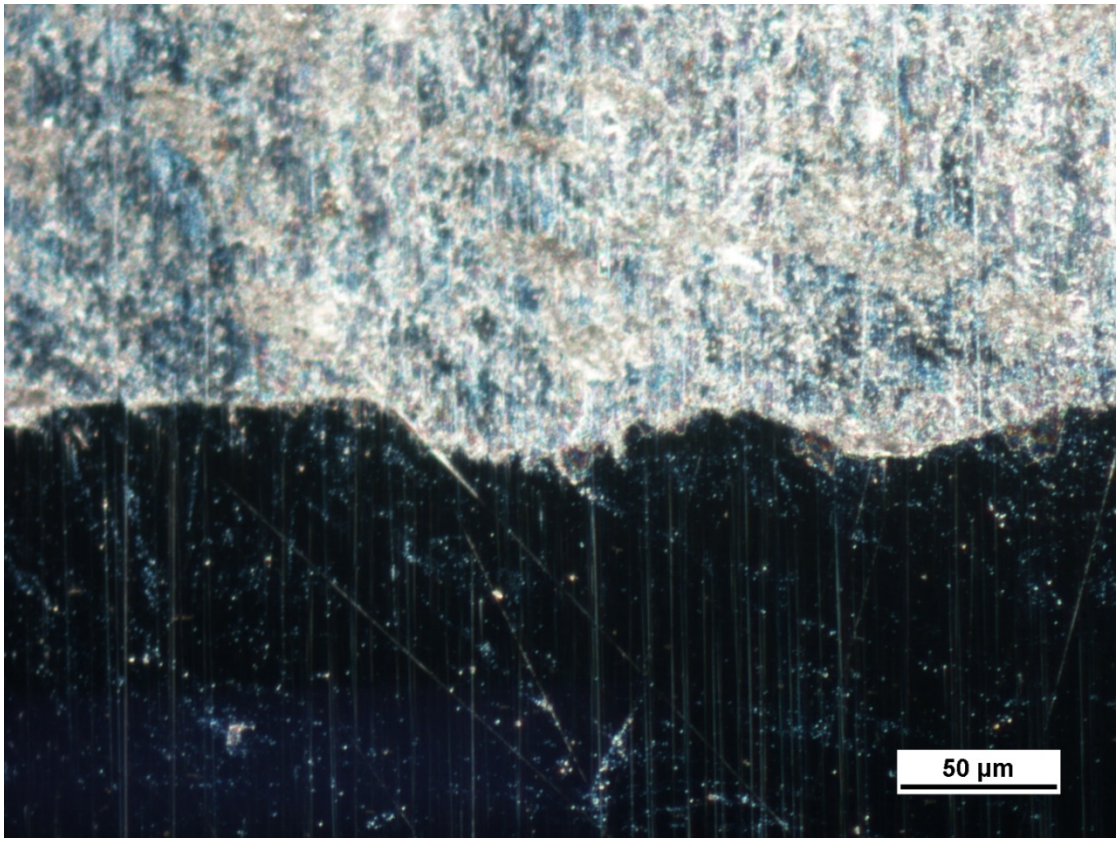

Figure 35. Dark field image of Al-S-SS coating-substrate interface

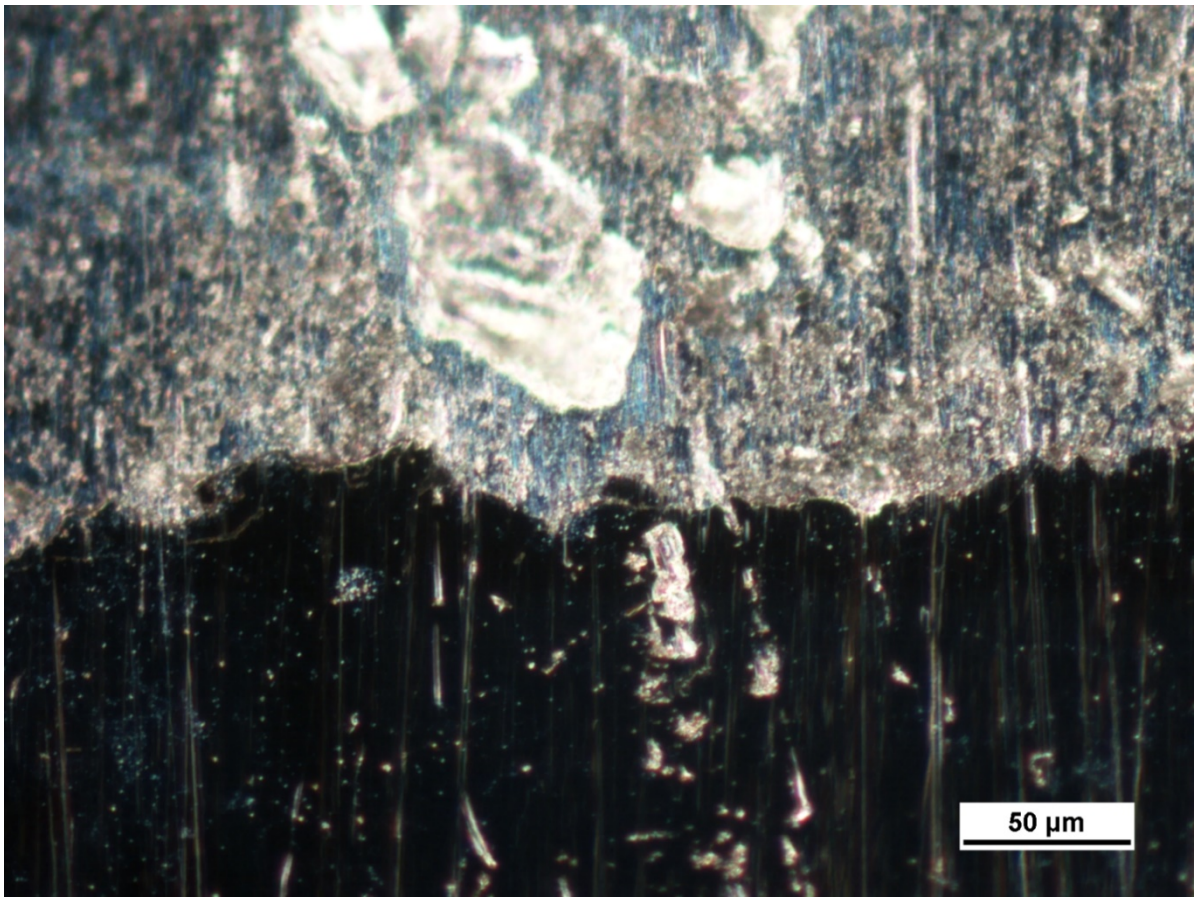

Figure 36. Dark field image of Al-S-SSG coating-substrate interface

2. Substrate Hardness

The results of this experiment were expected to show that adhesion strength increases as material hardness decreases. The magnesium, which was the softest material did have the highest adhesion strength, but stainless steel produced the second highest. The aluminum sample provided the lowest adhesive strength with the largest standard deviation. Table 20 shows the thickness of each sample's coating. One interesting trend that resulted from these experiments was that as the hardness of the substrate increased, its coating thickness also increased. Figures 29, 31 and 37–40 show the coatings for all four samples.

There was no direct correlation with porosity, which could have increased the thickness of the coating, since the least porous sample was the copper substrate (Figure 39) and the most porous sample was the stainless steel substrate (Figure 31). All coatings used the same spray parameters and were clearly distinguished in each image, so any deformation of the substrate surface would not have affected the coating thickness measurement. It is proposed here that as substrate hardness increase, it effected the jetting process. The equation for flow stress, equation 1.3, takes into account the strain hardening of the material by including material constants [10]. As strain hardening increases, the flow stress increases, the metallic particle acts less fluid like and does not flatten as significantly. The harder substrates did not experience stain hardening, but since they are naturally harder, they would have the same effect on the flow stress. This would explain why as the substrate hardness increased, so did the coating thickness.

Table 20. Coating thickness of samples used for evaluating substrate hardness

	Coating Thickness (µm)		
Al-S-Mg	107.212	±	20.131
Al-S-Al	200.962	±	26.345
Al-S-Cu	222.115	±	26.345
Al-S-SS	239.423	±	23.369

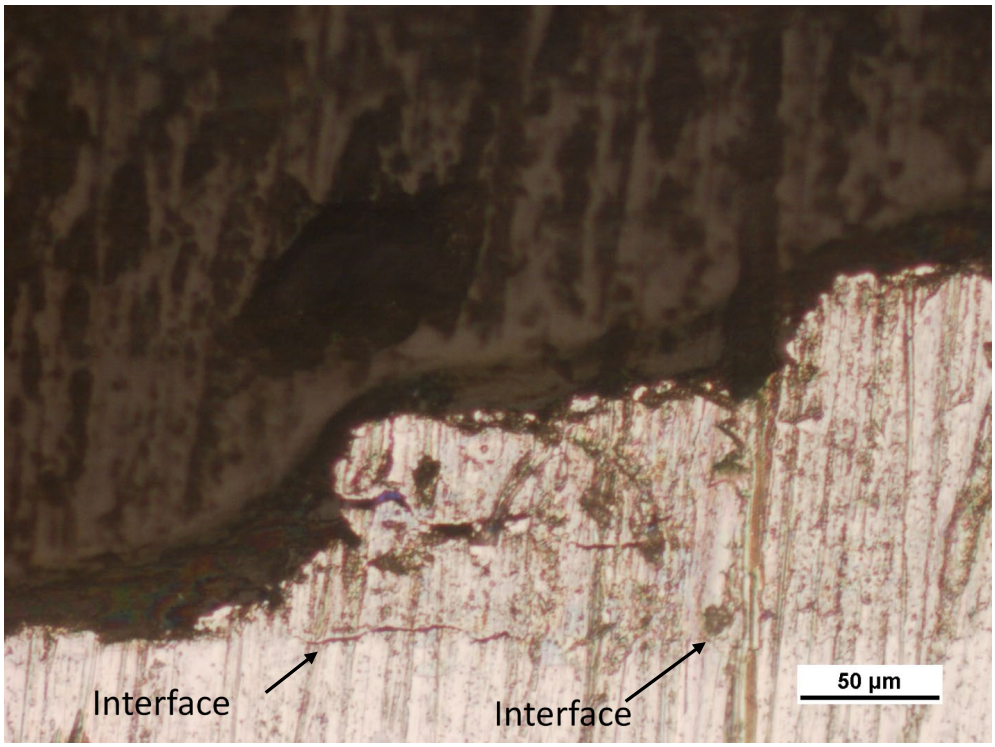

Figure 37. Al-S-Al fracture site

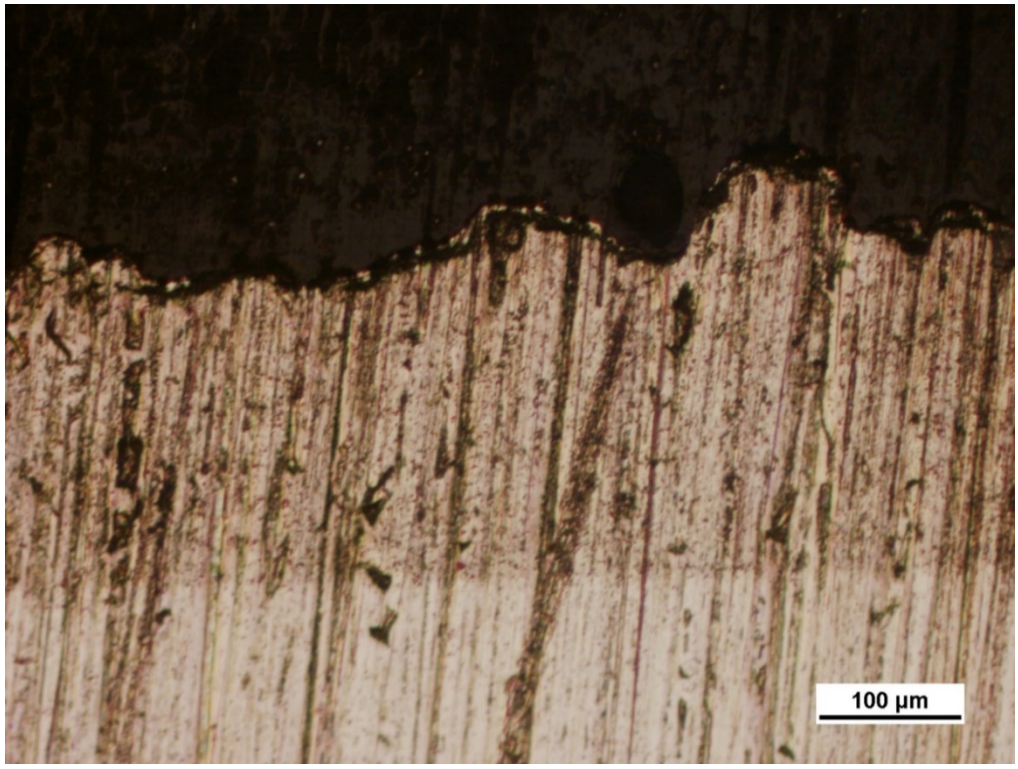

Figure 38. Al-S-Al coating

On the first attempt to spray an aluminum coating on the copper substrate, the high pressure air from the cold spray gun blew the coating off. The theory was the copper was not being heated enough to permit the aluminum to successfully adhere to the surface. To counter act this, the copper was preheated using the cold spray gun. The copper bar surface was sprayed in two passes with only nitrogen gas at 1.59 MPa and 500 °C. The aluminum powder was then immediately sprayed using the parameters listed in Table 6. The aluminum coating was not removed by the cold spray gun and showed an increase in adhesion strength. However, the results were still far lower than expected.

Figures 39 and 40 show the copper substrate sample. There were two observations of note. First, the aluminum coating on the copper substrate had the lowest porosity of any sample within this experiment. The second observation was the separation between the coating and the substrate. Corrosion may play a small role in this separation, but the primary cause is lack of adhesion between the coating and the substrate. This is supported by the adhesion results that occurred prior to any cross section that would have exposed the interface to the atmosphere.

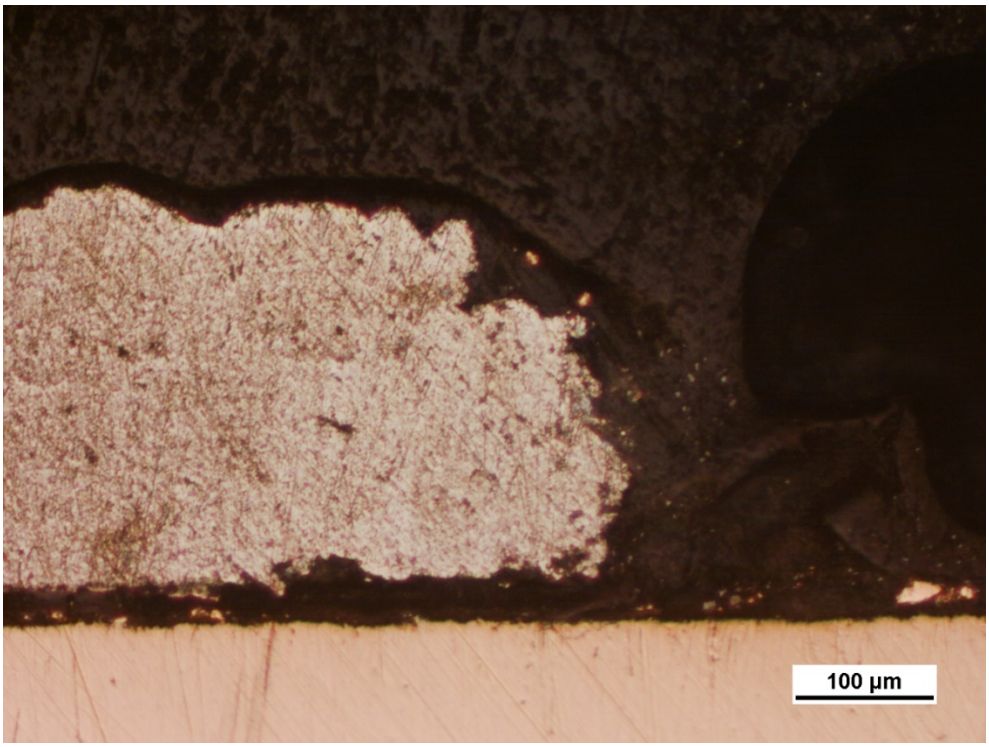

Figure 39. Al-S-Cu fracture site

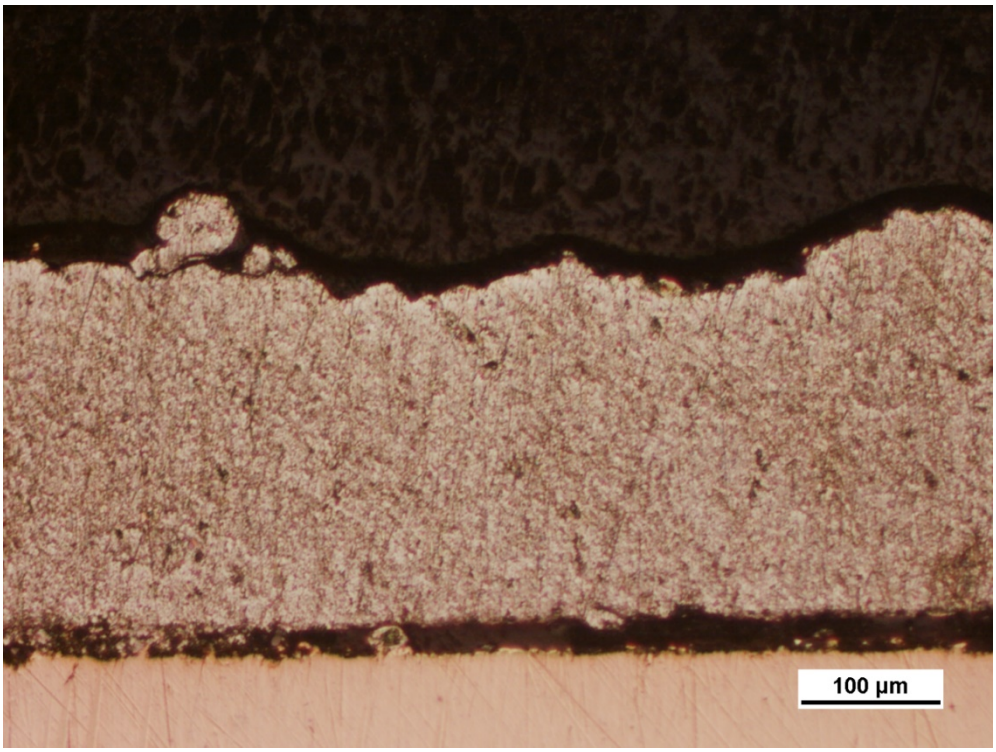

Figure 40. Al-S-Cu coating

Each substrate within this experiment was also going to be sprayed using stainless steel powder to compare the effects of hardness of the powder type on the adhesion strength. First, stainless coatings were attempted using nitrogen gas at 1.59 MPa and 500 °C. The cold spray machine has a max temperature of 550 °C. However, this only produced a very thin, non-uniform coating. An adhesion test was performed, which results in a glue failure and no visible coating. A second attempt was conducted using helium gas. The helium gas has a higher specific heat, so the theory was it would allow for a more efficient heat transfer to the stainless steel powder, increasing the powder ductility, creating a more uniform coating. One consequence of the higher specific heat is that it takes more energy to heat the gas. Since the cold spray machine's heater was producing the same btu/h, it took longer and required more energy for the gas to heat up. As a result, the max temperature that could be reached was reduced. To reach higher temperatures, the pressure of the gas had to be reduced. This reduced the speed of the gas and allowed the heater more time to heat the gas to the desired temperature. The final values used are listed in Table 6.

The results of using helium gas were positive. The coating was much more uniform on all samples. For this test set, magnesium, stainless steel, and aluminum were used as the substrates. Adhesion tests were performed on all three samples. The stainless steel substrate resulted in 87% average adhesion failure, with a mean adhesion strength of 17.44 MPa, and a standard deviation of 2.62 MPa. This is significantly higher when compared to the aluminum coating on the same substrate with only had a mean adhesion strength of 11.48 MPa. This indicates that harder cold spray powders may produce coatings with higher adhesion strengths. However, with only one successful substrate, no definitive conclusion can be made. The aluminum and magnesium substrate samples resulted in glue failures. Glue remained on both the substrate and the dolly. This could indicate a cohesive failure of the glue. One theory is the glue failure only occurred because of its tensile limit. The samples using aluminum powder show a loose trend of softer substrates producing higher adhesion strength. If this trend is applied to the stainless steel coatings, it would imply that the aluminum and magnesium coatings would have relatively large values that may exceed the capacity of the glue in this application.

3. Particle Distribution

The final analysis of this experiment did not completely match the expected results. As seen in Figure 25, the trends between the copper powder and aluminum powder were not consistent. The thicknesses of each coating are listed in Table 21.

Table 21. Coating thickness of samples used for evaluating particle size distribution

	Coating Thickness (µm)		
Al-S-Mg	107.212	±	20.131
Al-F-Mg	165.385	±	51.122
Al-M-Mg	115.385	±	16.318
Cu-S-Mg	70.673	±	8.064
Cu-F-Mg	99.519	±	5.058
Cu-M-Mg	58.173	±	7.427

Copper powder resulted with the stock powder having the lowest adhesive strength and the fine powder being the strongest. Stock powder having the lowest values matches expectations. The fine and mixed powder distributions being approximately the same was unexpected, but still showed that a particle distribution designed to reduce porosity did increase the adhesion strength of the coating. The overall values for the copper coatings were also much lower than desired. There is no clear trend between coating thickness and adhesion strength for copper coatings within this experiment. The thickest copper coating did have the highest adhesive strength, but the second highest also had the thinnest coating.

Figures 41–44 show the failure sites for the three different copper coatings. Figures 41 and 42 show a very similar failure site. Figure 43 showed evidence of cohesive failure. The mixed particle sample had a mean adhesive failure of 88.33 percent, listed in Table 15, which is higher than the fine particle sample. All three copper coatings had the most uniform, lowest porosity coatings amongst all samples from the three experiments.

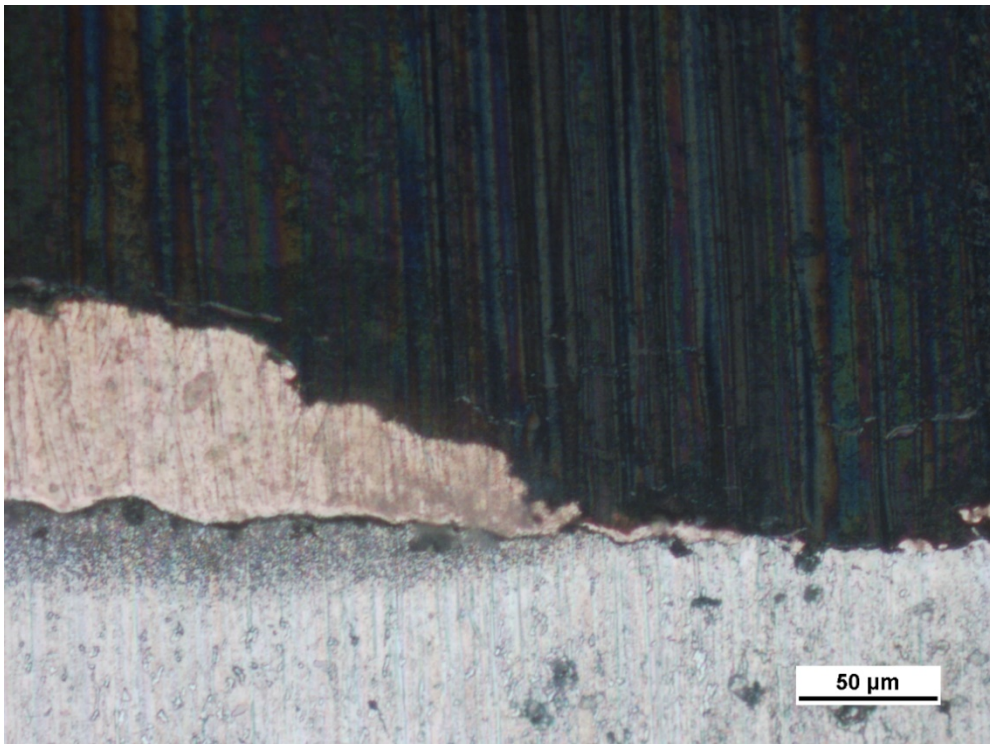

Figure 41. Cu-S-Mg fracture site

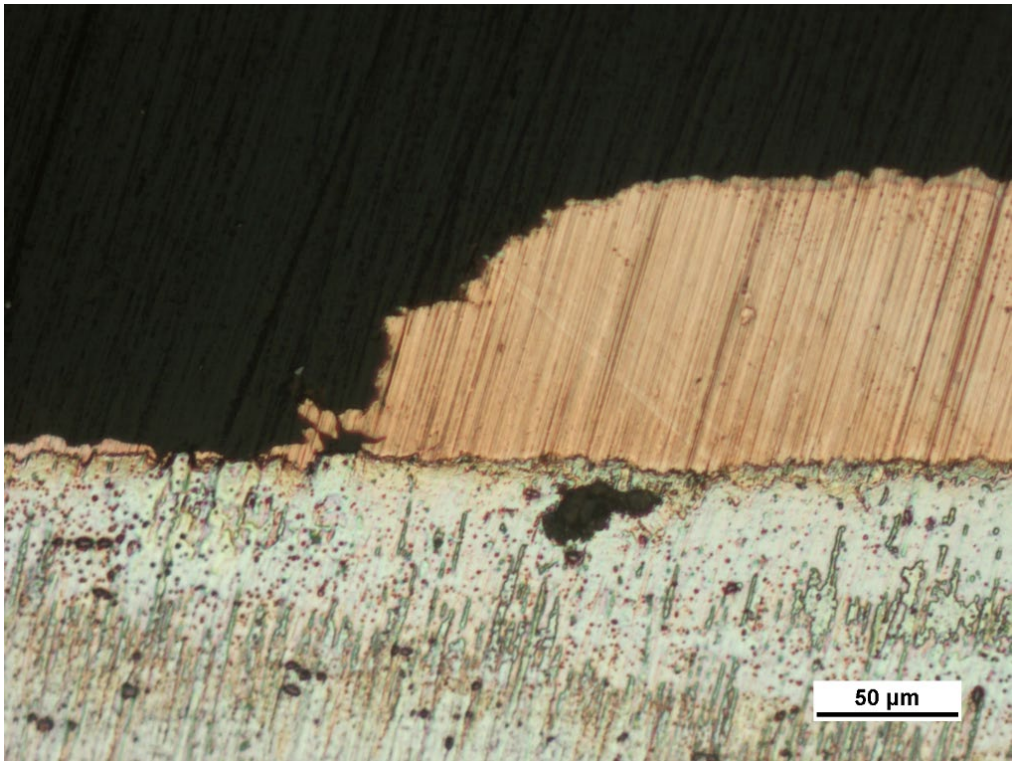

Figure 42. Cu-F-Mg fracture site

All copper coatings appear to have good adhesion at the substrate interface. There is a consistent thin black line that moves along the interface for each coating. This line is most likely a result of corrosion from the sample prep process and being exposed to the atmosphere while in storage. Figure 43 shows successful mechanical interlocking between the coating and the substrate, which supports the claim that the coating did successfully adhere to the substrate surface.

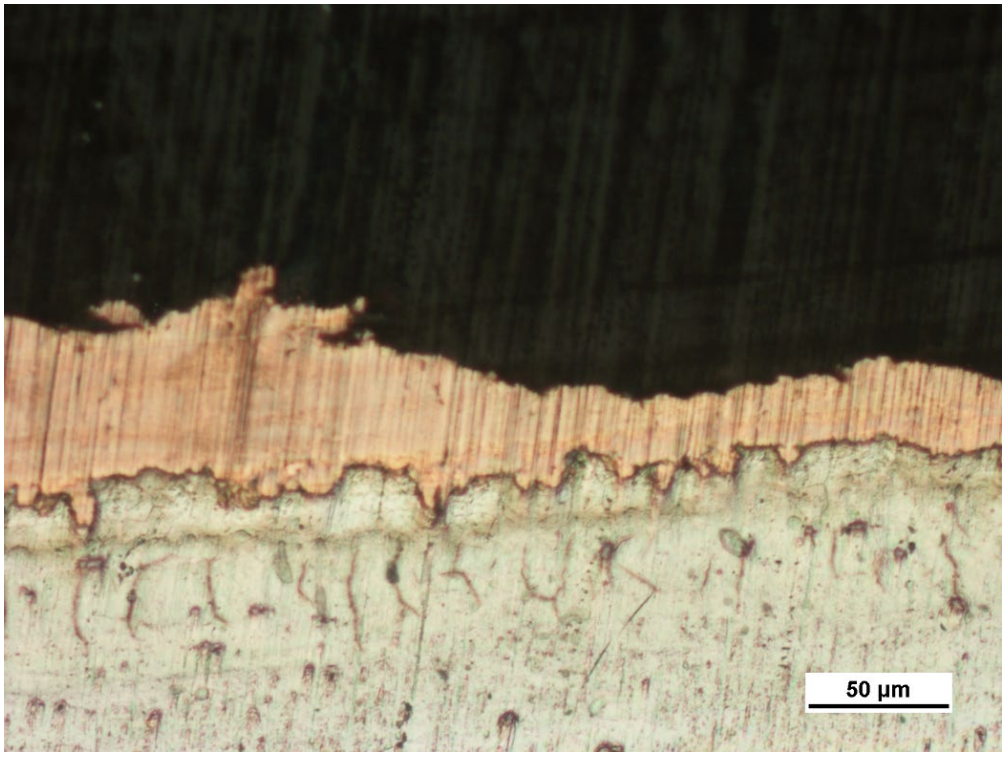

Figure 43. Cu-M-Mg fracture site

Figure 44 shows a wider view of the mix particle distribution failure surface. This sample failed initially in a cohesive manner, which gradually became an adhesive failure. Cohesive failure was seen on the other copper powder samples, but it was limited to small amounts of copper, less than 50 µm in length, distributed randomly along the substrate where the dolly was attached for the test. The failure seen on Figure 43 and 44 was most likely an anomaly and not a significant trait of the copper power or this size distribution.

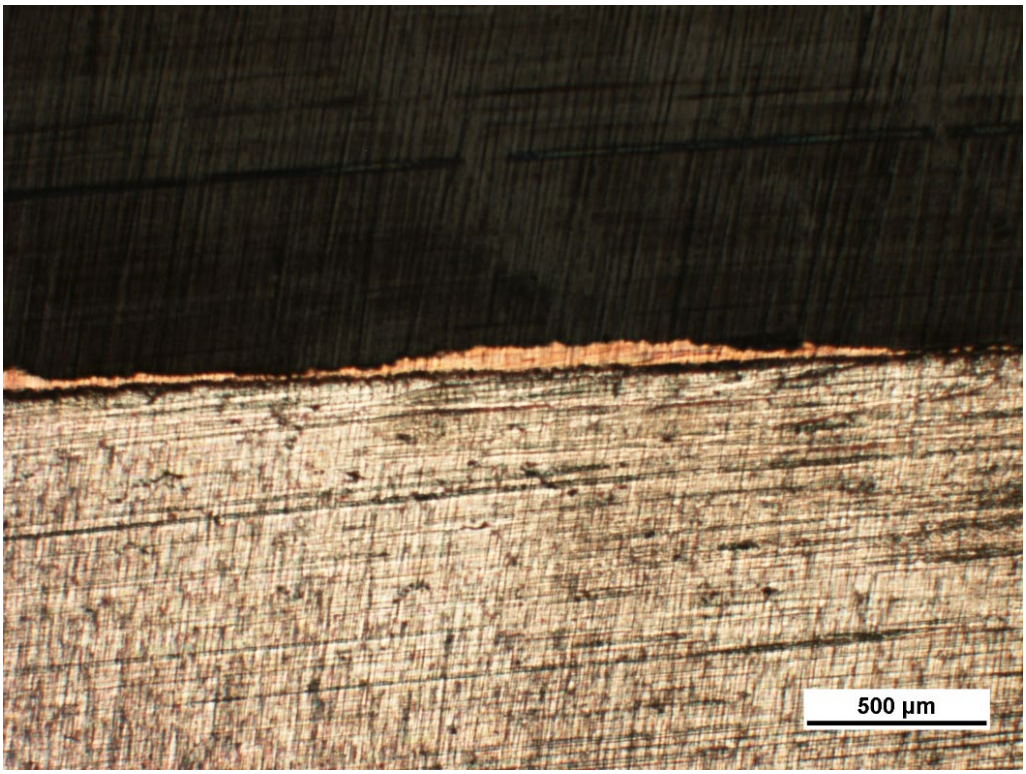

Figure 44. Cu-M-Mg fracture site at lower magnification

Figures 45–49 show the fracture sites for the three different aluminum samples. The SEM images required the cross section to the sputtered with a palladium coating approximately 0.8 nm thick. All three samples showed evidence of mixed mode failure and the adhesion strengths did not match expected. There was no significant difference in porosity between the three samples. The fine particle distribution had the thickest coating and the stock powder had the thinnest, as seen in Table 21. The standard deviation of the fine particle distribution was relatively large, but this still supports the claim that the higher the coating thickness, the lower the adhesive strength. A similar trend was displayed in the surface roughness experiment.

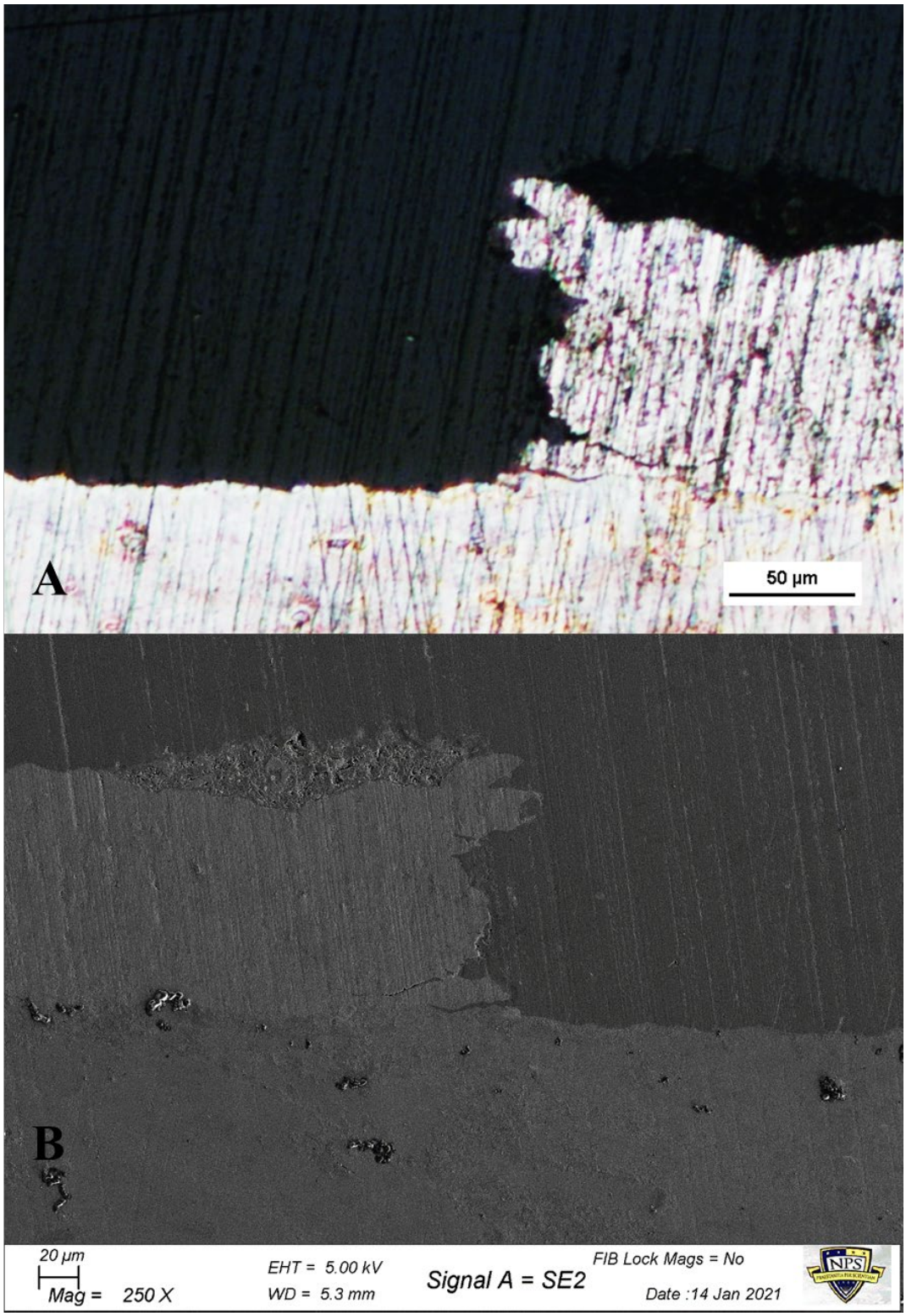

Figure 45. Al-S-Mg fracture site

The stock powder (Figure 45), had the highest adhesion strength. The fracture sites were primarily vertical, indicating a brittle failure. Within the fracture site there is evidence of ductile failure. Figured 45 shows both the optical (Figure 45A) and SEM (Figure 45B) images of similar magnification of the fracture site. The optical is a mirror image of the SEM. The comparison of the two images shows no noticeable differences between them. The fine particle distribution (Figures 46, 47) has the same observations. Since the stock powder had the highest adhesion strength and the fine particle distribution sample had the lowest adhesion strength, this observation provides no trend.

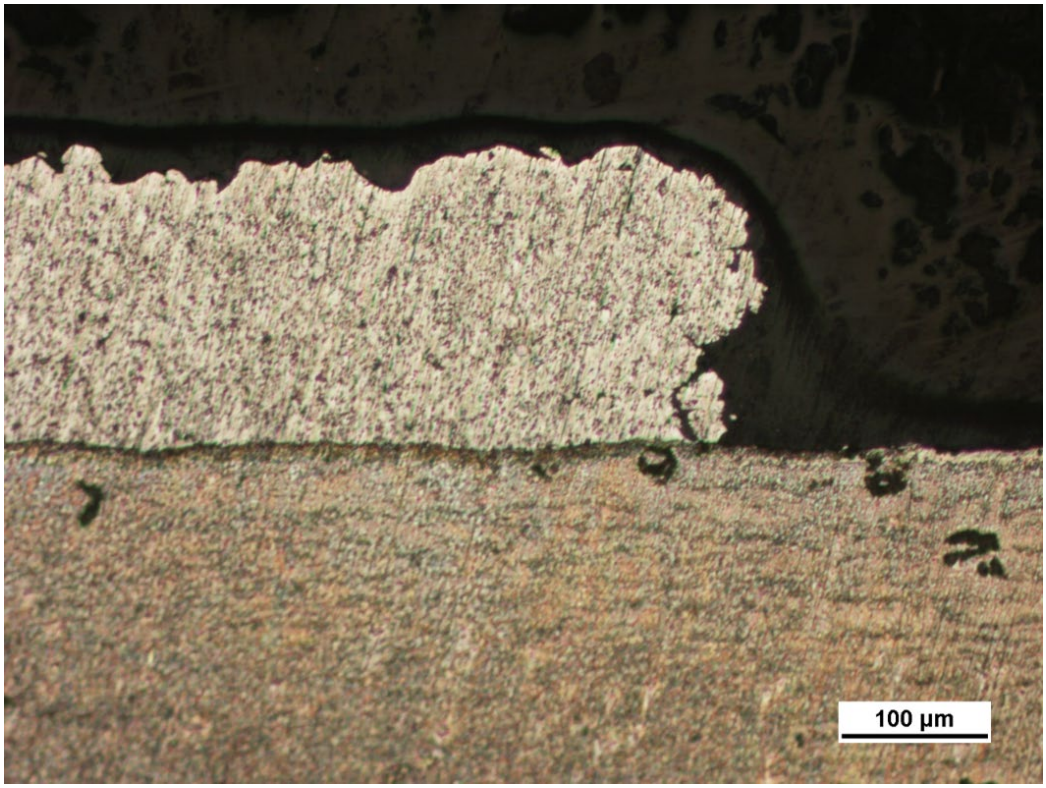

Figure 46. Al-F-Mg fracture site

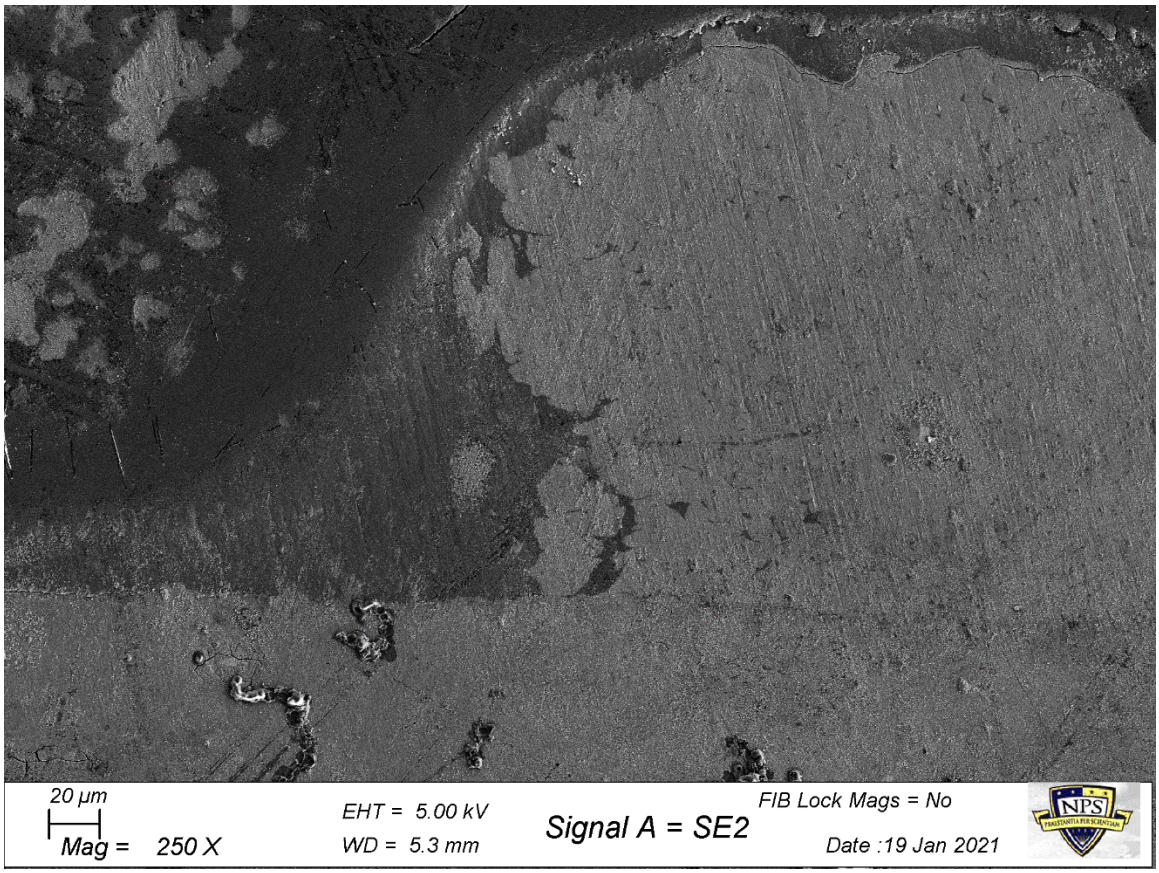

Figure 47. SEM image of Al-F-Mg fracture site

The mixed particle distribution sample (Figures 48, 49) had a fracture site at approximately a 45-degree angle. This indicates its primarily failure mode was ductile failure. Within the fracture site there is evidence of brittle failure in the form of near vertical fractures, supporting the claim of mixed mode failure.

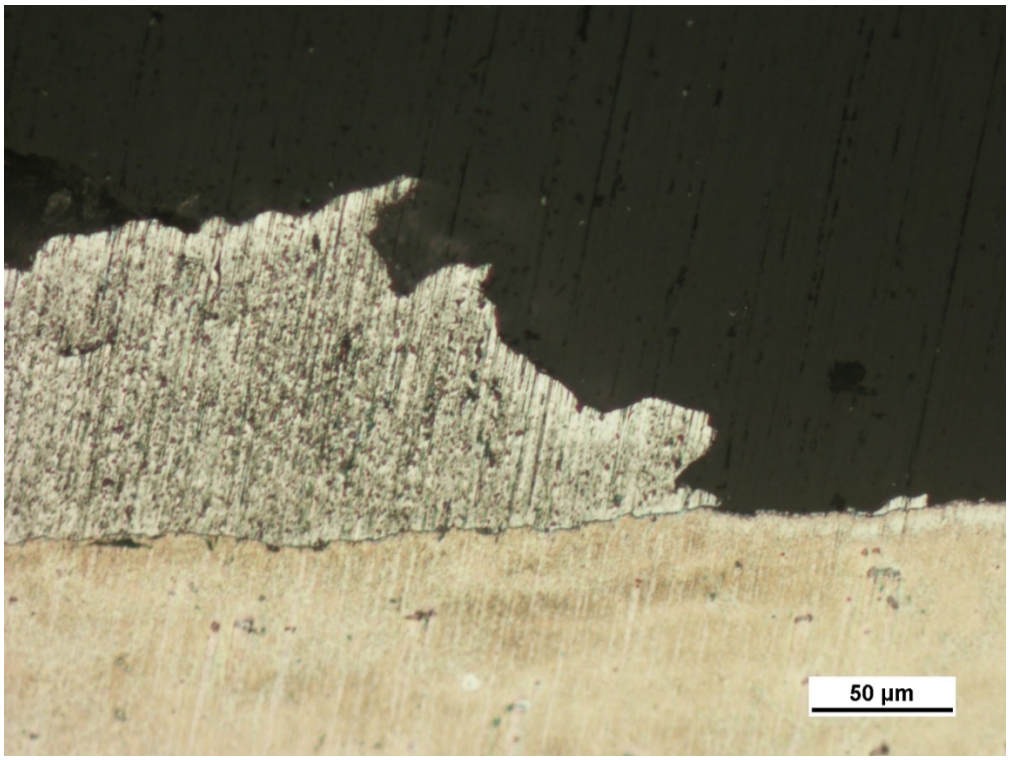

Figure 48. Al-M-Mg fracture site

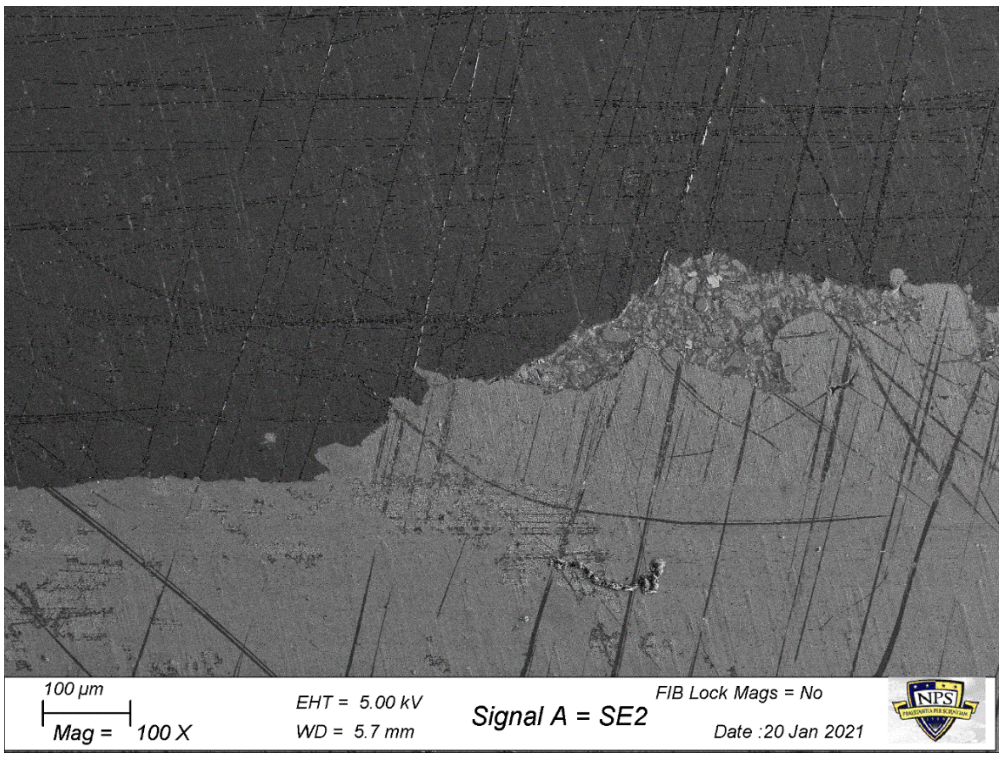

Figure 49. SEM image of Al-M-Mg fracture site

B. MAGNESIUM

This section was previously published in the journal *Metals* [33]. The formation of two oxide layers was expected to occur, based on previous reports on Mg corrosion [35], [36]. The presence of a hard crust-like MgO was expected to form on the top surface of each sample. On top of the magnesium oxide, an $Mg(OH)_2$ layer, which is a hydrated oxide layer known as brucite, was expected to form. The rate of corrosion and oxide layer formation was found to be proportional to the samples' average roughness (Ra) value. The expected corrosion reactions occurring within the salt fog environment include [35], [36]

Cathodic Hydrogen Evolution: $2H_2O + 2e^- \rightarrow H_{2(g)} + 2OH^-_{(aq)}$

Anodic Dissolution: $Mg_{(s)} \rightarrow Mg^{2+}_{(aq)} + 2e^-$

MgO Formation: $Mg_{(s)} + \frac{1}{2}O_{2(g)} \rightarrow MgO_{(s)}$

Brucite Formation: $Mg^{2+}_{(aq)} + 2OH^-_{(aq)} \rightarrow Mg(OH)_{2(s)}$

The top surfaces of both the roughened and polished samples were examined via SEM. Figure 50 shows the SEM images of the top surface of the roughened and polished samples. The top surface of the roughened sample (Figure 50A–C) had relatively large preexisting defects such as scratches, craters, and micro-crevices that served as preferential sites for pitting. This made this sample significantly more prone to pitting corrosion. The roughened sample indeed exhibited greater amounts of metallic dissolution reflected as a steady decrease in mass as well as a substantial formation and proliferation of oxide and hydrated oxide corrosion products. The corrosion on the roughened sample was much more uniform and more intrusive into the base metal. Flower-like oxide corrosion products were found in every pit. These flower-like oxide products on the sample surfaces are likely to be either MgO or brucite, as suggested by the XRD analysis presented in Figure 6. It should be emphasized that a careful examination of the literature on Mg corrosion indicated that this flower-like oxide product has not been previously observed for either MgO or $Mg(OH)_2$ formed during corrosion. However, similar flower-like oxides are seen in

manganese oxides used as electrodes for supercapacitor applications [37], [38]. The polished sample (Figure 50D–F) showed minimal amounts of corrosion. Most of the polished sample was base metal with corrosion present in isolated patches. Figure 50D shows one of the isolated oxide regions. The dashed box on Figure 50D indicates the region of the higher magnification images. The profilometer data for the polished sample indicated very minimal surface defects present on the surface. This made pitting corrosion very unlikely and sporadic. The corrosion products that were present on the polished sample exhibited greater amounts of cracking, as seen in Figure 50E,F suggesting that they may be thinner and poorly adhered to the underlying Mg metal.

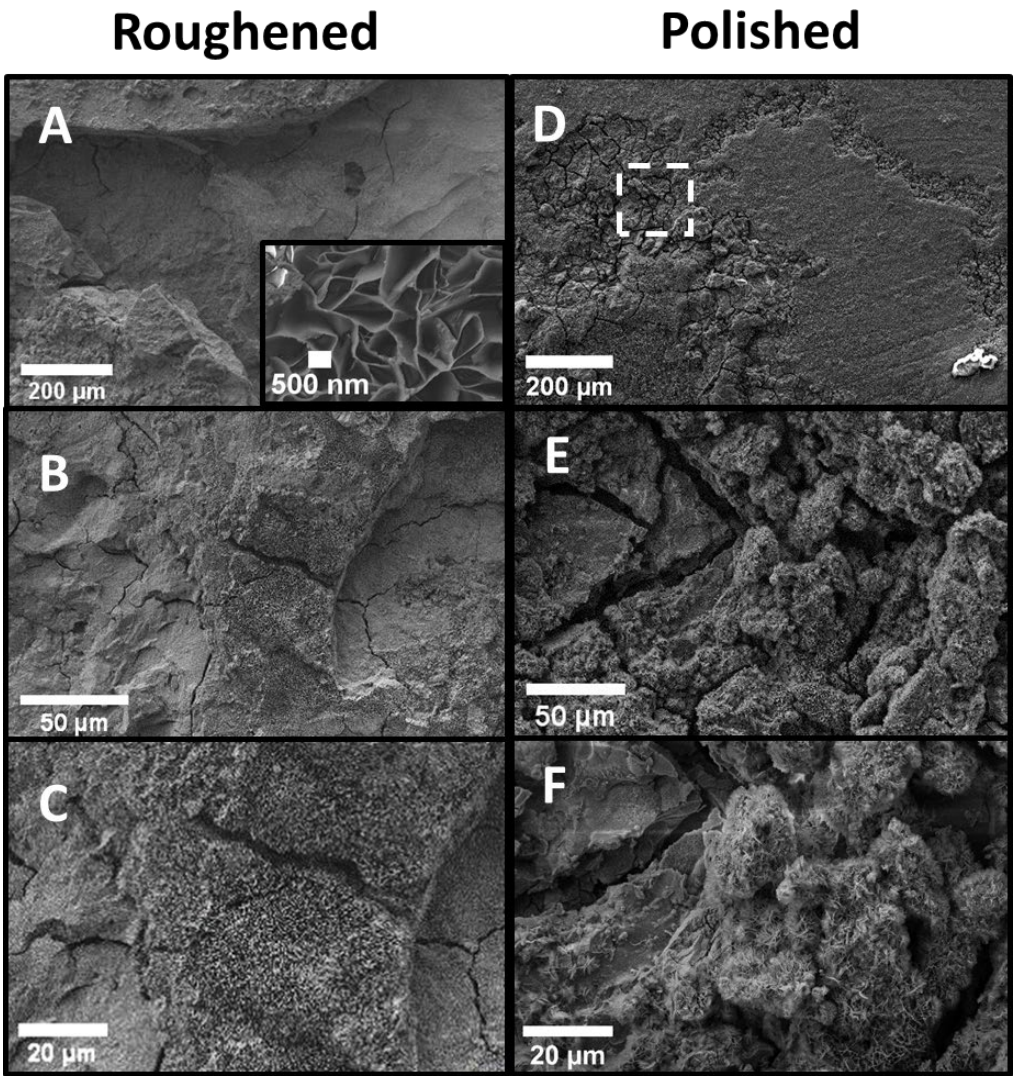

Figure 50. SEM images of the top surfaces for the control and roughened sample

At 168 h, the hydrated oxide layer from both the roughened and control samples were removed and placed in a sample bag to dry. Initially, when removed, the oxide was hydrated to the touch. When the experiment was complete after the 672 h salt fog chamber testing, the oxide looked and felt like ground chalk. Figure 51 shows images of the scraped-off hydrated oxides from the roughened and control samples. The same flower-like oxide from Figure 50 is also visible in both samples, but more developed in the roughened sample. This indicates the flower-like oxide is a characteristic of the hydrated oxide layer.

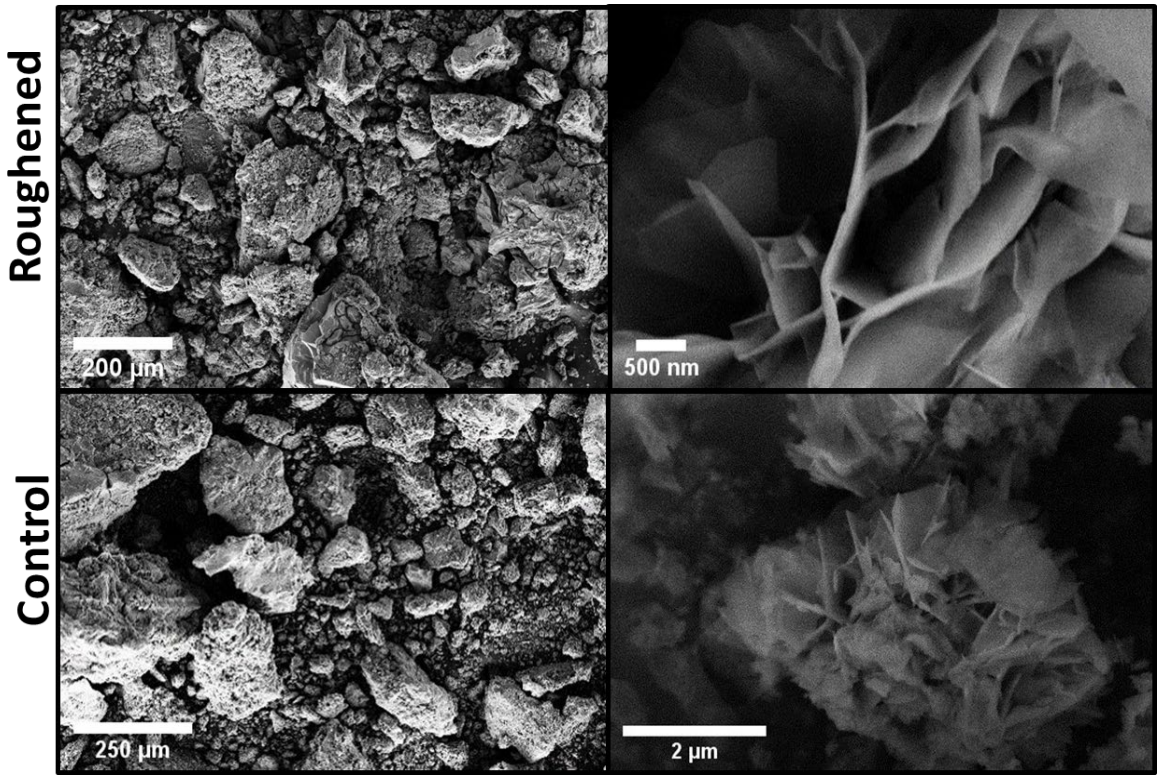

Figure 51. Hydrated oxide layer

An XRD analysis was performed on the oxide removed from the roughened sample. Oxides from both samples were analyzed with the EDS and had approximately the same weight and atomic percentages as all elements present. Figure 52 shows the XRD results that confirm the presence of brucite and magnesium oxide. These two compounds were the dominant species. Magnesium chloride, sodium chloride, and sodium oxide were also

present in smaller amounts. Sodium chloride is a result of the salt fog, and the magnesium chloride and sodium oxide are a result of the corrosion process.

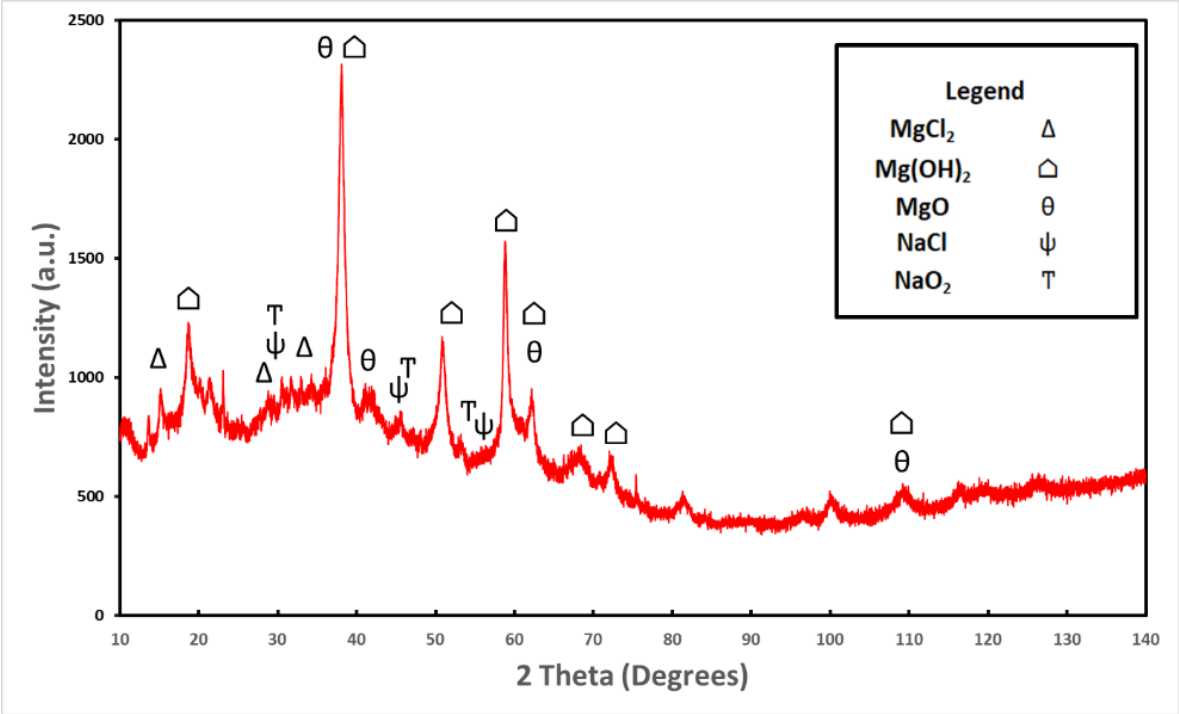

Figure 52. Oxide layer XRD analysis

The cross-sections of the three samples were examined via SEM to compare the thicknesses of the oxide layers and the intrusion into the base metal by the formed pits (Figure 53). SEM images are oriented with the substrate at the bottom, with the top portion of the images being the epoxy mounting material. SEM of the polished sample's (Figure 53E,F) cross-section shows very little defects on the surface of the sample and a sporadic oxide layer that reached ~1.5 µm into the base metal. The control sample (Figure 53C,D) shows an increase in corrosion. The images show the presence of an oxide layer and a pit that travels ~50 µm into the base metal. There is also evidence of crack propagation into the base metal. There was no visual oxide layer inside the crack. The roughened sample (Figure 53A,B) has a substantial amount of corrosion present on the surface. The oxide layer is ~600 µm thick (Figure 54) and the pit present is ~1 mm deep.

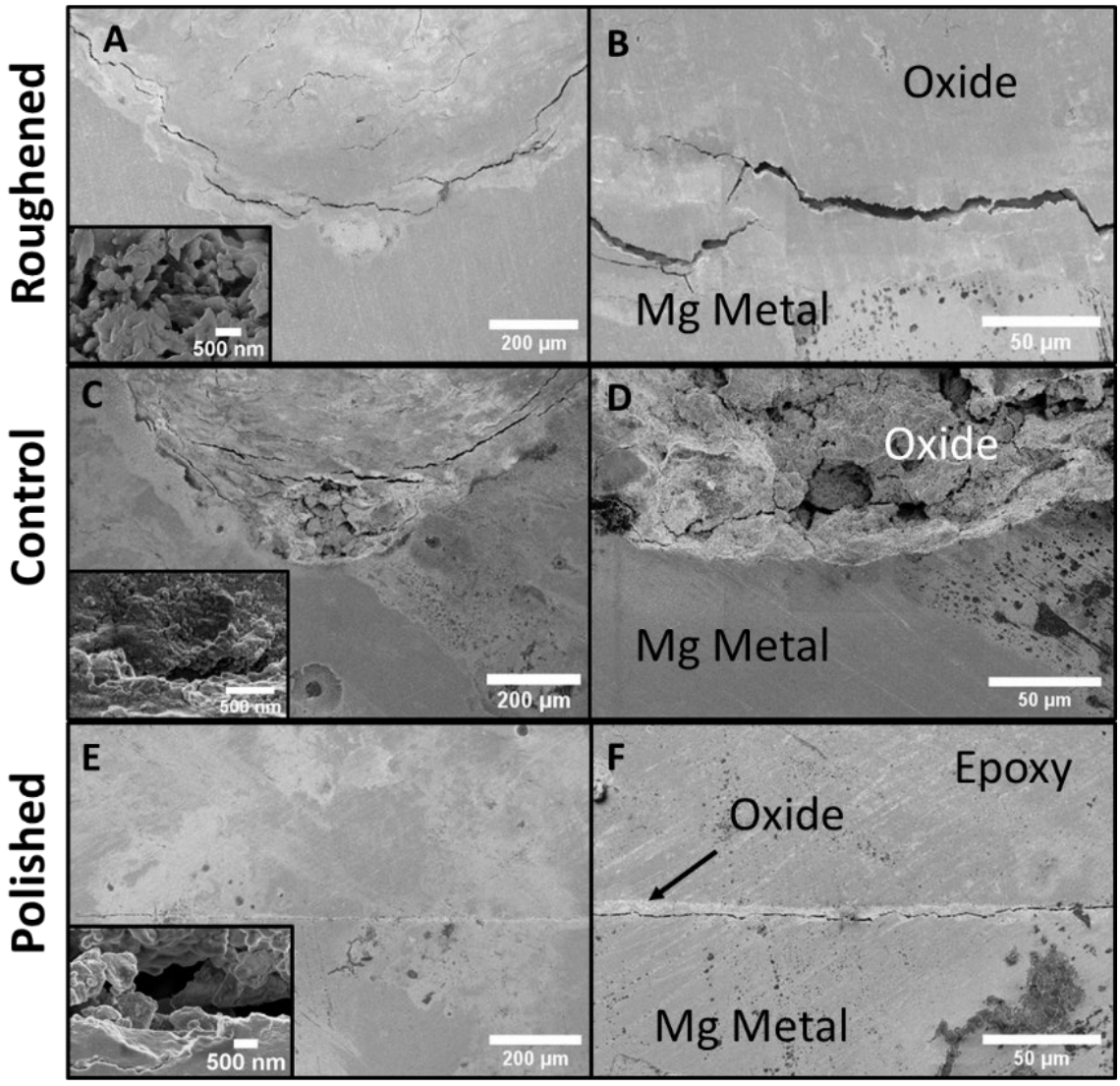

Figure 53. SEM images of the cross-sections for all three samples

The presence of two distinct oxide layers was expected but difficult to visually identify as a result of the sputtering. An EDS map of the area supports that there are indeed two distinct oxide layers. Figure 54 shows the map for oxygen. The oxygen map shows two different regions of oxygen near the surface of the sample. The difference in contrast between the two regions is due to a difference in counts received for oxygen within these regions. This indicates a change in oxidation concentration across the regions due to differences in the intrinsic chemistry, porosity, or both. The bright contrast regions are postulated to be MgO, which is expected to form a solid harder crust layer. The darker

contrast is believed to be the hydrated layer of brucite. Since brucite is hydrated, it will have a higher porosity as compared to a hard layer of MgO. Brucite would also be more likely to fill in a pit. Figure 54 shows that the dark contrast region appears to fill in a pore and the corresponding SEM micrograph shows the presence of microcracks and pores, indicating an overall higher porosity. Both oxides are depleted of Mg relative to the base metal according to the Mg map (not shown). The oxygen map also shows small pockets of oxygen within the base metal, indicating that oxygen ingress into the metal may occur prior to the evolution of a fully formed oxide.

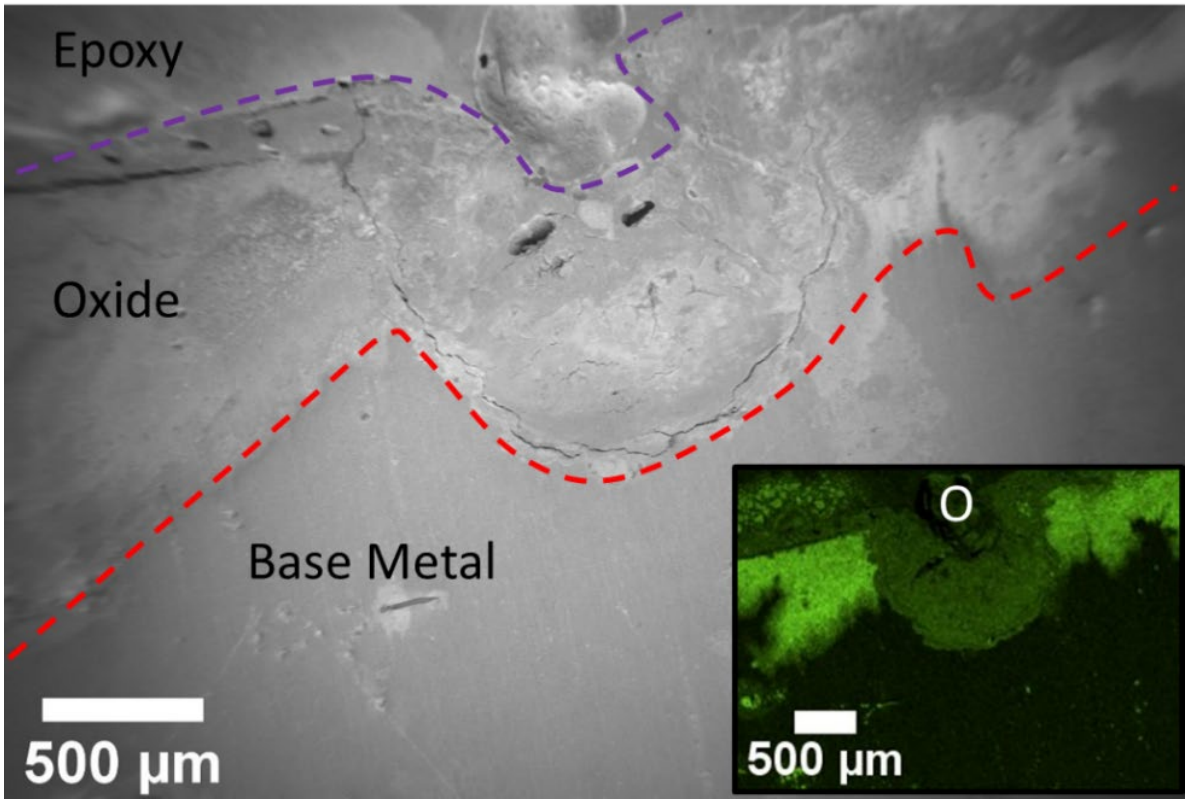

Figure 54. EDS map of a pit seen in the cross-section of the roughened sample

An EDS point analysis was performed on the cross-section of the roughened sample. Figure 55 shows the average of the analysis with all elements present. Five points were placed in a line in the base metal. Figure 55A shows the spectrum and averages for

each element for the first five points. The element is primarily magnesium with small amounts of oxygen, which was expected due to the native oxide layer formed on the cross-section and also from the diffusion of oxygen from the surface, as seen in Figure 54. The carbon present is a result of the mounting process for the samples and the platinum is from the platinum–palladium coating. Figure 55B shows the average of the other 10-point scans that were conducted within the oxide layer. The sodium and chlorine are most likely a result of the salt fog chamber solution. The oxygen being 31.03% by weight was consistent with that expected for brucite. Brucite has an extra oxygen in the molecule, which would result in higher oxygen values when compared with magnesium oxide. Brucite is the more dominant oxide present due to the surface condition of the roughened sample. The increase in surface roughness led to more numerous, deeper pits. The more severe corrosion leads to an increasing presence of brucite.

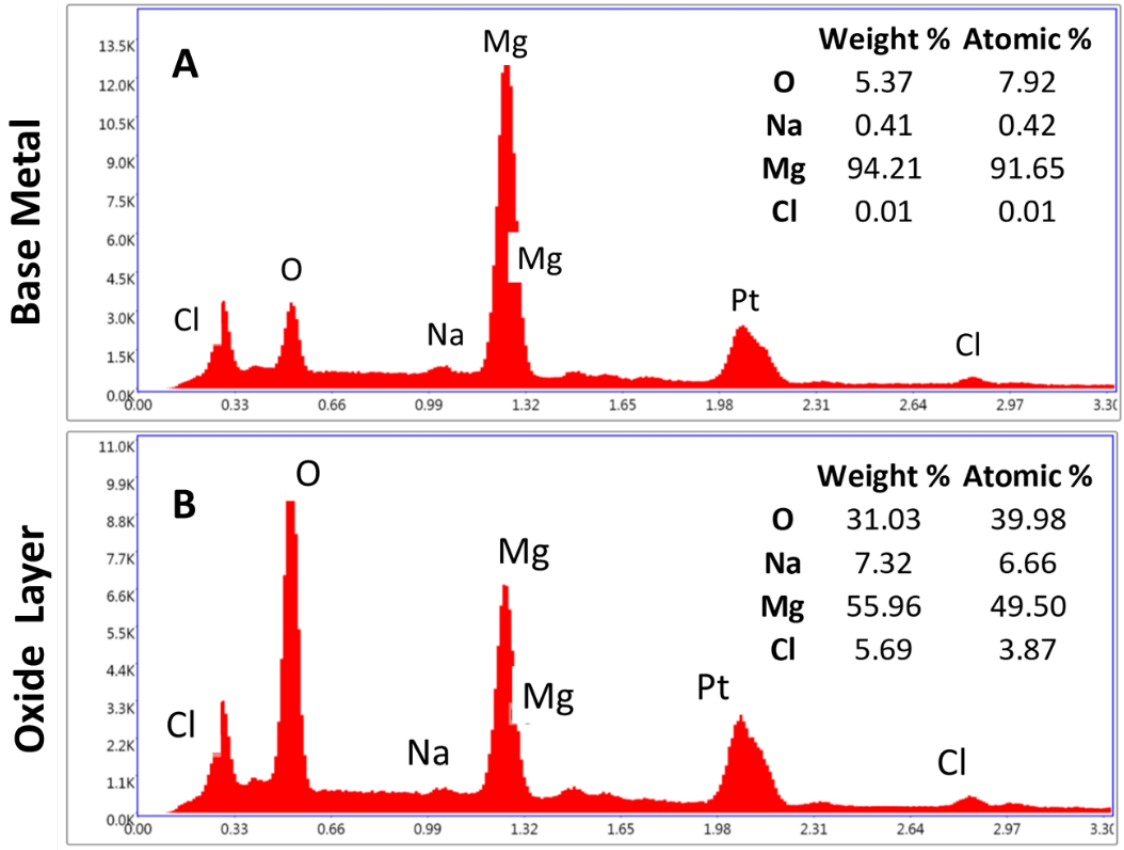

Figure 55. EDS analysis of roughened sample

VI. CONCLUSION

A. ADHESION STRENGTH

The primary focus of these experiments was to study how varying substrate and feedstock factors would affect the adhesion strength of a cold spray coating. Better adhesion strength is needed for cold spray to become a primary tool within the Navy and civilian industry. Without good adhesion, the coating will provide minimal protection against corrosion and could potentially make it worse. In order to determine how to increase cold spray adhesion, the feedstock powder and substrate were manipulated to analyze their effects on adhesion. The main areas of focus for this project will be the effects of the following characteristics on adhesion strength: i) the surface condition of the substrate, ii) the hardness of the substrate, and iii) the size of the cold spray particles. It was found that substrates that were roughened via grit blasting produced lower adhesion strengths when compared to the untouched samples. The largest trend from these experiments was the effect of substrate hardness on adhesion strength. Softer substrates produce higher adhesion strengths. It was also found that the softer substrates produce thinner coatings. These findings have a major impact on future cold spray applications and experiments. Further determining how substrate and feedstock factors can benefit cold spray coating adhesion strength is still required for this technology to become a primary method.

B. MAGNESIUM CORROSION

This section was previously published in the journal *Metals* [33]. This study investigated the effect of surface roughness modification treatments on an AZ31 Mg alloy on the corrosion rate in a simulated marine environment. Salt fog chamber experiments were conducted for 672 h on three samples with distinct surface states. One sample was roughened via grit blasting, another was mechanically polished to a near-mirror finish, and the last was left in its wrought form as a control sample. The roughened sample underwent severe uniform and pitting corrosion, characterized by a significant mass loss and the formation of a substantially greater amount of hydrated corrosion products. The SEM,

EDS, and XRD analyses showed the presence of deep pits (>1 mm) and indicated that corrosion products consisted of a relatively thin MgO layer formed, followed by a thicker layer of $Mg(OH)_2$. In contrast, the mechanically polished sample exhibited an insignificant mass change, and only sporadic discontinuous thin layers of oxide products were detected. This sharp contrast in the corrosion behavior of two AZ31 Mg alloy samples indicates that the surface roughness state has a profound impact on the subsequent corrosion behavior. These results have important implications for the fabrication and maintenance of Mg alloy parts and components exposed to marine environments. Further mechanistic studies using electrical impedance spectroscopy are planned to understand whether the surface roughness affects the intrinsic electrochemical characteristics at the Mg alloy subsurface.

VII. RECOMMENDATIONS

A. ADHESION EXPERIMENTS

Future experiments should be conducted using stainless steel powder in order to determine how particle hardness effects adhesion strength. It is also recommended to use helium gas with any hard materials such as stainless steel. There was a substantial difference in coating thickness and uniformity between the coatings sprayed with nitrogen vs. helium gas. It is recommended to use industrial strength adhesive that is designed to bond two different metals together. Some of the tests, namely the ones that utilized stainless steel as the coating, were potentially limited by the type of adhesive used. Using a stronger adhesive may produce results with a smaller standard deviation. It would be beneficial to have a cold spray machine with a large capacity heater and pressure regulator to support spraying harder materials.

B. MAGNESIUM CORROSION EXPERIMENTS

Future research is recommended in order to analyze the effects of a corrosion resistant coating, applied via cold spray, on the corrosion rate of the three different magnesium sample conditions. The samples should be prepared the same way and the experiment should follow the same procedures. It would be beneficial to see if the cold spray coating decreases the rate of corrosion and if it remains adhered to the surface for the duration of the experiment.

THIS PAGE INTENTIONALLY LEFT BLANK

LIST OF REFERENCES

[1] Singh, H., Sidhu, T. S., Kalsi, S. B. S., and Karthikeyan, J., 2012, "Development of Cold Spray from Innovation to Emerging Future Coating Technology," J. Braz. Soc. Mech. Sci. Eng., 35, pp. 231–245.

[2] Department of the Navy, 2019, Department of the Navy Fiscal Year (FY) 2019 Budget Estimates, Department of the Navy, Washington, D.C., USA.

[3] United States Government Accountability Office, 2018, DOD Should Take Additional Actions to Enhance Corrosion Prevention and Mitigation Efforts.

[4] Cavaliere, P., and Silvello, A., 2016, "Fatigue Behavior of Cold Sprayed Metals and Alloys: Critical Review," Surf. Eng., 32(9), pp. 631–640.

[5] Thurston, S., 1902, "Method of Impacting One Metal Upon Another."

[6] Grujicic, M., Zhao, C. L., DeRosset, W. S., and Helfritch, D., 2004, "Adiabatic Shear Instability Based Mechanism for Particles/Substrate Bonding in the Cold-Gas Dynamic-Spray Process," Mater. Des., 25(8), pp. 681–688.

[7] Raoelison, R. N., Xie, Y., Sapanathan, T., Planche, M. P., Kromer, R., and Costil, S., 2017, "Cold Gas Dynamic Spray Technology: A Comprehensive Review of Processing Conditions for Various Technological Developments till to Date," Addit. Manuf., 19, pp. 134–159.

[8] Allen, C. M., Marrocco, T., McNutt, P., Koivuluoto, H., Latokartano, J., Vuoristo, P., and Olsson, R., 2015, "A Novel Coaxially Laser-Assisted (COLA) Cold Spray System," TWI.

[9] Assadi, H., Gärtner, F., Stoltenhoff, T., and Kreye, H., 2003, "Bonding Mechanism in Cold Gas Spraying," Acta Mater., 51(15), pp. 4379–4394.

[10] Hassani-Gangaraj, M., Veysset, D., Champagne, V. K., Nelson, K. A., and Schuh, C. A., 2018, "Adiabatic Shear Instability Is Not Necessary for Adhesion in Cold Spray," Acta Mater., 158, pp. 430–439.

[11] Jodoin, B., Ajdelsztajn, L., Sansoucy, E., Zu'niga, A., Richer, P., and Lavernia, E. J., 2006, "Effect of Particle Size, Morphology, and Hardness on Cold Gas Dynamic Sprayed Aluminum Alloy Coatings," Surf. Coat. Technol., 201(6), pp. 3422–3429.

[12] Kainer, K. U., Kaiser, F., and Deutsche Gesellschaft für Materialkunde, 2003, Magnesium Alloys and Technology, Wiley-VCH, Weinheim, Germany.

[13] International Air Transport Association, 2004, Guidance Material and Best Practices for Fuel and Environmental Management, International Air Transport Association, Montreal, QC, Canada.

[14] Avedesian, M. M., and Baker, H., eds., 1999, ASM Specialty Handbook: Magnesium and Magnesium Alloys, ASM International, Materials Park, OH, USA.

[15] Mordike, B. L., and Ebert, T., 2001, "Magnesium: Properties — Applications — Potential," Mater. Sci. Eng. A, 302(1), pp. 37–45.

[16] Azzeddine, H., Hanna, A., Dakhouche, A., Rabahi, L., Scharnagl, N., Dopita, M., Brisset, F., Helbert, A.-L., and Baudin, T., 2020, "Impact of Rare-Earth Elements on the Corrosion Performance of Binary Magnesium Alloys," J. Alloys Compd., 829, pp. 1–14.

[17] Jönsson, M., Persson, D., and Thierry, D., 2007, "Corrosion Product Formation during NaCl Induced Atmospheric Corrosion of Magnesium Alloy AZ91D," Corros. Sci., 49(3), pp. 1540–1558.

[18] Kirkland, N. T., Lespagnol, J., Birbilis, N., and Staiger, M. P., 2010, "A Survey of Bio-Corrosion Rates of Magnesium Alloys," Corros. Sci., 52(2), pp. 287–291.

[19] Hasniyati, M. R., Zuhailawati, H., Sivakumar, R., and Dhindaw, B. K., 2015, "Optimization of Multiple Responses Using Overlaid Contour Plot and Steepest Methods Analysis on Hydroxyapatite Coated Magnesium via Cold Spray Deposition," Surf. Coat. Technol., 280, pp. 250–255.

[20] Zhang, L., Yang, S., Lv, X., and Jie, X., 2019, "Wear and Corrosion Resistance of Cold-Sprayed Cu-Based Composite Coatings on Magnesium Substrate," J. Therm. Spray Technol., 28(6), pp. 1212–1224.

[21] Wei, Y.-K., Luo, X.-T., Ge, Y., Chu, X., Huang, G.-S., and Li, C.-J., 2019, "Deposition of Fully Dense Al-Based Coatings via in-Situ Micro-Forging Assisted Cold Spray for Excellent Corrosion Protection of AZ31B Magnesium Alloy," J. Alloys Compd., 806, pp. 1116–1126.

[22] Siddique, S., Li, C.-X., Bernussi, A. A., Hussain, S. W., and Yasir, M., 2019, "Enhanced Electrochemical and Tribological Properties of AZ91D Magnesium Alloy via Cold Spraying of Aluminum Alloy," J. Therm. Spray Technol., 28(7), pp. 1739–1748.

[23] Xie, Y., Planche, M.-P., Raoelison, R., Hervé, P., Suo, X., He, P., and Liao, H., 2017, "Investigation on the Influence of Particle Preheating Temperature on Bonding of Cold-Sprayed Nickel Coatings," Surf. Coat. Technol., 318, pp. 99–105.

[24] Stoltenhoff, T., Kreye, H., and Richter, H. J., 2002, "An Analysis of the Cold Spray Process and Its Coatings," J. Therm. Spray Technol., 11(4), pp. 542–550.

[25] Assadi, H., Schmidt, T., Richter, H., Kliemann, J.-O., Binder, K., Gärtner, F., Klassen, T., and Kreye, H., 2011, "On Parameter Selection in Cold Spraying," J. Therm. Spray Technol., 20(6), pp. 1161–1176.

[26] Schmidt, T., Gärtner, F., Assadi, H., and Kreye, H., 2006, "Development of a Generalized Parameter Window for Cold Spray Deposition," Acta Mater., 54(3), pp. 729–742.

[27] Yin, S., Xie, Y., Suo, X., Liao, H., and Wang, X., 2015, "Interfacial Bonding Features of Ni Coating on Al Substrate with Different Surface Pretreatments in Cold Spray," Mater. Lett., 138, pp. 143–147.

[28] Raletz, F., Vardelle, M., and Ezo'o, G., 2006, "Critical Particle Velocity under Cold Spray Conditions," Surf. Coat. Technol., 201(5), pp. 1942–1947.

[29] Munson, B. R., Okiishi, T. H., Heubsch, W. W., and Rothmayer, A. P., 2013, Fundamentals of Fluid Mechanics, John Wiley & Sons, Inc., Hoboken, NJ.

[30] Urieli, Israel "Properties of Various Ideal Gases (at 300 K)" [Online]. Available: https://www.ohio.edu/mechanical/thermo/property_tables/gas/idealgas.html. [Accessed: 03-Nov-2020].

[31] Wong, W., Vo, P., Irissou, E., Ryabinin, A. N., Legoux, J.-G., and Yue, S., 2013, "Effect of Particle Morphology and Size Distribution on Cold-Sprayed Pure Titanium Coatings," J. Therm. Spray Technol., 22(7), pp. 1140–1153.

[32] Theimer, S., Graunitz, M., Schulze, M., Gaertner, F., and Klassen, T., 2019, "Optimization Adhesion in Cold Spraying onto Hard Substrates: A Case Study for Brass Coatings," J. Therm. Spray Technol., 28(1), pp. 124–134.

[33] Mitchell, J., Crow, N., and Nieto, A., 2020, "Effect of Surface Roughness on Pitting Corrosion of AZ31 Mg Alloy," Metals, 10(5), p. 651.

[34] ASTM International, 2011, ASTM B117-11, Standard Practice for Operating Salt Spray (Fog) Apparatus, ASTM International, West Conshohocken, PA.

[35] Esmaily, M., Ström, M., Svensson, J. e., Halvarsson, M., and Johansson, L. g., 2015, "Corrosion Behavior of Alloy AM50 in Semisolid Cast and High-Pressure Die Cast States in Cyclic Conditions," Corros. Journal Sci. Eng., 71(6), pp. 737–748.

[36] Cabrera, N., and Mott, N. F., 1949, "Theory of the Oxidation of Metals," Rep. Prog. Phys., 12(1), pp. 163–184.

[37] Agrawal, R., Baboukani, A. R., and Wang, C., 2019, “Expanding the Potential Window of Aqueous Electrochemical Capacitors with Binder-Free Electrostatically Sprayed Manganese Oxide Composite Cathode Films,” Mater. Res. Express, 6(8), p. 085012.

[38] Agrawal, R., Adelowo, E., Baboukani, A. R., Villegas, M. F., Henriques, A., and Wang, C., 2017, “Electrostatic Spray Deposition-Based Manganese Oxide Films-From Pseudocapacitive Charge Storage Materials to Three-Dimensional Microelectrode Integrands,” Nanomater. Basel Switz., 7(8), p. 198.

INITIAL DISTRIBUTION LIST

1. Defense Technical Information Center
   Ft. Belvoir, Virginia

2. Dudley Knox Library
   Naval Postgraduate School
   Monterey, California